FACULTY OF SCIENCE
UNIVERSITY OF COPENHAGEN

Study of forward elastic *pp* scattering at $\sqrt{s} = 8$ TeV with the ALFA detector

Simon Holm Stark

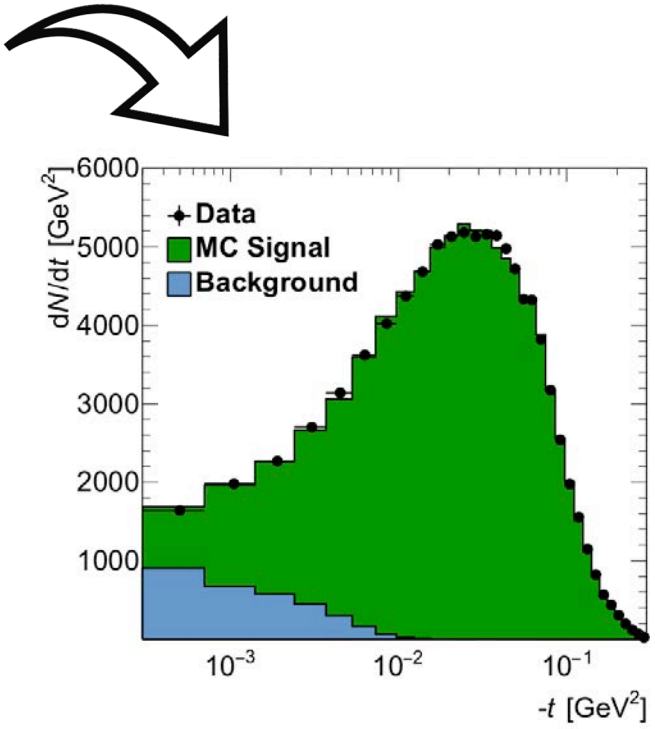

CERN-THESIS-2017-141
24/02/2017

Supervisors:
Peter Henrik Hansen
Jørgen Beck Hansen

January 2017

This thesis has been submitted to the PhD School of
The Faculty of Science, University of Copenhagen

A thank offering to the LORD God,
the Almighty.

Hver gang jeg havde til hensigt at forstå visdom, indså jeg om alt det, Gud gør, at mennesket ikke kan finde ud af det, der sker under solen. Hvor meget mennesket end slider og søger, finder det ikke ud af det. Og selv om den vise siger, at han forstår det, kan han ikke finde ud af det.

Prædikerens Bog kapitel 8 vers 16.

Abstract

The elastic pp scattering data analyzed in this thesis was taken at the LHC with the ALFA detector at $\sqrt{s} = 8$ TeV with a $\beta^* = 1$ km collision optics which gave access to the Coulomb-Nuclear-Interference region. An improved procedure was used to fit the observed number of elastic events as a function of the four-momentum transfer with a simulation based on theoretical expectations including experimental effects. The data can not exclude any of the investigated parametrizations for the modulus of the nuclear amplitude. The fit results for the total pp cross section, σ_{tot}, and the ratio of the real to imaginary forward elastic scattering amplitude, ρ, are:

$$\sigma_{\text{tot}} = 99.1 \pm 0.3 \text{ (stat.)} \pm 1.6 \text{ (syst.) mb} ,$$
$$\rho = 0.166 \pm 0.017 \text{ (stat.)} \pm 0.019 \text{ (syst.)} ,$$

which are in agreement with previous measurements. As part of the analysis, the detector distance to the beam was determined with an improved method. A new background estimation procedure was developed and also implemented in the determination of the elastic track reconstruction efficiency. The experience gained in this thesis was used to optimize the experimental settings for a new data taking at $\sqrt{s} = 13$ TeV with $\beta^* = 2.5$ km which will be used to determine the absolute luminosity for ATLAS.

Resumé på dansk

Denne afhandling analyserer elastiske proton-proton kollisioner med data fra ALFA detektoren ved LHC på CERN. Data er opsamlet ved en massemidtpunktsenergi på 8 TeV og en $\beta^* = 1$ km kollisionsoptik, hvilket muliggører en analyse i interferensområdet mellem Coulomb og nuklear spredning. En forbedret procedure er brugt til at fitte det observerede antal af elastiske begivenheder som funktion af den overførte fire-impuls med en simulering baseret på en teoretisk forventning, som inkluderer eksperimentielle effekter. Data kan ikke udelukke nogen af de undersøgte parameteriseringer brugt for beskrivelsen af den nukleare spredningsamplitude. Resultaterne af fittet for det totale proton-proton tværsnit, σ_{tot}, og forholdet mellem den reelle og den imaginære del af den forlæns elastiske spredningsamplitude, ρ, er:

$$\sigma_{\text{tot}} = 99.1 \pm 0.3 \text{ (stat.)} \pm 1.6 \text{ (syst.) mb} ,$$
$$\rho = 0.166 \pm 0.017 \text{ (stat.)} \pm 0.019 \text{ (syst.)} ,$$

hvilket er i overensstemmelse med tidligere målinger. Som en del af analysen er detektorernes afstand til LHC protonstrålen blevet bestemt med en forbedret metode i forhold til tidligere. Derudover er der udviklet en ny procedure til at estimere baggrundsprocesser, og denne er også implementeret i målingen af effektiviteten til at rekonstruere elastiske spor. Arbejdet i denne afhandling har resulteret i erfaringer, som blev brugt til at optimere forsøgsbetingelserne for opsamlingen af ny data ved en massemidtpunktsenergi på 13 TeV og en $\beta^* = 2.5$ km kollisionsoptik. Hensigten er at bruge denne data til at bestemme den absolutte luminositet for ATLAS.

Acknowledgment

Many people have contributed in one way or another to my thesis over the last three years, and I would like to express my gratitude.

The people in the HEP group at the Niels Bohr Institute deserves a thanks. You make the environment nice and cozy and everybody help each other.

Thanks to my supervisor Jørgen Beck Hansen for your most valuable ideas, your willingness to teach me programming, and for your hard critique of my work which pushed me to do better and learn more. Thanks to my other supervisor Peter Hansen. You have always been very kind to take your time to help me.

I want to thank all the people in the ALFA group for your help and support, especially Sune Jakobsen, Christian Heinz, and Hasko Stenzel. Sune introduced me to the exciting world of particle detectors, and I owe him big thanks for supervising me while I was at CERN and for spreading his knowledge about ALFA and LHC. Christian was my main collaborator in the data analysis, and our conversations about (potential) ROOT bugs and other people's stupidity (or our own) made the daily life at CERN much more fun. Hasko has the great overview of the previous ALFA analyses and could remind me how things "*were discussed at length in the past*". Thanks to Christian, Hasko, Rafal, and Jack who have collaborated with me on parts of the data analysis.

Jeg vil også gerne sige stor tak til min familie, som ikke har forstået meget af, hvad jeg har lavet, men alligevel har virket interesseret i mit arbejde. Specielt tak til min dejlige hustru, Anne. Det var ikke nemt, mens jeg opholdt mig på CERN, men vi kom igennem det ved Guds hjælp. Det er dejligt, hvordan du accepterer, at mit humør svinger i takt med mit arbejde.

The last and greatest thanks goes to God, my Heavenly Father and Creator of all things, who gives me every single breath, my scientific curiosity, my skills, and the opportunity to some extent say with Johann Kepler: "*O God, I am thinking Thy thoughts after Thee.*"

Contents

1 | Introduction

"*In the beginning, God created the heavens and the earth. God created man in his own image and said to them, »Be fruitful and multiply and fill the earth and subdue it«*" [1]. Mankind started with the mastering of stone, fire, water etc., and the continuing studies of the creation of God keep extending the subjugation to yet more areas. Sometimes knowledge is sought for pragmatic purposes, but often it is the curiosity of man which drives the work.

The last two hundred years have shown a tremendous expansion in the knowledge of sub-atomic processes. It started with electromagnetism and the discovery of the electron, continued with relativity and quantum mechanics, and by the end of the 20th century a total of 16 elementary particles and their antiparticles had been discovered and put into a theoretical framework called the Standard Model (SM). The most recent piece in the SM is the discovery of the Higgs Boson at the Large Hadron Collider (LHC) at CERN. Though the Higgs Boson was predicted already in the 1960s and its discovery in 2012 gave further evidence for our understanding of the elementary particles, the SM is not complete. There are still unanswered questions such as: What is the dark matter in the Universe which seems to be five times more abundant than ordinary matter? Can all fundamental forces be described in a Grand Unified Theory? What are the masses of the neutrinos and how can they be implemented in the SM? Given the overwhelming daily life improvements using electricity - which is possible due to the understanding of the electron - one can only imagine the consequences of a full understanding of the remaining elementary particles.

The LHC at CERN collides protons at the highest human made center-of-mass energy in the world. The hope is that the study of such processes eventually leads to answers of some of the big questions of particle physics. Searches for new heavy particles and precision measurements of the SM may show new physics which is not yet described by the SM. Other studies are the measurements of SM processes which cannot be calculated with current techniques. One such process is elastic proton-proton scattering which is the subject of this thesis.

The ALFA subdetector of ATLAS measures the positions of elastic scattered protons about 240 m down the LHC beam pipe from the interaction point, from which the kinematics can be deduced. Elastic scattering at small angles is related to the total proton-proton cross section, σ_{tot}, via the optical theorem, and σ_{tot} is used as an input parameter to simulations of other processes. Furthermore, the ratio of the real to imaginary forward elastic scattering amplitude, ρ, has predictive power for the energy evolution of σ_{tot}, which among other things is important for simulations of cosmic ray interactions

with the atmosphere.

This thesis presents the first ATLAS study of elastic scattering in the Coulomb-Nuclear-Interference region at $\sqrt{s} = 8$ TeV which allows a simultaneous measurement of σ_{tot} and ρ. These measurements are complementary to recently published results by the TOTEM Collaboration [2].

The first part of this thesis sets the theoretical framework. Chapter 2 gives a short introduction to the SM with a focus on Quantum Chromodynamics (QCD) which describes the strong interactions between quarks and gluons. It will be apparent that elastic proton-proton scattering can not be calculated in the framework of perturbative QCD. A study of elastic scattering therefore provides insight in the less understood non-perturbative regime. Here, one relies on phenomenological models which will be presented in Chapter 3.

The second part describes the experimental setup. The LHC provides the proton collisions and is described in Chapter 4. The transverse motion of the beam protons wrt. the center of the beam pipe is explained as it has a great influence on the elastic scattered proton trajectories. ATLAS is one of the four large experiments at CERN and is built to study many different processes. The parts of ATLAS relevant for elastic scattering is described in Chapter 5. The ALFA subdetector of ATLAS is designed to measure elastic proton scattering and a thorough description of ALFA is given in Chapter 6. Some of the ALFA calibration work carried out by the author is presented in Chapter 7.

The third part is devoted to the data analysis of elastic scattering in the very low momentum-transfer region where the Coulomb-Nuclear-Interference is visible. Chapter 8 describes the very special experimental settings used to collect the data. The event selection and background estimation is devoted to Chapter 9. The experimental effects on the data are determined in Chapter 10, and Chapter 11 describes how theoretical models are fitted to the data. The results are presented in Chapter 12, followed by a discussion in Chapter 13, and a conclusion in Chapter 14.

Part I

Theory

2 | The Standard Model

The aim of particle physics is to describe Nature by its smallest constituents, the elementary particles. The best available description is the Standard Model (SM), which uses Quantum Field Theory (QFT) to describe the interactions between the particles. Three out of the currently four known fundamental forces are included in the SM, namely the electromagnetic, the weak, and the strong force. Gravity is not yet included.

QFT combines quantum mechanics and special relativity and describes the elementary particles by different kinds of fields. In order for a field to interact via one of the forces, it must posses the corresponding *charge*. The charges are called electric, weak, and color for the electromagnetic force, the weak force, and the strong force, respectively. The theory describing electromagnetic interactions is known as Quantum Electrodynamics (QED), whereas the theory for strong interactions is Quantum Chromodynamics (QCD).

2.1 Running coupling constant

The strength of an interaction is given by the charges of the fields and by a coupling constant. One of the important consequences of QFT is that the coupling constants depend on the momentum transfer involved in the interaction between the particles. This behavior is known as the running coupling constants. Therefore, also the strengths of the interactions are momentum dependent. The electromagnetic coupling decreases with momentum, whereas the weak and strong couplings increase.

The running of the couplings restrict the possibility to do perturbative calculations to a certain range in the momentum transfer. The interaction is written as a Taylor expansion in the couplings, and only if the coupling strength is much less than 1, the expansion will converge, and a given precision can be reached within a finite order of perturbation theory. Figure 2.1 shows measured values of the strong coupling constant, α_s, as a function of the transferred momentum, Q. At large Q, it is in many cases sufficient to do perturbative calculations keeping only up to the next-to-leading order terms in the expansion. However, it is clear that perturbative QCD is only safe at $Q \gtrsim 1$ GeV. In strong processes with low momentum transfer, one must rely on phenomenological models instead. The situation is completely different in QED where the precision of perturbative calculations increases with decreasing momentum transfer. In practice, the coupling constant of QED is below 0.01 even at $Q \sim 10^6$ GeV, hence the perturbative calculations of QED are well behaved and precise.

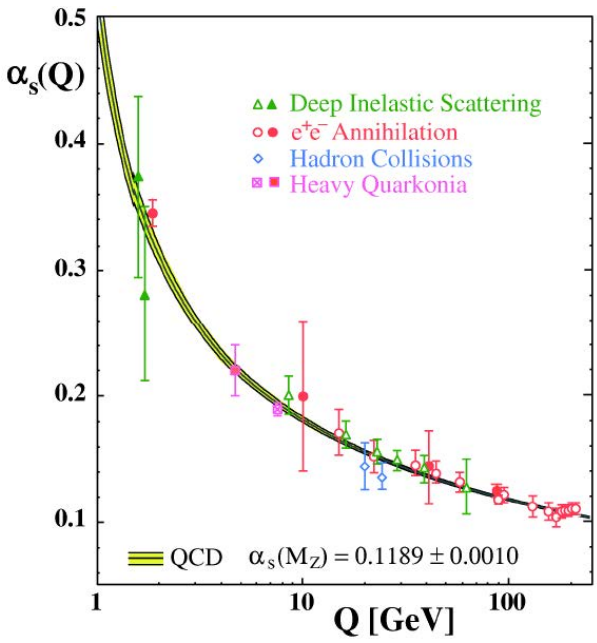

Figure 2.1: Measurements of the strong coupling constant, α_s, as a function of the momentum transfer, Q. From Ref. [3].

2.2 Particles

The particles of the SM is shown in Figure 2.2. The leptons and quarks (and their anti-particles) make up the matter around us. The quarks interact via all three forces, whereas the leptons have no color charge and hence do not interact strongly. The photon is the mediator of the electromagnetic force. It has no mass which gives an infinite range for the force. The strong force is mediated by the gluons. The gluon itself possess color charge and hence couple strongly to other gluons. In contrast, the photon does not carry electric charge and does not couple to other photons. This difference explains the completely different behavior of the running coupling constants in QED and QCD. The $W^{\pm}$ and Z bosons have masses around 100 GeV and they mediate the weak force. Due to their large masses, the weak interactions can be neglected in processes with small momentum transfer. QFT is built upon the principle of local gauge invariance which precludes an explicit assignment of masses to the $W^{\pm}, Z$ bosons. The Higgs boson is a manifestation of a mechanism that breaks the gauge symmetry and thereby provides masses to the particles.

2.3 The proton

No isolated quark has ever been observed, which is a consequence of the running α_s. The strong force increases when the distance between two quarks increases, since the distance probed by the force is inversely proportional to the momentum transfer of the force. At some point is becomes energetically more favorable to break the gluon field between the

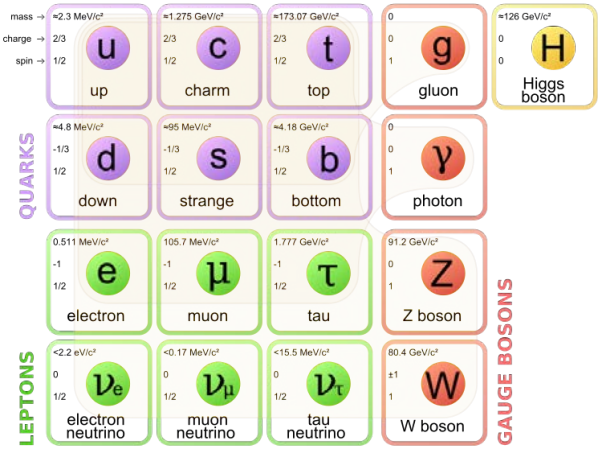

Figure 2.2: The particles in the Standard Model. Corresponding anti-particles with opposite charges exist for the leptons and quarks but are not shown here. From Ref. [4].

two quarks whereby a quark-antiquark pair is produced, and there will now be two sets of quark pairs instead of the original one. Instead, one can study bound states of quarks to better understand QCD.

The proton can be used to study the strong force. At low energies, the proton can be described as a bound state of two up-quarks and a down-quark in a color combination which leaves the proton colorless (otherwise an isolated proton could also not be observed). Probing the proton at higher energies - which by Heisenbergs uncertainty principle corresponds to smaller distances - reveals that the proton is better described by a collection of many quarks and gluons. The interpretation is that the three valence quarks, up-up-down, continuously emit gluons. These are then either reabsorbed or they split into gluons or quark-antiquark pairs.

The proton has electric charge +1 which means that it will interact via QED. This is an important feature exploited in particle accelerators where the proton is guided and brought to collision using electric and magnetic fields. The proton has no color charge, but its constituents of quarks and gluons do. This allows one quark/gluon in a proton to interact strongly with a quark/gluon in another proton. When two protons collide at high energy, the interacting quarks/gluons can have high momentum. In such cases, the perturbative calculations can be used. However, it is not possible to calculate the momentum probability distribution of a quark/gluon inside the proton, hence this has to be measured in other kinds of experiments.

The interactions between two protons can be classified as follows:

Hard interactions where a high momentum quark/gluon from each of the protons interact and produces for instance a Higgs boson. Such processes are calculable with perturbative QCD.

Soft interactions where the momentum transfer between the interacting quarks/gluons is low and hence perturbative QCD is not applicable.

Elastic proton scattering where the interaction only leads to a change of momentum

of the two protons. Such processes involve low momentum transfer and are also not calculable with perturbative QCD. Furthermore, an elastic process is an interplay between QCD and QED since both the exchange of a photon and a system of gluons can cause the change in momentum.

All of these processes are important for a more complete understanding of QCD and the SM. This thesis focuses on elastic scattering. The theory behind elastic scattering is described in the next chapter.

3 | Forward elastic scattering

Forward elastic proton-proton (pp) scattering is not calculable with perturbative QCD as it involves low momentum transfer, and phenomenological models are used to provide a description. A measurement of forward elastic scattering therefore probes the strong force in a phase-space region where the understanding is inadequate. This chapter describes the basics of forward elastic scattering and some of the specific models. In addition, it will be shown how the total pp cross section can be inferred from elastic scattering using the optical theorem. All factors of c and $\hbar$ are omitted in the following.

3.1 Kinematics

Elastic pp scattering is characterized by two initial state protons with four-momentum p_1 and p_2 and two final state protons with four-momentum p_3 and p_4. The center-of-mass energy squared is given by the Mandelstam s variable:

$$\begin{aligned} s &= (p_1 + p_2)^2 \\ &= 4\left(p^2 + m^2\right) \ , \end{aligned} \tag{3.1}$$

where $p = |\mathbf{p}|$ is the magnitude of the three-momentum of the protons and m is the proton mass. The four-momentum transfer in an elastic collision is given by the Mandelstam t variable:

$$\begin{aligned} t &= (p_1 - p_3)^2 \\ &= (E_1 - E_3)^2 - (\mathbf{p_1} - \mathbf{p_3})^2 \\ &= -2p^2 + 2p^2\cos(\theta) \ , \end{aligned} \tag{3.2}$$

where θ is the scattering angle. In forward scattering the angle is very small, hence

$$\begin{aligned} t &\simeq -2p^2 + 2p^2(1 - \theta^2/2) \\ &= -(p\theta)^2 \ . \end{aligned} \tag{3.3}$$

3.2 Elastic cross section

The cross section of a given process is a measure of the probability for that specific interaction. The scattering amplitude F is defined in terms of the differential elastic

cross section:

$$\frac{\mathrm{d}\sigma_{\mathrm{el}}}{\mathrm{d}t} = |F|^2 \,, \tag{3.4}$$

where a kinematical factor $\frac{1}{16\pi s(s-m^2)}$ is absorbed into this definition of the Lorentz invariant amplitude. The protons have electric charge and will therefore have electromagnetic interactions described by the Coulomb force. However, the protons also interact via the strong force due to their internal nuclear quark/gluon structure. Therefore, the differential elastic cross section can be written as

$$\frac{\mathrm{d}\sigma_{\mathrm{el}}}{\mathrm{d}t} = \left|F_C(t)e^{i\alpha\phi(t)} + F_N(t)\right|^2 \,, \tag{3.5}$$

where F_C is the Coulomb amplitude, F_N is the nuclear amplitude, α is the fine structure constant, and $\phi(t)$ is a phase describing the interference between the Coulomb and the nuclear amplitudes. Each of the contributions are described in the following.

3.2.1 Coulomb scattering amplitude

The Coulomb scattering amplitude accounts for the electromagnetic interaction between the two protons. Unlike QCD, QED can be described using perturbation theory even at very small momentum transfer, hence the Coulomb part of elastic scattering is 'well-known'.

One caveat is the size of the proton. For small momentum transfer, the virtual photon exchanged between the two protons has a long wavelength compared to the size of the proton which means that it will 'see' the entire proton charge. As the momentum transfer increases, the wavelength decreases and the photon will only see a part of the proton charge, hence the scattering amplitude will decrease.

The decrease of the scattering amplitude is described with the electric form factor, which is defined as the Fourier transform of the charge density. For many years, the dipole approximation was used for the form factor where the charge distribution of the proton is described by a spherically symmetric exponential decrease which gives the form factor:

$$G(t) = \left(\frac{\Lambda}{|t| + \Lambda}\right)^2 \,, \quad \Lambda = 0.71 \text{ GeV}^2 \,. \tag{3.6}$$

Alternative models are fit to data in Ref. [5] where also the magnetic form factor is discussed. The dipole model is ruled out by the data, however many of the alternative models have no physical interpretation and are simply constructed to be as flexible as possible. The resulting form factors for some of the models can be seen in Figure 3.1. The largest difference to the dipole approximation is the double dipole parametrization which is simply the sum of two dipoles.

With a given parametrization of the form factor, the Coulomb amplitude can be written as

$$F_C(t) = -\frac{2\sqrt{\pi}\alpha G^2(t)}{|t|} \,. \tag{3.7}$$

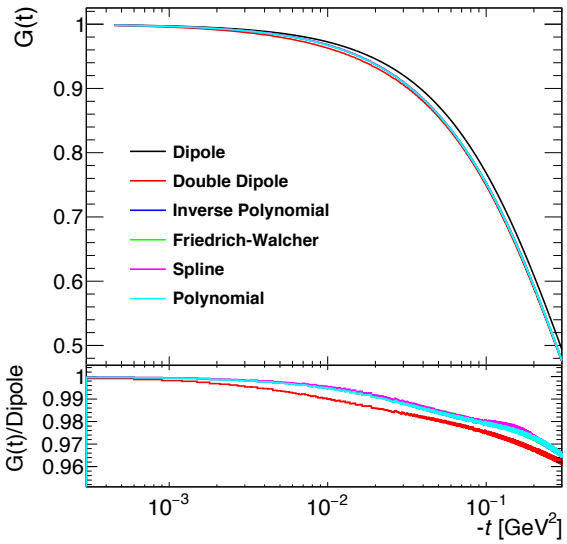

Figure 3.1: The electric form factor of the proton. The different parametrizations were obtained by the A1 Collaboration [5].

3.2.2 Nuclear scattering amplitude

The nuclear amplitude cannot be calculated with perturbative QCD. Traditionally, the modulus of the nuclear scattering amplitude has been parametrized with an exponential function such that

$$\frac{\mathrm{d}\sigma_N}{\mathrm{d}t} = \frac{\mathrm{d}\sigma_N}{\mathrm{d}t}\Big|_{t=0} \cdot e^{-B|t|} \,, \tag{3.8}$$

where B is a center-of-mass dependent parameter which must be determined from the data. However, it is an experimental fact that it can only be an approximation at small t, see Figure 3.2. A 'dip' in the differential elastic cross section occurs at $|t| \sim 0.5$ GeV^2, and at even higher $|t|$ the slope is better described with a power law[1].

Many different phenomenological approaches have been used to model the nuclear amplitude. These models use different parametrizations in the exponent with more free parameters, and some models allow a different amplitude for the real and imaginary part, i.e. a t-dependent phase of the scattering amplitude. Recently, the TOTEM Collaboration has obtained a good description of elastic data at $\sqrt{s} = 8$ TeV using a second order polynomial in the exponent for the modulus [7].

3.2.3 Coulomb phase

The Coulomb phase describes the interference between the electromagnetic and the nuclear scattering amplitudes. Based on lowest-order Feynman diagrams where both nuclear and Coulomb interactions are present, West and Yennie have derived the following

[1]The dip and following peak resembles what in classical optics is called *diffraction* of light hitting a totally absorbing 'black disc' which is explained by the Huygens-Fresnel principle.

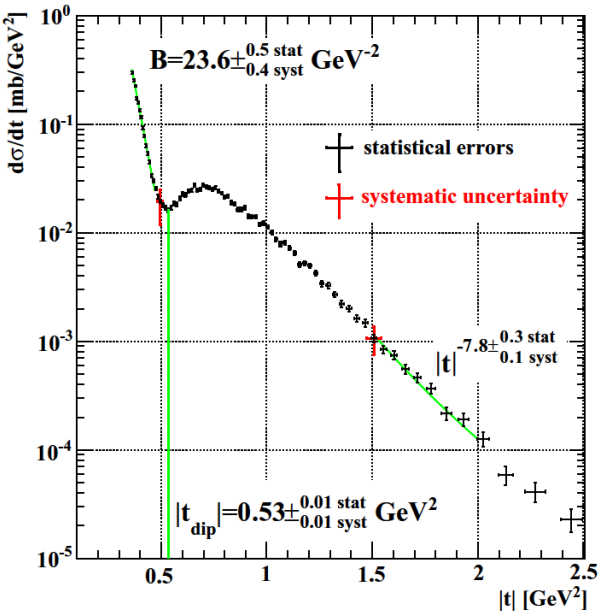

Figure 3.2: The differential elastic cross section at $\sqrt{s} = 7$ TeV measured by TOTEM [6].

expression for the phase [8]:

$$\phi(t) = -\gamma_E - \ln\left(\frac{B|t|}{2}\right) , \qquad \gamma_E = 0.5777\ldots \tag{3.9}$$

where the assumption of a pure exponential nuclear amplitude is used. Cahn has used an eikonal approach where also the effect of the electric form factor is included and found [9]:

$$\phi(t) = -\left[\gamma_E + \ln\left(\frac{B|t|}{2}\right) + \ln\left(1 + \frac{8}{B\Lambda}\right)\right] + \frac{4|t|}{\Lambda}\ln\left(\frac{\Lambda}{4|t|}\right) - \frac{2|t|}{\Lambda} \tag{3.10}$$

More general models for the phase without the assumption of a pure exponential nuclear amplitude are discussed in Ref. [2].

3.3 The total cross section

The optical theorem follows from conservation of probability. It can be derived using the S-matrix formalism where the S-matrix transforms the initial state $|i\rangle$ to the final state $|f\rangle$ by

$$S|i\rangle = |f\rangle \, . \tag{3.11}$$

Using the fact that

$$\langle i|S^\dagger S|i\rangle = 1 \tag{3.12}$$

and writing

$$S = \mathbb{1} + iT \tag{3.13}$$

one ends up with the relation

$$2 \text{ Im } T_{if} = \sum_n T^*_{fn} T_{in} \ . \tag{3.14}$$

For forward elastic scattering with $t = 0$, the final state equals the initial state and one ends up with a relation between the total pp cross section, σ_{tot}, and the imaginary part of the forward elastic nuclear scattering amplitude:

$$\sigma_{\text{tot}} = 4\sqrt{\pi} \text{Im} F_N(t \to 0) \ . \tag{3.15}$$

See for instance Ref. [10] for a full derivation of the theorem.

The optical theorem can be used to rewrite Equation (3.8):

$$\begin{aligned}
\frac{\mathrm{d}\sigma_N}{\mathrm{d}t} &= \frac{\mathrm{d}\sigma_N}{\mathrm{d}t}\Big|_{t=0} \cdot e^{-\Omega(t)} \\
&= |F_N(t=0)|^2 \, e^{-\Omega(t)} \\
&= \left| \left(\frac{\text{Re}F_N(t=0)}{\text{Im}F_N(t=0)} + i \right) \text{Im}F_N(t=0) \right|^2 e^{-\Omega(t)} \\
&= \left| (\rho + i) \, \frac{\sigma_{\text{tot}}}{4\sqrt{\pi}} e^{-\Omega(t)/2} \right|^2
\end{aligned} \tag{3.16}$$

where

$$\rho \equiv \frac{\text{Re}F_N(t=0)}{\text{Im}F_N(t=0)} \ , \tag{3.17}$$

and where $\Omega(t)$ is any parametrization of the exponent. Equation (3.5) can now be written as

$$\begin{aligned}
\frac{\mathrm{d}\sigma_{\text{el}}}{\mathrm{d}t} =& \left| F_C(t) e^{i\alpha\phi(t)} + F_N(t) \right|^2 \\
=& \left| -\frac{2\sqrt{\pi}\alpha G^2(t)}{|t|} e^{i\alpha\phi(t)} + (\rho + i) \, \frac{\sigma_{\text{tot}}}{4\sqrt{\pi}} e^{-\Omega(t)/2} \right|^2 \\
=& \frac{4\pi\alpha^2 G^4(t)}{|t|^2} \\
& - \sigma_{\text{tot}} \frac{\alpha G^2(t)}{|t|} \left[\rho \cos(\alpha\phi(t)) + \sin(\alpha\phi(t)) \right] e^{-\Omega(t)/2} \\
& + \sigma^2_{\text{tot}} \frac{(\rho^2 + 1)}{16\pi} e^{-\Omega(t)} \ ,
\end{aligned} \tag{3.18}$$

where the first term is the pure Coulomb interaction, the second is the Coulomb-Nuclear-Interference (CNI) term, and the last term is the pure Nuclear interaction.

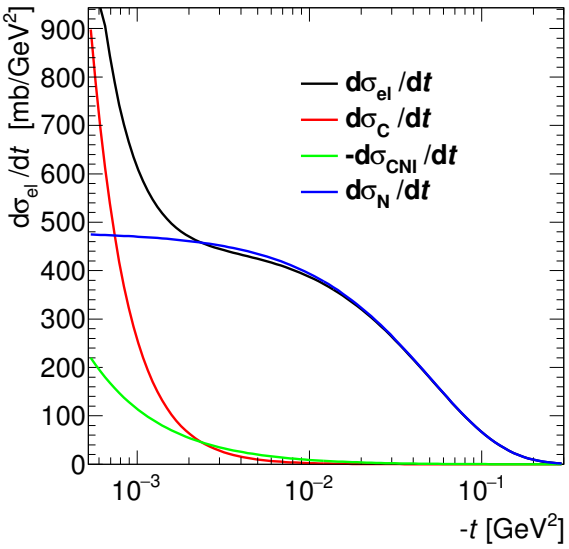

Figure 3.3: Theoretical prediction of the differential elastic cross section at $\sqrt{s} = 8$ TeV with $\sigma_{\text{tot}} = 96$ mb, $B = 19.7$ GeV^{-2} and $\rho = 0.136$. The CNI term is negative and have been mirrored on the x-axis for illustration purpose.

Figure 3.3 shows the three contributions to the differential elastic cross section, $\mathrm{d}\sigma_{\text{el}}/\mathrm{d}t$, where the dipole approximation is used for the form factor, the West-Yennie formula for the interference phase, and the pure exponential decay is used for the nuclear modulus. The difference in $\mathrm{d}\sigma_{\text{el}}/\mathrm{d}t$ to the double dipole and the phase by Cahn is below 0.5 % in $10^{-4} \leq -t \leq 0.3$ GeV^2. The large $|t|$ region is dominated by the nuclear part and is useful to measure the t-dependence of the nuclear amplitude. The CNI and Coulomb interactions start to contribute at $-t \sim 10^{-3}$ GeV^2, and this region has the best sensitivity to the ρ parameter, the interference phase, and the phase of the nuclear amplitude. At $-t \lesssim 2 \cdot 10^{-4}$ GeV^2 the Coulomb part constitutes more than 90 % of the cross section, and since the Coulomb term is well known from QED, the luminosity, L, can be inferred from

$$\frac{\mathrm{d}\sigma_{\text{el}}}{\mathrm{d}t} = \frac{1}{L} \cdot \frac{\mathrm{d}N_{\text{el}}}{\mathrm{d}t} \approx \frac{4\pi\alpha^2 G^4(t)}{|t|^2} \,. \tag{3.19}$$

The luminosity is an experimental quantity which relates the number of observed events for a given process, N, to the cross section of that process. Therefore, the precision on L is important for all measurements.

The total cross section is an important quantity to measure at new center-of-mass energies, since it is impossible to calculate with perturbative QCD, like for the elastic cross section. It is the sum of all proton-proton interactions and is used to set the scale for other processes, in particular for diffractive processes defined as inelastic processes where no quantum numbers are exchanged between the particles. The diffractive cross sections are large but poorly known since they involve low momentum transfer. The scaling of cross sections plays a role also for measurements of rare processes where σ_{tot} is

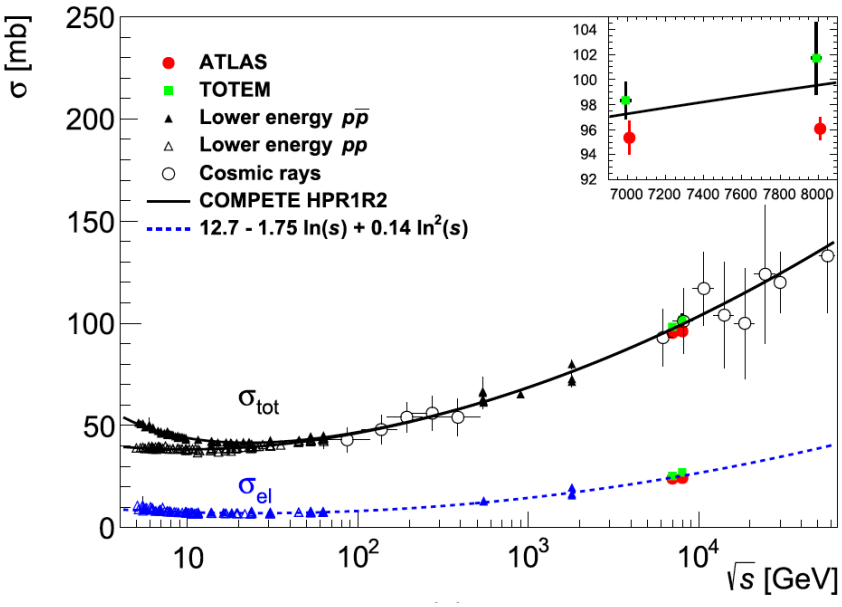

Figure 3.4: The total and elastic cross sections as a function of the center-of-mass energy [11]. The fit is not updated with the ATLAS $\sqrt{s} = 8$ TeV measurement.

used to understand the abundant so-called 'pile-up' events which are additional collisions happening in the same bunch crossing.

Figure 3.4 shows the observed increase of the total cross section with center-of-mass energy. Apart from the Froissart-Martin bound [12, 13] which states that it can not increase faster than $\ln^2(s)$ at asymptotic energies, the predictions at new energies are uncertain. The ρ parameter is related to the energy evolution of σ_{tot} through dispersion relations [14], and a measurement of ρ will give insight in the asymptotic behavior of σ_{tot}. Therefore, a measurement of ρ is particularly useful for models of astroparticle physics where the energy is high and the cross sections correspondingly uncertain.

The expression (3.18) will be used later to extract σ_{tot} and ρ from a measurement of the differential elastic cross section.

Part II

Experimental setup

4 | The LHC

The Large Hadron Collider (LHC) is the most powerful particle accelerator in the world. It is built to test the predictions of the SM and search for new physics. LHC is a part of the CERN accelerator complex which is located at the border between France and Switzerland.

This chapter gives an introduction to the LHC as it was in 2012 where the data for this thesis was taken. An overview of the CERN accelerator complex is given. The LHC aperture relevant for the elastic analysis is described. The transverse motion of protons and the beam properties are discussed in some detail as it has importance for the reconstruction of the four-momentum tranfer for elastic scattered protons. Unless otherwise stated, the information in this chapter is from Ref. [15].

4.1 The CERN accelerator complex

The LHC is the last part of the CERN accelerator chain shown in Figure 4.1. Several steps are needed before the protons can be collided: A strong electric field is used to strip off the electrons in hydrogen molecules, leaving only the protons. The bunch of protons is injected to the LINAC 2 which accelerates the protons to an energy of 50 MeV. Afterwards, the proton bunch is injected to the BOOSTER, the PS and the SPS reaching an energy of 450 GeV before the final injection to the LHC. When the LHC has been filled with the required number of bunches, the final acceleration from 450 GeV to 4 TeV is performed.

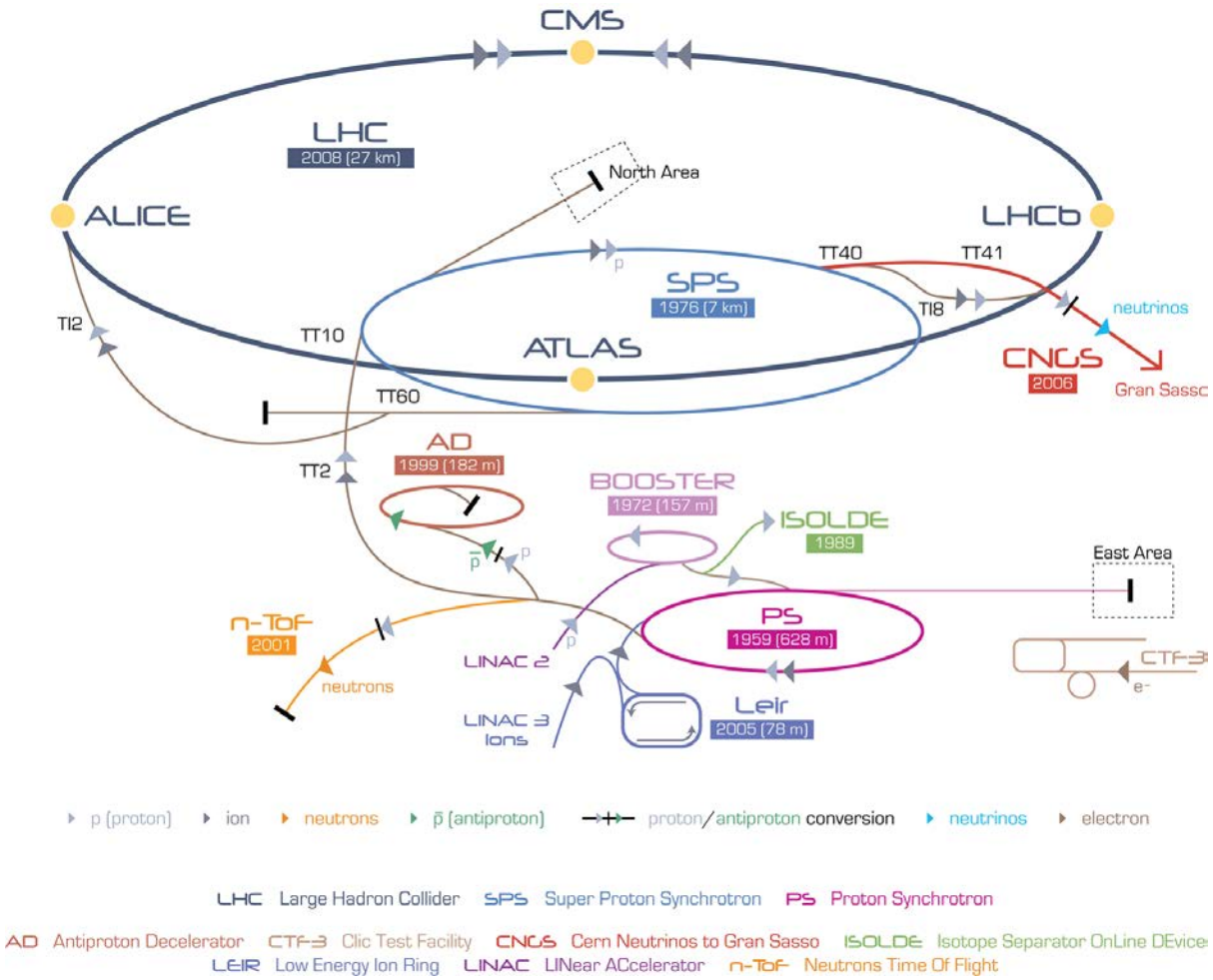

Figure 4.1: The CERN accelerator complex [16].

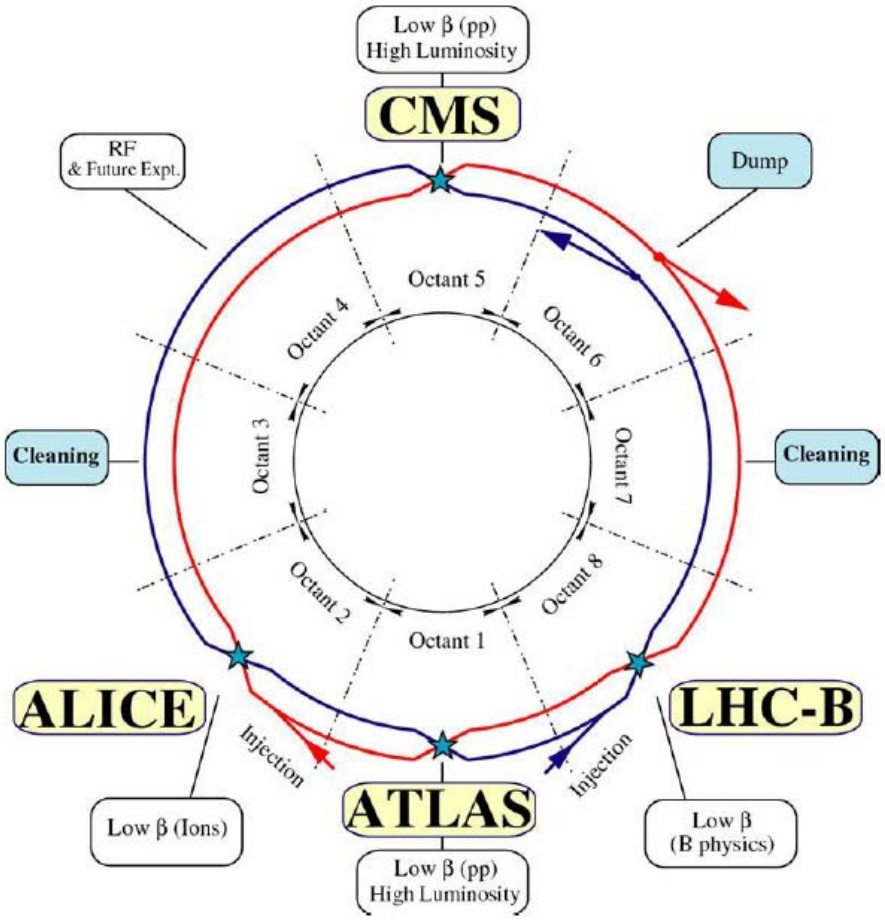

Figure 4.2: Schematic layout of the LHC. The original figure is from Ref. [17].

4.2 LHC aperture

LHC is built in a 27 km long circular tunnel about 50-175 m underground. It accelerates and collides two circulating beams of protons - one in the clockwise direction and one in the counterclockwise. LHC consists of eight bent sections where the proton trajectories are circular, and eight straight sections where the protons can collide. This is where the four main LHC experiments are located: ATLAS, CMS, LHCb, and ALICE, see Figure 4.2.

In the bent sections, the two beams are separated into two beam pipes, but the beams share the same beam pipe about 100 meters before and after the Interaction Points (IPs) in the straight sections. The beam pipes have an ultra high vacuum of about $10^{-10} - 10^{-11}$ mbar, which is important in order to reduce the interaction probability with air molecules. Such interactions would reduce the beam intensity, create heat, and be a background source for the experiments.

Protons are charged particles and are hence affected by electric, $\mathbf{E}$, and magnetic, $\mathbf{B}$, fields according to the Lorentz force:

$$\mathbf{F} = q\left(\mathbf{E} + \mathbf{v} \times \mathbf{B}\right) \ , \tag{4.1}$$

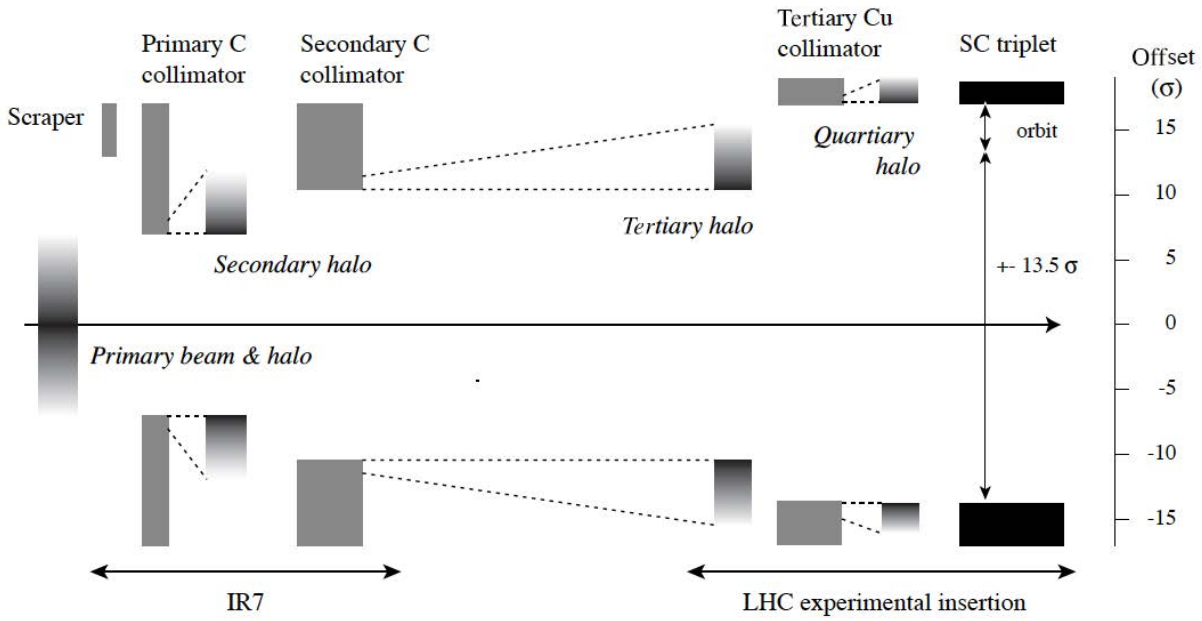

Figure 4.3: Principle behind the LHC collimation setup.

where q is the proton charge and $\mathbf{v}$ is the velocity which is almost the speed of light already at the injection. In the LHC, an electric field is used to accelerate the protons, whereas a magnetic field is used to bent and focus the protons inside the beam pipes.

The acceleration from 450 GeV to 4 TeV is done with a longitudinal electric field provided by radio frequency cavities at a single location in the LHC. The phase of the longitudinal field is adjusted during the acceleration in order to take into account the increasing momentum of the protons and thereby later arrival time due to a larger orbit. The protons in a bunch do not have the exact same energy, but the phase is adjusted such that low (high) energy protons get a larger (smaller) kick. In this way, the electric field preserves the injected bunch structure.

The protons are bent by a total of 1232 superconducting dipole magnets in order to obtain a circular trajectory. The magnets are cooled to 1.9 K using liquid helium and are operated at up to 11850 A yielding a magnetic field of up to 8.33 T. More than 8000 additional quadrupoles and higher order magnets are used to focus the protons and keep them inside the beam pipes which are only about 4 cm in diameter.

The LHC magnets must be protected against accidental hits from the highly energetic beam protons, since this will otherwise quench the magnets. Due to different beam dynamics processes, protons from the beam will continuously be lost to the *beam halo*, i.e. a collection of particles not moving on the designed trajectory. The beam halo must be continuously removed to protect the magnets and also to reduce halo-induced background in the experiments. Furthermore, accidental fluctuations of the beam could hit the magnets and/or experiments. Therefore, a series of collimators are installed in the LHC. The principle behind the collimators is shown in Figure 4.3. The primary collimators scrape away the outermost part of the beam halo. The interactions between the collimator and the halo particles create a shower called the secondary halo. This secondary halo is then

removed by the tertiary collimators. The collimators are moveable and can be adjusted to a given distance to the beam. No apparatus is allowed to be moved closer to the beam than the collimators. The collimator settings play a crucial role in the elastic data taking in Chapter 8.

4.3 Luminosity definition

The luminosity, L, is an experimental quantity which relates the observed number of events for a given process, N, to the corresponding cross section, σ, by:

$$N = L \cdot \sigma \ . \tag{4.2}$$

The luminosity is therefore of greatest importance in the translation from experimental observations to the underlying physics. For a storage ring like the LHC where two bunched beams rotate and collide with a revolution frequency, f, the instantaneous luminosity, $\mathscr{L}$, is given by [18]:

$$\mathscr{L} = f n_B \frac{n_1 n_2}{4\pi\sigma_x\sigma_y} \ , \tag{4.3}$$

and the luminosity is found by integrating over time. Here, n_B is the number of colliding bunches in the beams, n_1 and n_2 are the number of particles in the bunches, and σ_x, σ_y characterize the profiles of the beams in the transverse plane to the beam direction.

The revolution frequency is given by the speed of the particles and the circumference of the LHC and has a value of 11245 Hz. The number of particles in the beams are measured by Bunch Current Transformers with a precision around 0.5 % [19]. The convoluted transverse shape of the beams is determined by Van der Meer scans [20], where the beams are displaced in the horizontal and vertical directions: The counting rate in a monitor is observed as a function of the displacement from which σ_x, σ_y can be deduced.

4.4 Beam dynamics

The coordinate system of the LHC is chosen such that protons on the designed trajectory, the design orbit, have the coordinates $(x, y, z) = (0, 0, s)$. The x-axis is pointing towards the center of the LHC, the y-axis points upwards in vertical direction, and the z-axis goes in the counterclockwise direction as seen from above. In the following, the transverse motion of the protons wrt. the design orbit is described. The properties of the transverse motion need to be adjusted depending on the intended type of physics measurement.

4.4.1 Transverse motion

The transverse motion of the protons in the LHC, $u(s)$, satisfies Hill's equation:

$$\frac{\mathrm{d}^2}{\mathrm{d}s^2}u(s) + K(s)u(s) = 0 \ , \quad K(s+L) = K(s) \ , \tag{4.4}$$

where K is given by the LHC magnet settings and L is the circumference of the LHC. To first order, the horizontal and vertical motions are decoupled, hence the equation holds for both separately: $u = x, y$. The real part of the solution can be written as a quasi-harmonic oscillator:

$$u(s) = \sqrt{\epsilon\beta(s)}\cos(\Psi(s) - \Psi(0)) \ , \quad \Psi(s) \equiv \int_0^s \frac{\mathrm{d}z}{\beta(z)} \ . \tag{4.5}$$

Here, Ψ is the phase advance from the starting point at $s = 0$. It is important that $\Psi(L)$ is not a rational number since otherwise there can be constructive interference from magnet imperfections over many cycles in the LHC. The amplitude is determined by the constant ϵ called the *emittance* and the s-dependent beta function, $\beta(s)$. The local angle with respect to $(x, y, z) = (0, 0, s)$ is then given by

$$\begin{aligned} u'(s) &= -\sqrt{\frac{\epsilon}{\beta(s)}}\left[\sin(\Psi(s) - \Psi(0)) + \alpha(s)\cos(\Psi(s) - \Psi(0))\right] \\ \text{with} \quad \alpha(s) &\equiv -\frac{1}{2}\frac{\mathrm{d}}{\mathrm{d}s}\beta(s) \ . \end{aligned} \tag{4.6}$$

This is also called the *beam divergence*. With the collision point set to $s = 0$, the boundary condition $\Psi(0) = 0$, and the short hand notations $u(0) = u^*$, $u'(0) = u'^*$, $\beta(0) = \beta^*$, $\alpha(0) = \alpha^*$, $\alpha(s) = \alpha$, $\beta(s) = \beta$ and $\Psi(s) = \Psi$, the Equations (4.5)-(4.6) can be conveniently written in the matrix form:

$$\begin{pmatrix} u(s) \\ u'(s) \end{pmatrix} = M_u(s) \begin{pmatrix} u^* \\ u'^* \end{pmatrix} \ , \quad u = (x, y) \ , \tag{4.7}$$

with

$$M_u(s) = \begin{pmatrix} \sqrt{\frac{\beta}{\beta^*}}\left(\cos\Psi + \alpha^*\sin\Psi\right) & \sqrt{\beta\beta^*}\sin\Psi \\ \frac{1}{\sqrt{\beta\beta^*}}\left[(\alpha^* - \alpha)\cos\Psi - (1 + \alpha\alpha^*)\sin\Psi\right] & \sqrt{\frac{\beta^*}{\beta}}\left(\cos\Psi - \alpha\sin\Psi\right) \end{pmatrix} \ . \tag{4.8}$$

The set of parameters in Equation (4.8) is referred to as the *optics*. Knowing the optics parameters, the transverse motion at $z = s$ is a simple linear combination of the point of collision, (x^*, y^*), and the transverse angle (x'^*, y'^*). Hence, the kinematics at the IP can be inferred from a measurement of positions and/or angles at another location in the LHC.

4.4.2 Emittance

The (u, u') phase-space maps out an ellipse with the boundaries

$$u_{\max} = \sqrt{\epsilon\beta} \ , \tag{4.9}$$

$$u'_{\max} = \frac{\epsilon(1 - \alpha^2)}{\beta} \ . \tag{4.10}$$

The shape of the ellipse changes as a function of s, but the area equals $\pi\epsilon$ and is invariant under conservative forces, according to Liouvilles theorem. However, non-conservative forces like energy loss due to ionization and Coulomb scattering between the beam protons can blow up the emittance. It is clear that the emittance should be kept small in order to have a small beam pipe. A larger beam pipe would result in larger and hence more expensive magnets.

The emittance is inversely proportional to the momentum of the protons, hence the emittance decreases when the proton beam is accelerated. Therefore, when one refers to the emittance, it is generally inferred to mean the normalized emittance defined as

$$\epsilon_N = \beta\gamma\epsilon \ , \quad \text{with} \quad \beta = v/c \quad \text{and} \quad \gamma = \frac{1}{\sqrt{1-\beta^2}} \ , \tag{4.11}$$

which is invariant. At normal running conditions, LHC has

$$\epsilon_N \approx 3.75 \text{ mm} \cdot \mu\text{m} \ . \tag{4.12}$$

One of the methods to determine the LHC emittance is by wire scans [21]. A thin wire is moved through the beam in the transverse direction with a speed of 1 m/s. The beam interacts with the wire, and the secondaries are measured with photomultipliers. In that way, the beam profile is determined, and the emittance can be inferred from Equation (4.9) knowing $\beta(s)$. There are in total four wires: one for each beam in horizontal and vertical direction. Each wire scan provides two measurements, namely when the wire is moved inwards through the beam and back again.

4.4.3 ALFA collision optics

From Equation (4.9) it is seen that the transverse size of the beam increases with β^*. Therefore, a small β^* of ~ 0.5 m is used under normal LHC running in order to increase the luminosity according to Equation (4.3) and thereby enhance the observation probability of rare events. During the elastic ALFA data taking, the situation is opposite where a large β^* is used which has two important implications.

First, the beam divergence at the IP is small according to Equation (4.10). The transverse angle in Equation (4.7) is the sum of the elastic scattering angle, θ^*, and the beam divergence, hence according to Equation (3.3) the resolution of the reconstructed four-momentum transfer, t, is diminished if the beam divergence is comparable with the elastic scattering angle.

Second, a large β^* gives access to smaller t-values which enhances the sensitivity to the CNI and Coulomb region in the differential elastic cross section. As will be explained in Chapter 6, the ALFA detectors are moved close to the beam in the vertical direction. The smallest allowed position, y_{min}, is given as a multiple, n, of the size of the beam:

$$y_{\text{min}} = n \cdot \sqrt{\epsilon\beta} \ . \tag{4.13}$$

With $\Psi \approx \pi/2$ and a small α^*, the position of a scattered proton at the ALFA location is given by (ignoring the beam divergence):

$$y \simeq \sqrt{\beta\beta^*}\theta_y^* \tag{4.14}$$

which gives a minimum accessible four-momentum transfer of

$$-t_{\min} = p^2 n^2 \frac{\epsilon}{\beta^*} \,. \tag{4.15}$$

The divergence and $t_{\min}$ also scales with the emittance. However, the emittance should not be too low since a low emittance typically comes with the cost of less protons in the bunches. This reduces the luminosity (Equation (4.3)), which will then limit the number of collisions.

Another aspect of the special ALFA optics is $\Psi \approx \pi/2$ and small α^* in the vertical plane. This gives a so-called *parallel-to-point* optics where the vertical position in ALFA is independent of the point of collision. Not only does this give a more precise determination of the vertical scattering angle, but it is also used in the calibration of the ALFA detector. Unfortunately, the parallel-to-point optics can not be obtained simultaneously in the horizontal and vertical plane.

5 | The ATLAS detector

ATLAS (A Toroidal LHC ApparatuS) is a multi-purpose detector located at the LHC IP 1. Among others, the ATLAS analyses span over measurements of the Higgs boson and searches for supersymmetry to precision measurements of SM processes. This chapter gives a brief overview of the ATLAS detector with focus on the parts relevant for the elastic analysis. The ALFA subdetector built for elastic scattering is the subject of the next chapter. ATLAS is described as it was in LHC run 1, since the data analyzed in Part III was taken in 2012. The information is from Ref. [22] and [23].

5.1 Sub-detectors

ATLAS consists of several sub-detectors, each with its own specific purpose. An illustration is shown in Figure 5.1.

The Inner Detector (ID) is closest to the beam pipe and comprises the Pixel, SCT, and TRT sub-detectors. Its main task is the reconstruction of tracks from which the momentum of charged particles are deduced. Furthermore, the primary collision vertex can be found by extrapolation of the tracks to their intercept with each other. The number of reconstructed vertices can be used in the ATLAS luminosity determination.

The Liquid Argon and Tile calorimeters measure the energy of the particles by absorbing them. Furthermore, the Tile calorimeter is a luminometer in ATLAS when the LHC is in standard high luminosity mode. The Muon system has the largest transverse direction to the beam and measures the momentum of muons.

The Minimum Bias Trigger Scintillators (MBTS) are two detectors of highly efficient scintillator tiles located at each side of the IP at $z = \pm 3.56$ m. Due to their large phase-space coverage they will trigger on nearly all inelastic events including many of the single diffractive processes, which are a background source in elastic scattering.

The Beam Conditions Monitor (BCM) consists of two stations of detectors, one on each side of the IP. The detectors have four modules and each module has two diamond sensors. The diamond sensors are at $z = \pm 184$ cm and $r = 55$ mm. The BCMs are designed to monitor the LHC beams and to trigger a beam dump in case of high losses in order to protect the ATLAS ID. The BCMs are also used to determine the ATLAS luminosity based on the hit rates which are related to the luminosity through the visible inelastic cross section. The luminosity calibration is performed in Van der Meer scans.

LUCID (Luminosity measurements Using Cherenkov Integrating Detector) is designed to measure the ATLAS luminosity by counting the number of inelastic collisions inside

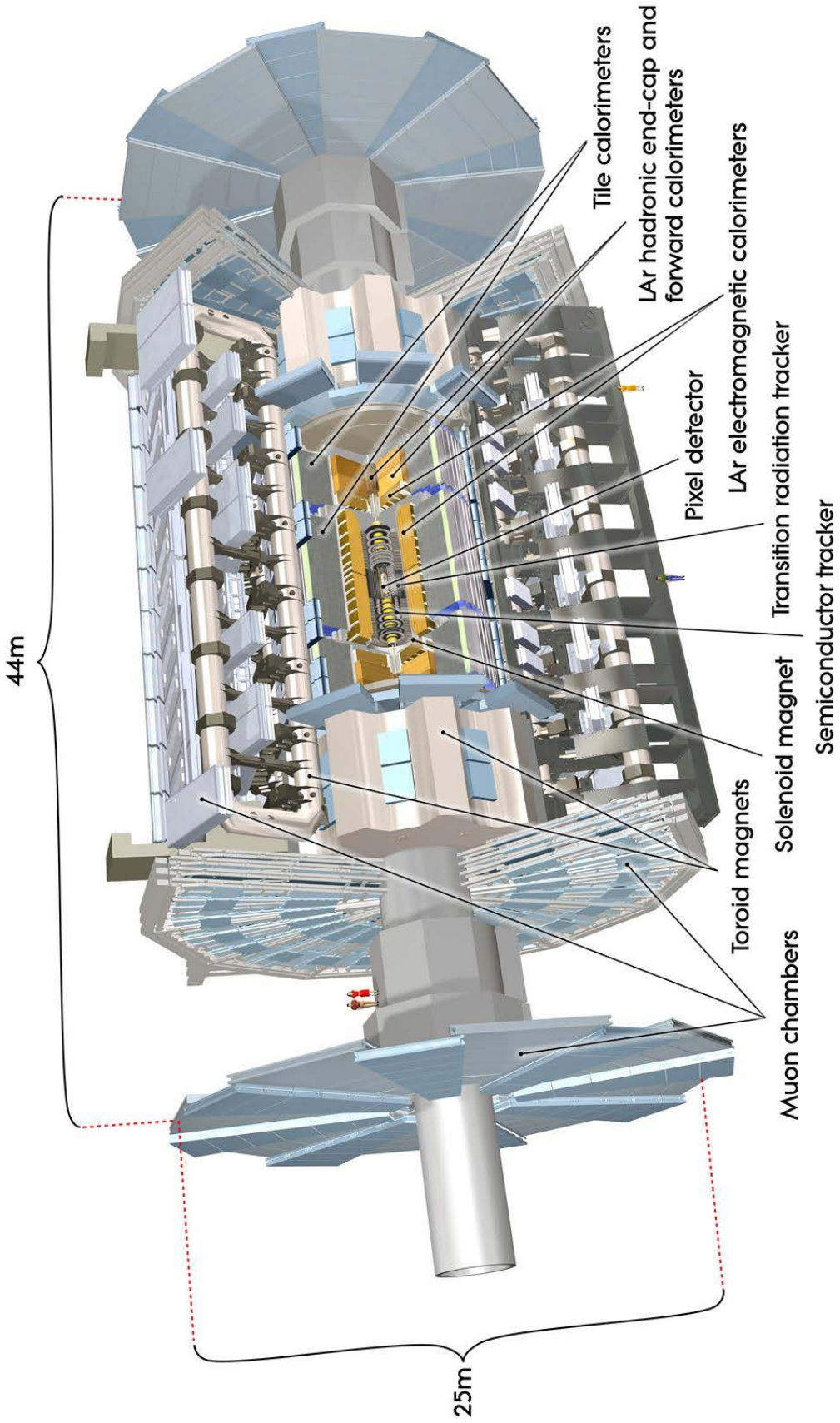

Figure 5.1: Illustration of the ATLAS detector. From Ref. [25].

the LUCID acceptance. LUCID is installed at $z = \pm 17$ m on both sides of the IP. Photomultiplier tubes (PMTs) are used to measure the Cherenkov light produced in 20 aluminum tubes surrounding the beam pipe with a radial distance of about 10 cm. The tubes were originally filled with C_4F_{10} gas but for most of 2012 the tubes were operated under vacuum in order to reduce pile-up effects, and the Cherenkov light was only produced in the window separating the tube and the PMT [24]. The calibration from hit rate to luminosity is performed in Van der Meer scans.

5.2 Trigger system

The bunch crossing rate at the LHC is too high to store all of the information from ATLAS produced by each bunch crossing. Therefore, ATLAS has a trigger system used to select only (a part of) the interesting collisions and thereby bring down the read out rate to an acceptable level.

The Level 1 trigger (L1) is hardware-based and does not use information from the ID as it must be very fast. The Central Trigger Processor (CTP) receives trigger signals from the other sub-detectors. Only if the combination of trigger signals fulfill the logic of any of the CTP items, the event is sent to the Level 2 trigger (L2). The CTP also uses prescales to bring down the event rate. If the prescale for a given item is n, only one out of n events fulfilling that item will be sent to L2.

The L2 trigger uses a computer farm to reconstruct some details of the given event and thereby make a decision on whether or not to sent the event to the High Level Trigger (HLT). The HLT reconstructs the entire event like in offline analyses and makes the final decision to save or discard the event.

6 | The ALFA detector

The Absolute Luminosity For ATLAS (ALFA) detector is designed to measure the angles of elastic scattered protons down to a few micro radians. This chapter gives a description of the parts of the ALFA detector needed to understand the data analysis in Part III. Unless otherwise stated, all information and figures are taken from Ref. [26].

6.1 Detector design

ALFA consists of tracking detectors which measure the positions of protons in the transverse plane to the LHC beam from which the scattering angle can be inferred, as discussed in Section 4.4.1. The detectors are located on each side of the IP at the end of the straight LHC section around ATLAS, which is after the ingoing and outgoing beams are split into separate beam pipes. This large distance to the IP gives the maximum lever arm for the scattered protons and thereby maximizes the separation from the beam protons.

The detectors are placed inside Roman Pots which allows an adjustable distance to the beam center in vertical direction. From a mechanical point of view, the smallest possible distance to the beam center is less than 1 mm, however in practice the size of the beam halo will in most cases determine the distance as described later. There are two stations of detectors on both sides of the IP. No magnets are in between the inner and outer station, which allows both a position and a local angle measurement. Each station is comprised of a lower detector and an upper detector approaching the outgoing beam from below and above, respectively. The detector is split into a Main Detector (MD) used for the actual tracking and two Overlap Detectors (ODs) used for alignment.

An overview of the detectors is shown in Figure 6.1. There exist almost as many naming schemes for the ALFA detectors as there are people in the ALFA group. The official LHC naming scheme will be used throughout this thesis, i.e. B7L1U, B7L1L, A7L1U, A7L1L, A7R1U, A7R1L, B7R1U, and B7R1L. Here, 'B/A' labels an outer/inner detector, '7' indicates that it is the 7th element from the IP, 'L/R' means left/right side of the IP (also known as A-side and C-side, respectively), '1' is because it is around LHC IP 1, and 'U' and 'L' are abbreviations for upper and lower detector, respectively. Due to momentum conservation, an elastic event detected by ALFA will either be in the *elastic arm 1* configuration with signals in B7L1U, A7L1U, A7R1L, and B7R1L or in the *elastic arm 2* configuration with signals in B7L1L, A7L1L, A7R1U, and B7R1U.

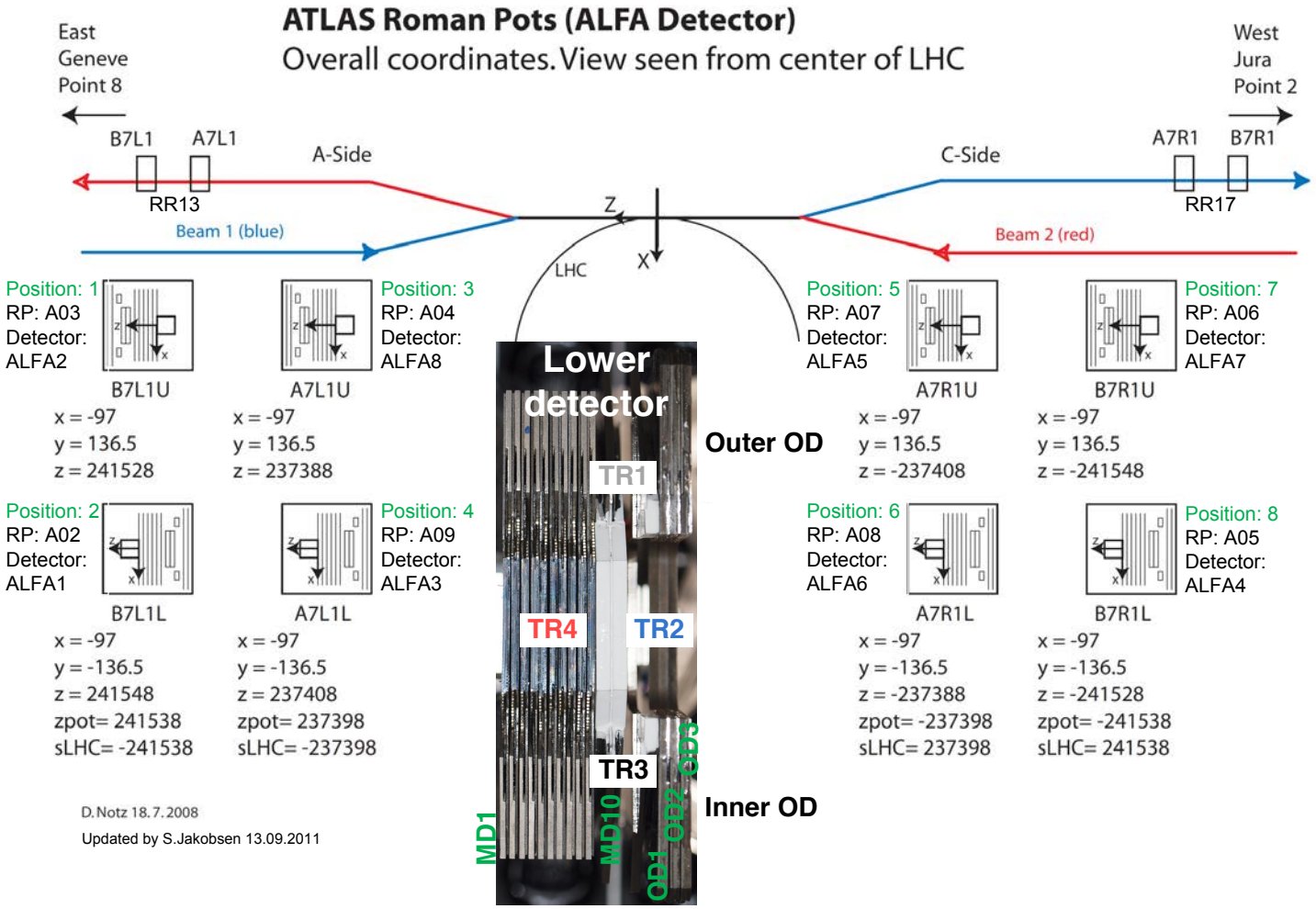

Figure 6.1: Overview of the eight ALFA detectors with their positions, orientations, and naming schemes. The MD1-10 on the picture are the 10 layers of fibers in the Main Detector, OD1-3 are the three layers of fibers in the Overlap Detectors, TR2 and TR4 (TR1 and TR3) are the Main (Overlap) Detector trigger tiles.

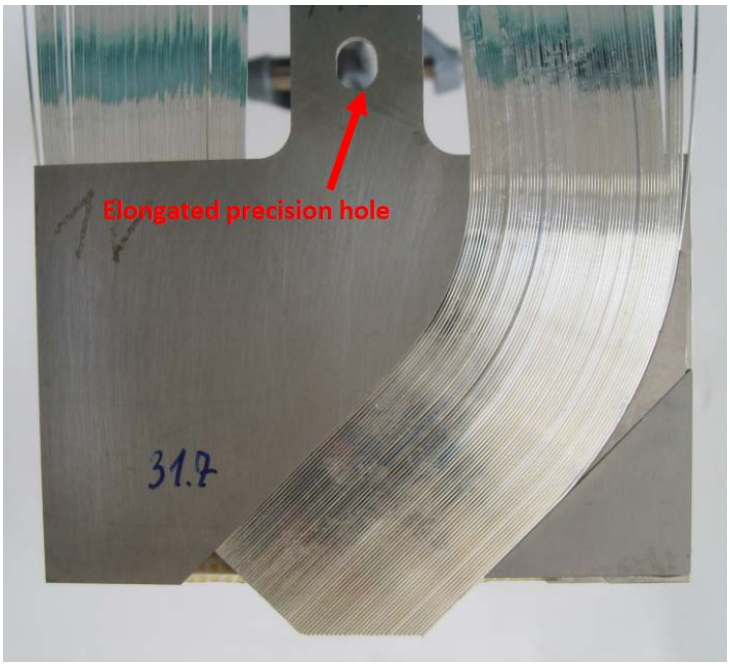

Figure 6.2: Picture of a titanium plate with the fibers for the V(U)-plane glued to the front(back).

6.2 Main Detector

The MD uses scintillating fibers to track the protons in the transverse plane to the beam. The fibers are arranged in layers glued to 10 titanium plates with 64 fibers on one side of the plate and 64 fibers on the other side giving in total 20 layers of fibers. The fibers on the front side of the titanium plate (V-plane) are orthogonal to the fibers on the back side (U-plane) giving a 2D tracking. Figure 6.2 shows one of the titanium plates. Some of the fibers are cut at 45° in order to maximize the acceptance close to the beam, which gives a diamond shaped tracking region. There is no titanium between the fiber layers in the 2D tracking region in order to reduce multiple scattering inside the detector.

The fibers are 0.5×0.5 mm^2 squared fibers, which are cladded such that the produced light is trapped inside the fiber due to internal reflection. The fibers are coated with aluminum to reduce cross-talk where light propagates to a neighboring fiber. The inactive cladding and coating amount to 2.2 % of the total layers width, and the layer efficiency has been measured in a test beam to be around 90 %.

The 10 fiber layers are staggered such that each layer is shifted by 1/10 of the fiber width, which enhances the resolution of the tracks. The resolution is about 30 μm, but it depends on the beam energy and background level and needs to be determined from the data separately for each run.

The fibers of each layer are connected to a 64-channel MultiAnode PhotoMultiplier Tube (MAPMT). There is a risk of cross-talk between neighboring channels in the MAPMT. Therefore, a special mapping of the fibers to the MAPMT channels is used such that neighboring fibers are not neighbors in the MAPMT.

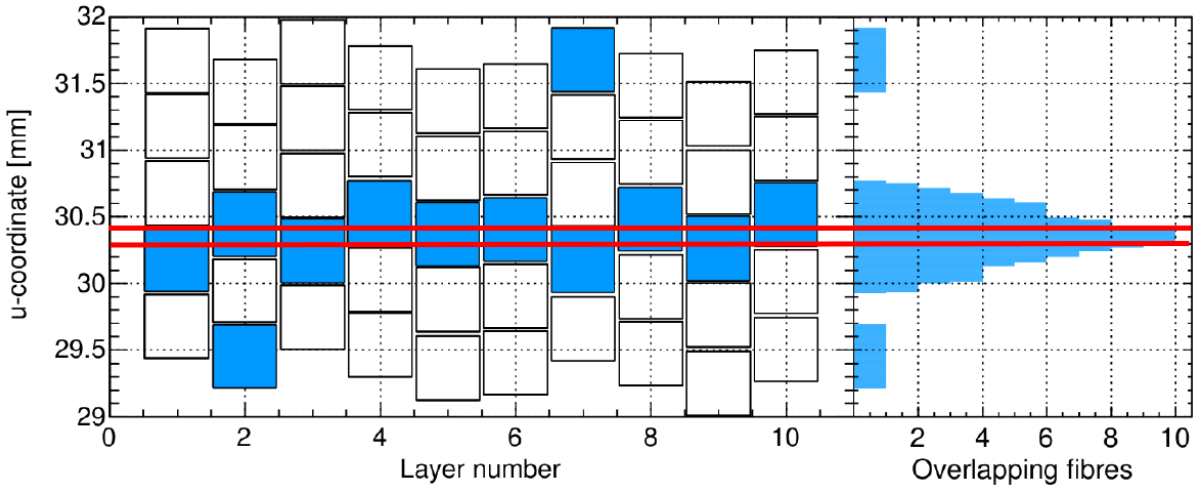

Figure 6.3: Illustration of the track reconstruction principle in the U-plane [27].

6.2.1 Track reconstruction

The track reconstruction principle is shown in Figure 6.3 and explained in detail in Ref. [27]. A traversing proton gives a fiber hit in several of the layers. Assuming that the proton trajectory is perpendicular to the detector plane, the true proton trajectory must be within the boundaries of the red lines, which show the common overlap region of the hit fibers. The reconstructed position of the proton is then the middle of the overlap region, and the size of the overlap is a measure of the precision. This procedure is used in both the U- and V-plane and then translated into (x, y)-coordinates. The coordinates are given wrt. the precision hole in Figure 6.2. This will be referred to as the detector coordinate system, where the MD edge is at $y \simeq -135$ mm.

It is clear that the staggering of the layers gives an overlap much smaller than the size of a fiber. In general, the best precision of a track is therefore obtained when all layers are hit. With perfect staggering, such a track would have a fiber overlap region of only 50 μm corresponding to 1/10 of a fiber width which corresponds to a Gaussian resolution of 14.4 μm. Fiber and MAPMT cross-talk are also important for the precision of the track: If neighboring fibers give a signal, the fiber overlap size will increase. Therefore, the standard track criteria are minimum three overlapping fibers in the track in both the U- and V-plane, and minimum three U-layers and three V-layers with maximum three fiber hits. The specific track criteria change from run to run, and the track reconstruction efficiency and detector resolution are determined from the data for each run.

The scenario with multiple tracks needs careful investigation in ALFA. If two protons hit ALFA, there will be two tracks in both the U- and V-plane with no information about which U-track belongs to which V-track. Therefore, four track candidates will be saved and the ambiguity is handled in the offline analysis.

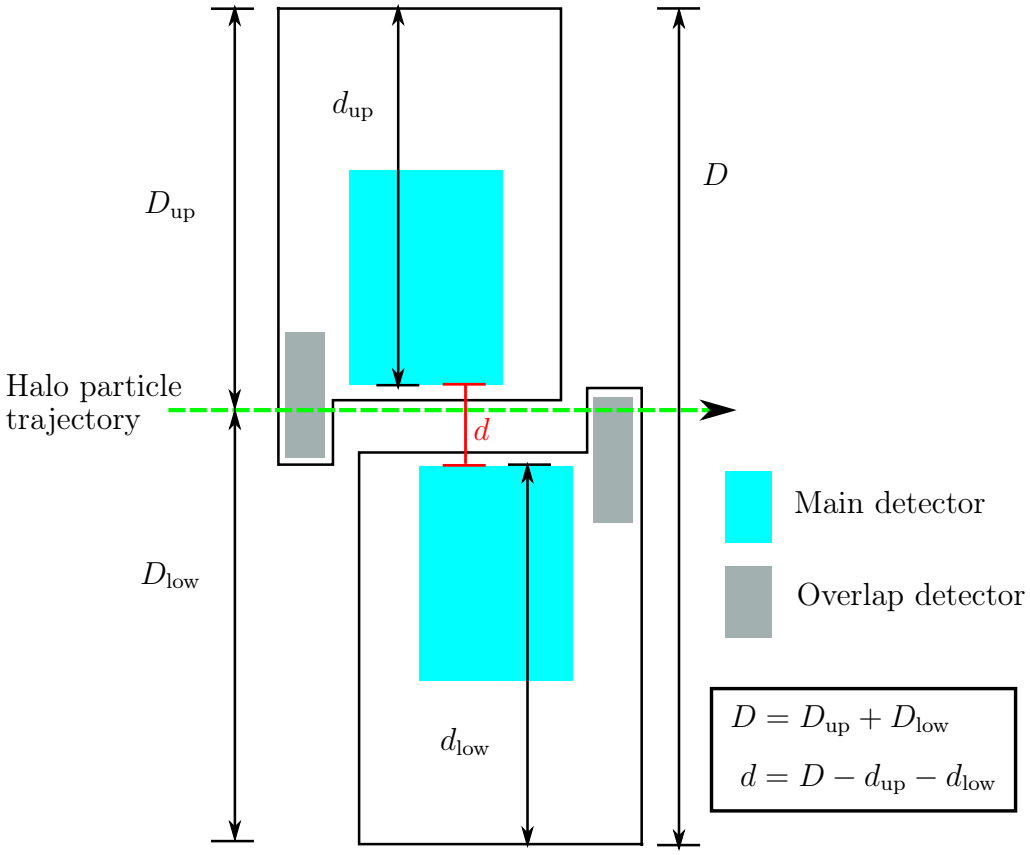

Figure 6.4: The principle behind the distance measurement. The original figure is from Ref. [28].

6.3 Overlap Detector

The ODs are placed on both sides of the MD in horizontal direction and are used to find the distance between the edges of the upper and lower MD in a station. The idea is illustrated in Figure 6.4 where a particle traverses both the OD belonging to the upper detector and the OD belonging to the lower detector. Knowing the vertical position of the particle in each OD and the calibration constants d_{up} and d_{low}, the distance, d, can be inferred. The actual distance measurement using an ensemble of traversing particles is described in Section 7.1.

The positions of the ODs with respect to the MD and the LHC beam pipe are shown in Figure 6.5. The horizontal distance from the inner vertical OD edge to the beam center is 19 mm, hence only halo particles are expected to be observed in the ODs. LHC beam screens at $x = 18$ mm are located only four meters before the inner ALFA stations. This means that either the halo particles must have a horizontal angle of at least 1/4000 radians to hit the ODs, or only shower events will hit the ODs where the noise level is high. In a calibration run performed in 2015, the author observed that the OD trigger rates in the outer stations increased when the inner stations scraped the beam, hence shower events are non-negligible. The ODs belonging to the lower (upper) detector is placed in

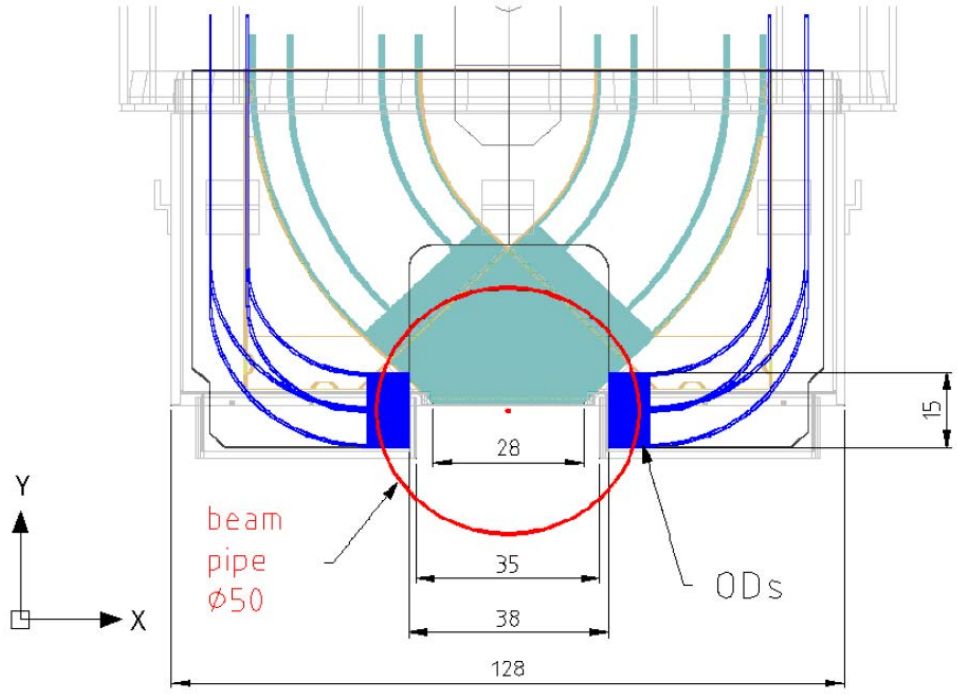

Figure 6.5: Orientation of the ODs (blue) wrt. the MD (green). From Ref. [29].

front of (behind) the MD in the direction of the proton. This gives a distance of about 4 cm between the upper and lower OD in the z-direction, which plays an important role in the distance measurement.

The vertical positions of the ODs wrt. the MD are chosen to maximize the overlap between the upper and lower OD when the detectors are in design data taking position. They will start to overlap when the MD edges are 8.5 mm from the beam center.

The ODs are build of the same kind of scintillating fibers as the MD, the difference being that there are only three fiber layers and only in the horizontal direction. Each layer consists of 15 fibers glued to each side of a titanium plate. The fibers are bent outside the range of the titanium plate in order to be connected to MAPMTs. The active area where the fibers are horizontal and useful for vertical tracking is 15×6 mm^2. In contrast to the MD, there is more than 0.5 mm titanium between the fiber layers, which gives an enhanced probability for shower development and multiple scattering inside the OD. The fibers are cut at 90° and have an aluminum coating used as a mirror to reduce optical cross-talk. The three layers were designed to be staggered by 1/3 of a fiber width to improve the resolution of the tracks. Unfortunately, the staggering is far from the intended design, resulting in fiber overlap sizes as small as 1 μm and as large as 380 μm. This is far from the 133 μm overlap size which would have been the case with perfect staggering, and it plays an important role in the distance measurement.

The OD fibers are connected to MAPMTs, like the fibers in the MD. The 30 fibers in the first layer share an MAPMT with the first OD layer on the other MD side. Cross-talk between the two ODs is therefore possible. No neighboring fibers are neighbors in the MAPMT in order to reduce the combined effect of optical and MAPMT cross-talk.

6.3.1 MD-OD calibration

The calibration of the relative positions between the ODs and the MD edge was performed in a test beam campaign in 2010 using a EUDET telescope. The MD edge was measured and also the individual positions, slopes and widths of 20 out of the 30 fibers in each OD layer was determined [28]. EUDET did not cover the five outer-most fibers in the top and bottom, hence the positions of these fibers were estimated from the 20 measured fibers.

The relative position between the MD and ODs is a convoluted effect of the OD fiber positions, MD edge measurement and the alignment between EUDET and ALFA. The combined uncertainty is obtained by adding the different uncertainty contributions in quadrature. The values are 80 μm, 8 μm, 9 μm, and 8μm for B7L1, A7L1, A7R1, and B7R1, respectively. The large uncertainty for B7L1 is because B7L1U was not part of the test beam campaign as it was already installed in the LHC.

As seen on Figure 6.5, there is a small overlap region between the ODs and the MD of about 1 mm^2. The author has investigated whether the overlap can be used to find the relative vertical distance between the MD and ODs since an apparent miscalibration has been observed in the elastic data analysis. In the ATLAS run 206881, events were selected where both the MD and the OD have a track in the overlap region. Plotting the difference in y-coordinate between the MD track and the OD track, a miscalibration would result in a distribution with a mean different from zero. Unfortunately, the overlap region is so small that less than 100 events were recorded in each detector and a precision better than 100 μm were impossible to achieve.

6.4 Roman Pot

The ALFA detectors need to be moved inside the LHC beam pipe in order to find the best data taking position. Therefore, the detectors are placed inside Roman Pots, which separate the detectors from the ultra high LHC vacuum and hence allows the movement from an LHC protection perspective. A picture of an ALFA Roman Pot is shown in Figure 6.6. The Roman Pots are connected to a motor with a step size of 5 μm which is needed to obtain a precise alignment to the beam. The beams are not necessary located exactly in the center of the beam pipe but can be off by several hundreds of micro meters. Therefore, a Beam Based Alignment (BBA) procedure is used. A Roman Pot is moved to a not so distant but still safe distance to the beam. This position is calculated from the nominal emittance of the beam and the β function. The Roman Pot is then moved at a step size of 10 μm until a sudden increase in the LHC Beam Loss Monitor located right after the ALFA stations shows that the Roman Pot scrapes the beam and produces shower events. The alignment to the beam for that Roman Pot is now known and the detector is moved outwards to the physics data taking position. This position needs to comply with the LHC safety rules which depend on the properties of the beams. The position can be several standard deviations of the beam size. The same procedure is used for the other Roman Pots and it takes about 2-3 hours to perform the entire BBA.

The Roman Pot thin window has a thickness of only 200 μm. This allows to reduce the distance between the outer window edge and the MD edge to about 450 μm. This

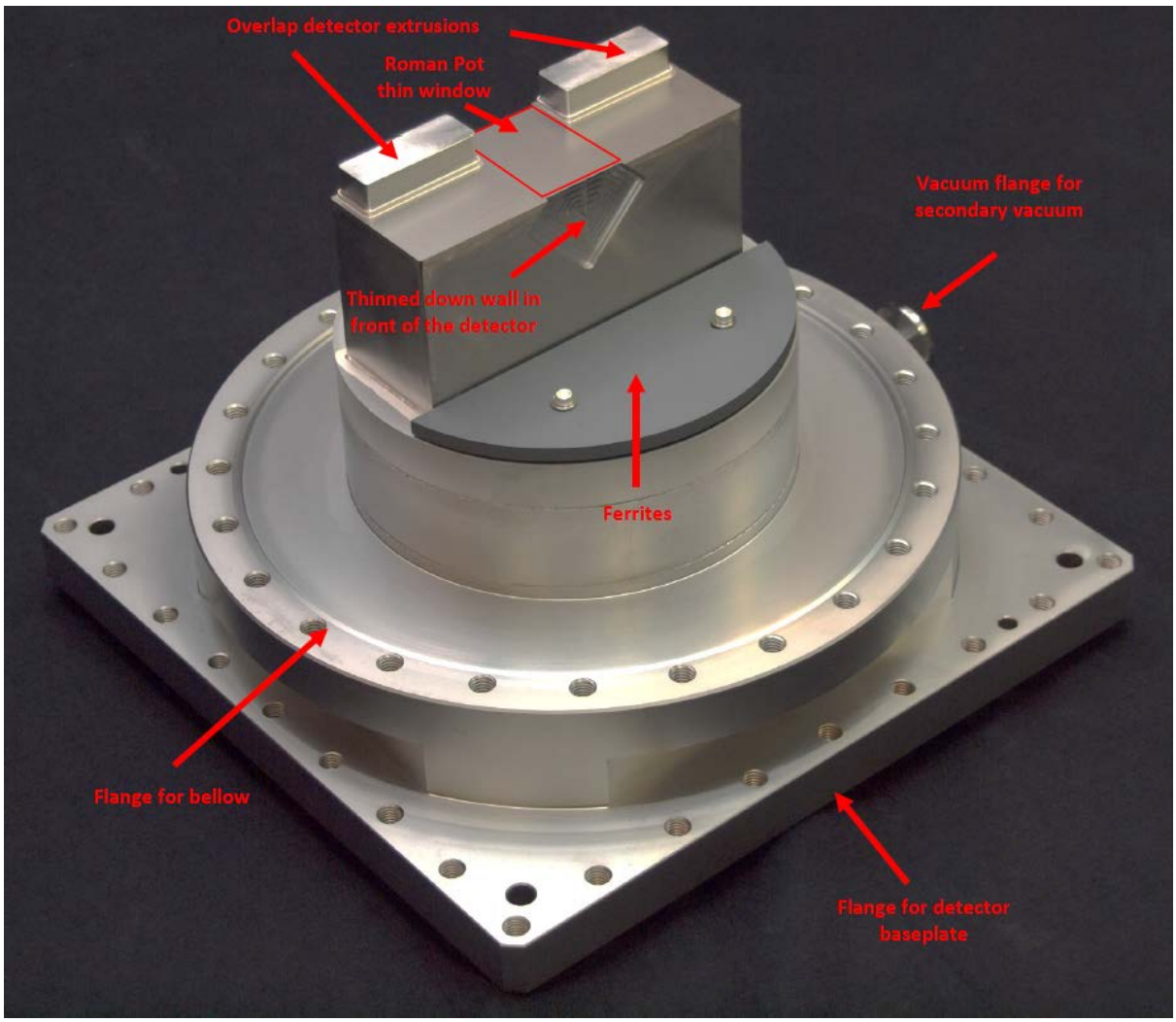

Figure 6.6: Picture of an ALFA Roman Pot.

distance should naturally be as low as possible in order to get close to the beam with the detector. There is a secondary vacuum inside the Roman Pot such that the pressure on the window is minimized. Without this vacuum, the window would bent (more) outwards, reducing the possible detector distance to the beam.

The thinned down wall in front of the detector is 500 μm thick and has the same shape as the MD. It should be as thin as possible to reduce the probability of interactions with the elastic protons while not making a risk for the vacuum. In general, the outer detectors have a 10 % worse tracking resolution than the inner detectors, which is explained by interactions with the Roman Pot and detector material.

6.5 Trigger system

The ALFA detectors are connected to the ATLAS CTP L1 menu with air-core cables which have a transmission speed of 91 % the speed of light. Due to the large distance of 240 m to ATLAS, the high transmission speed is crucial to ensure fast enough readout.

The MD tracking region is covered by two plastic scintillator tiles with a thickness of 3 mm each. A coincidence between the two tiles sends a signal to the CTP. The requirement of a coincidence is used to reduce noise from the trigger PMTs. For most of the detectors, the trigger tiles extend the MD tracking region by up to 100 μm. However, for detector A7L1L the tiles do not cover the 70 μm closest to the detector edge, and this needs to be dealt with in the offline data analysis. A single trigger tile covers the active OD area of 15×6 mm^2. Only one tile is used since a coincidence between one of the upper ODs and one of the lower ODs in the same station is needed for a signal to be sent to the CTP.

The events are read out in two streams, the calibration stream and the physics stream. The calibration stream contains only ALFA information as well as the trigger information sent to the CTP by the rest of the ATLAS sub-detectors. This means that the event size is small and events can be read out at a very high rate. In most cases, the L1_ALFA_ANY trigger is unprescaled in the calibration stream, meaning that a signal from any of the eight MDs causes a read out of the event. The physics stream contains full ATLAS information about the event, hence the read out rate must be much lower than for the calibration stream. Therefore, ALFA has several L1 CTP items where there is a requirement for a coincidence between some of the MDs. The two most important L1 items are L1_ALFA_ELAST15 and L1_ALFA_ELAST18 with the logic:

$$\text{logic}_{\text{L1\_ALFA\_ELAST15}} = \text{(B7L1U OR A7L1U) AND (A7R1L OR B7R1L)}\,, \tag{6.1}$$

$$\text{logic}_{\text{L1\_ALFA\_ELAST18}} = \text{(B7L1L OR A7L1L) AND (A7R1U OR B7R1U)}\,. \tag{6.2}$$

The logic is strict enough to use the two items unprescaled in the physics stream while the trigger efficiency for elastic events is still close to 100 %. The exact trigger efficiency is determined from the data for each run.

7 | ALFA detector calibration

This chapter describes parts of the detector calibration carried out by the author. It includes the distance measurement, the high voltage optimization for the ODs, online distance histograms, and elastic trigger efficiency determination.

7.1 Distance measurement

The distance between the MD edges in a station is paramount in order to find the scattering angle in an elastic event. Without this distance, the tracks measured by the MDs in the detector coordinate system can not be translated to the coordinate system of the beam used in the data analysis. The distance is found using tracks in the ODs as was shown in Figure 6.4: A particle gives a track in both the upper and lower OD from which the distance can be found knowing the relative MD-OD distance. The uncertainty on the distance measurement can be reduced by combining many such events, but the procedure to do so is not trivial. This section describes the distance measurement procedure developed by the author for the physics analysis in Ref. [11]. All presented results are from this data set, but the procedure is generic and is intended for all future data sets.

The ODs have only three fiber layers which give a less precise determination of the actual particle trajectory. Furthermore, the staggering of the layers is for some of the ODs very poor, hence the size of the overlap between fibers in the different layers can be as low as 1 μm and as large as 380 μm. This gives different precisions on the particle trajectories, and the effect must be taken into account to obtain the most precise distance measurement. If this fact is ignored in the distance measurement - for instance by just taking a mean of the single particle distances - the result will not only be less precise, but can in fact have a bias by up to 30 μm, which is then quoted as a systematic uncertainty (Figure 6.17 in Ref. [28]). For the data presented here, the distance between the MD edges was so large that the overlap between the upper and lower OD corresponded to only about three fiber widths. Therefore, the bias from a simple mean or Gaussian fit is expected to be even larger and a proper procedure was needed.

Since the ODs have only three fiber layers, only tracks where all three layers are hit will be considered. A track in a single OD will be referred to as a *tracklet*, whereas *track* is used for the combined tracklets in the upper and lower OD. The positions and sizes of the tracklets are solely given by the positions of the fibers in the ODs, whereas the position of the track is a function of the distance between the MD edges.

The basic idea behind the distance method is to look at the rates of all possible

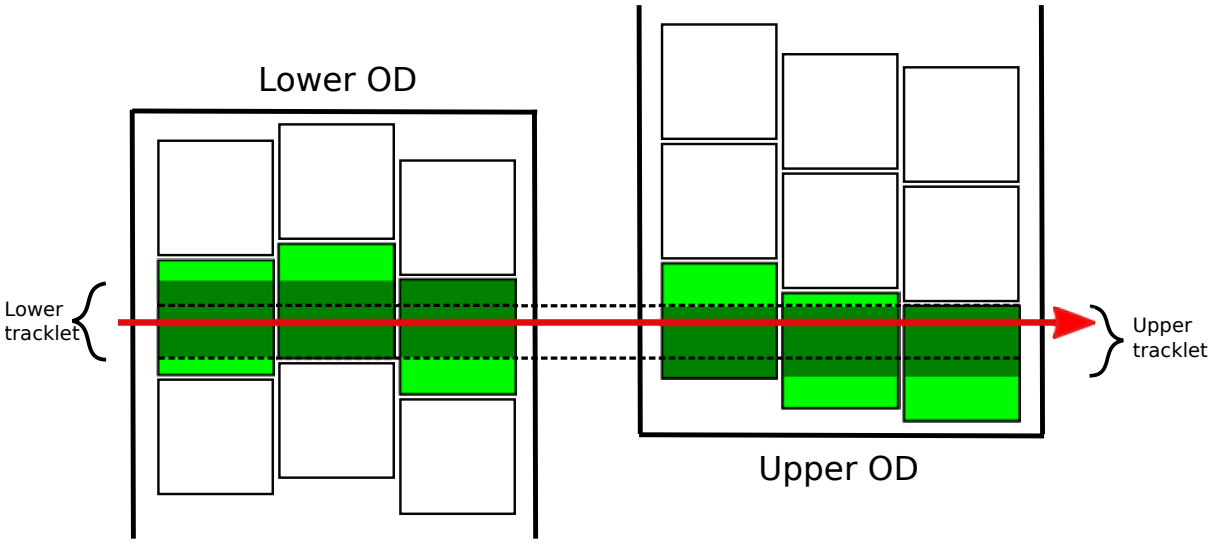

Figure 7.1: Principle behind the distance procedure: A particle (red arrow) traverses the ODs and illuminates the fibers (squares with green color). The size of the tracklet inside an OD is given by the individual fiber boundaries (dark green area), whereas the vertical range for the combined track (inside the dashed lines) is given by the relative positions of the two tracklets and thereby the distance. The illustration is not to scale.

combinations of tracklets in the upper and lower ODs and compare to the expectation from a simulation with varying distance between the MD detectors edges.

7.1.1 Distance procedure

The distance measurement is treated by counting the number of events in each tracklet combination in the ODs. It can be explained from Figure 7.1 where a traversing particle enlightens fibers which gives a tracklet in both the lower and upper OD. The possible vertical range for the trajectory is limited by the overlap of the two tracklets which depends on the distance. The larger the overlap, the larger probability for the combination of those two tracklets. If the upper OD is moved downwards wrt. the lower OD (i.e. if the MD edge distance is decreased), the area between the dashed lines will decrease and the probability for that track will decrease and hence also the counting rate. However, other tracklet combinations will now be more probable, and the counting rates can be translated into a distance. The procedure is similar to the originally proposed distance method [30], but the refined method presented here takes into account the 'as built' detector with non-uniform tracklet sizes.

With three fiber layers and 30 fibers in each layers, all ODs can have up to about 100 different tracklets giving up to 10000 different possible tracks for each side in a station. The track pattern generated by a sample of particles can be described by a histogram with track number on the x-axis and number of events on the y-axis. An example is shown in Figure 7.2 for the negative side in station B7L1. The high peaks belong to real tracks where the tracklets in the upper and lower OD come from the same particle, whereas many of the low peaks belong to background events consisting of the combination

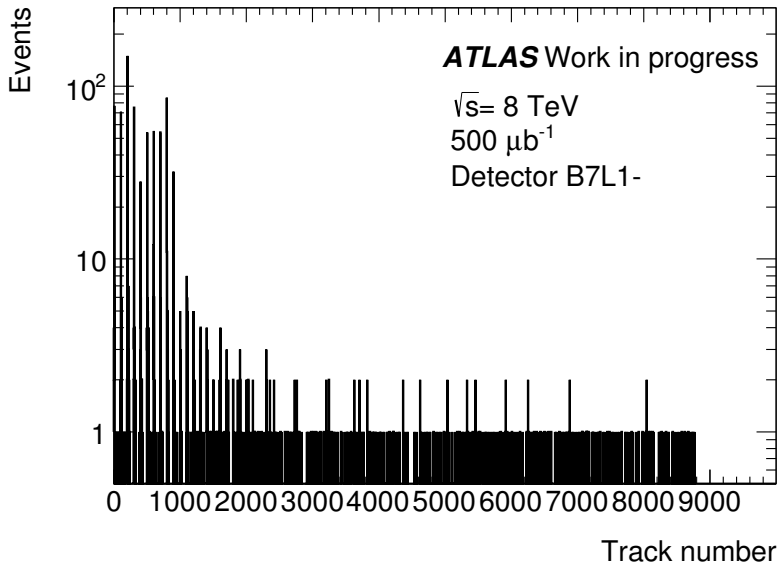

Figure 7.2: Track pattern in the ODs in negative side of station B7L1. The track number is a unique combination of the tracklet number in the lower and upper OD, but the value itself has no physical interpretation.

of uncorrelated tracklets. A low peak can of course also come from a real track with low probability due to a small overlap area.

To determine the distance, the track pattern in the data is compared with corresponding patterns from simulation. Templates that resemble the signal are Monte Carlo (MC) produced for all possible distances in steps of 1 μm using the measured fiber positions and widths in the ODs. In addition, a distance-independent background template is MC produced from uncorrelated tracklets. The similarity between the data and the signal plus background template is found by minimization of a likelihood function based on Poisson statistics:

$$L = \prod_k \frac{e^{-N_k^{\mathrm{sig}}(d)\cdot p_{\mathrm{sig}} - N_k^{\mathrm{back}}\cdot p_{\mathrm{back}}} \cdot \left(N_k^{\mathrm{sig}}(d)\cdot p_{\mathrm{sig}} - N_k^{\mathrm{back}}\cdot p_{\mathrm{back}}\right)^{N_k^{\mathrm{data}}}}{N_k^{\mathrm{data}}!}\,, \tag{7.1}$$

where the multiplication is over all the different tracklet combinations and N_k^{sig}, N_k^{back}, N_k^{data} is the number of events in the k'th combination in the signal template, background template and data, respectively. Whereas N_k^{back} (and of course also N_k^{data}) is constant, the N_k^{sig} changes with the distance used in the construction of the template. The sum of signal and background events in a tracklet combination is treated as the theoretical mean around which the number of data events fluctuates. The level of signal and background (p_{sig}, p_{back}) are the fit parameters.

The distance is determined from the value of $-2\ln(L)$ as a function of the distance. The resulting distance is chosen as the midpoint of the one standard deviation interval in order to have symmetric statistical uncertainties.

7.1.2 Selection criteria

A number of selection criteria must be applied for the distance measurement. The cut flow and efficiencies are of no interest as long as the number of statistics is large enough:

1) Only luminosity blocks where the ALFA detectors are in data taking position are selected. Otherwise, the computed distance will be a mixture of different physical distances. The standard physics analysis requirement of a luminosity block duration above 60 seconds is not applied, since problems with other parts of ATLAS have no influence on the ALFA ODs.

2) Due to the construction of the ODs, it is necessary to require that the trigger tiles in both the upper and the lower OD have fired, since the fibers bend outside the area covered by the tiles and a track in bend fibers will give a wrong distance.

3) A veto on the trigger tiles in the MD and in the ODs on the other x-side of the MD are used to reduce the probability of shower events in the beam pipe before the ALFA station. Shower events are problematic for the distance measurement because they enhance the probability of uncorrelated tracks as well as particles with large angles. The effect of particle angles are problematic for the distance measurement as discussed later.

4) A requirement of a trigger in the upper and/or lower OD in same x-side in the other ALFA station on the same side of the IP is used to reduce the amount of tracks with large angles.

5) The CTP item for OD coincidence in the ALFA station in question must have fired and no other CTP items before prescale must have fired except for OD coincidence in the other ALFA stations. This is to avoid trigger bias in the investigation of the vertical track distribution in Section 7.1.3.

6) Exactly one reconstructed tracklet in both the upper and lower OD is required, since a distance for an event where one or both tracklets are missing is impossible to deduce. Furthermore, the tracklets must be *isolated*, meaning that none of the neighboring six fibers to the tracklet must be hit. This is a very strict cut, but it is absolutely necessary because the simulation used for the signal templates does not include cross-talk between the fibers, hence there is no possibility to simulate non-isolated tracklets. Events with multiple tracklets are rejected in order to reduce background events.

7) At least one layer in each of the ODs should be *clean*, meaning that it has only one fiber hit. This reduces the probability of fake tracklets coming from noise.

8) A veto on fiber hits in the ODs on the other side of the MD is used to reduce fake fiber hits from MAPMT cross-talk. As decribed in Section 6.3, one layer in the positive OD and one layer in the negative OD share the same MAPMT and the cross-talk could possibly give fake tracklets.

The selection criteria are chosen to reject as much background and noise as possible while assuring that the statistical uncertainty is not dominating the precision of the distance measurement.

Event categorization

With the cuts described above, the sample is almost as free of background and noise as possible, but the remaining events are still classified according to their noise level. It is reasonable to assume that an event where all layers are clean gives a better measure of the distance than an event where only one layer in each OD is clean. This classification serves as a stability check of background effects. The events are divided into three classes:

Class 1: All three layers in both ODs are clean.

Class 2: At least two layers in both ODs are clean, excluding events from class 1.

Class 3: At least one layer in both ODs are clean, excluding events from class 1 and class 2.

Each class is fitted individually with the signal and background templates to find the distance. Afterwards, the $-2\ln(L)$ for the three classes are added together to find the combined distance. In this way, the $-2\ln(L)$ takes into account the relative weight between the three classes.

7.1.3 Input parameters to the template construction

In order for the templates to resemble data as much as possible, a proper probability distribution of positions and angles of tracks in the ODs must be given as input to the template construction. These input parameters will either be estimated from the data in the following or simply included in the likelihood function as nuisance parameters.

Horizontal track distribution

The horizontal distribution of tracks in the ODs is important because the OD fibers are not perfectly horizontal. A particle hitting the OD on the inner edge closest to the beam can have a different position than a particle hitting the OD on the outer edge even though the same fibers have been hit. Therefore, the profile must be determined and given as input to the template construction.

The horizontal profile is estimated from MD data, since the ODs do not have tracking in the horizontal direction. Events are selected with a trigger in the MD and only one reconstructed track, and the hitmap is shown in Figure 7.3 for the inner ALFA detector A7R1L. Only tracks inside the area indicated by the red lines are suitable for an estimation of the horizontal track distribution. Tracks below the MD lower edge comes from fake tracks, and tracks above the red lines are a mixture of fake tracks and other background sources which will not be present in the ODs. The upper boundary is determined manually where there is a clear drop in density of tracks and it varies between the detectors. The

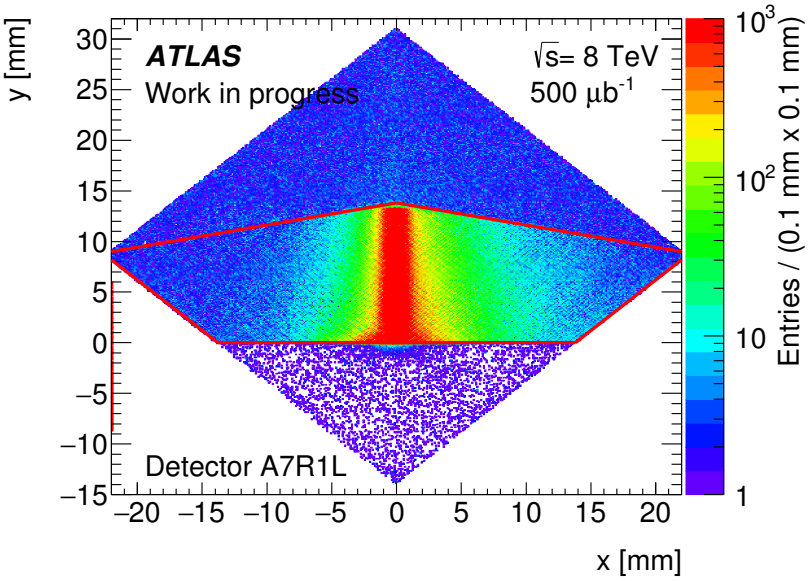

Figure 7.3: Hitmap in the Main Detector A7R1L. Red color is overflow. No horizontal alignment has been performed, and the MD edge position is set to $y = 0$ mm.

drop is understood as an effect of the LHC beam screen. The drop is more pronounced for positive x-values[1]; therefore the boundary on the negative side is determined as a mirror of the positive boundary.

The profile for the OD is estimated from tracks with 6 mm $< y <$ 8 mm as this gives the largest possible range in x, and the larger x, the better overlap with the OD horizontal coverage of 19 mm $< |x| <$ 25 mm. Going to slightly larger values in y will increase the x-range but it will be too close to the upper boundary.

A projection on the x-axis of the selected tracks is shown in Figure 7.4 as the black curve for the positive side of detector A7R1L. The rapid decrease at $x \sim 20$ mm is due to the MD geometry and should not be considered as information about the OD track distribution. An exponential fit in the range 13 mm $< |x| <$ 19 mm is chosen to describe the profile and is extrapolated to the OD horizontal range. The fit range is chosen as the same size as the OD horizontal range and in the region closest to the OD without including edge and geometry effects in the MD. The fit range must be so large that the extrapolation is a valid procedure but small enough not to include effects that will never be present in the ODs, e.g. elastic events. The final estimation of the horizontal track distribution is then an average of the fit in the upper MD and the fit in lower MD since the overlap region of the ODs must share the same distribution.

The difference in final distance between using the black fit in Figure 7.4 and using the red fit is taken as a one standard deviation systematic uncertainty due to the horizontal track distribution. The red curve is a projection of events with 1 mm $< y <$ 3 mm and is an attempt to go closer in vertical direction to the position where the ODs overlap at $y \simeq -8$ mm. The 1 mm distance to the MD edge is to exclude edge effects. The

[1]Diffractive events tend to move in this direction due to their energy loss [31].

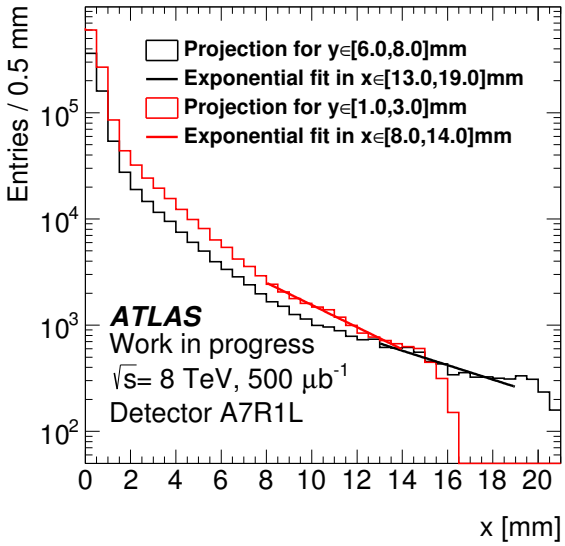

Figure 7.4: Horizontal profile for main detector A7R1L. The black curve is the nominal and the red curve is for the systematic uncertainty.

Detector	Nominal [mm^{-1}]	For systematics [mm^{-1}]
B7L1U	-0.089 ± 0.006	-0.243 ± 0.003
B7L1L	-0.107 ± 0.006	-0.220 ± 0.004
A7L1U	-0.163 ± 0.008	-0.260 ± 0.004
A7L1L	-0.151 ± 0.007	-0.253 ± 0.004
A7R1U	-0.161 ± 0.008	-0.252 ± 0.005
A7R1L	-0.157 ± 0.008	-0.240 ± 0.005
B7R1U	-0.115 ± 0.006	-0.233 ± 0.004
B7R1L	-0.070 ± 0.007	-0.231 ± 0.004

Table 7.1: Slopes for the exponential fits describing the horizontal track distribution. The uncertainties are statistical only.

downside of this projection is that the fit range must now be chosen further away in horizontal direction from the ODs than with the nominal black curve, and the distance to the OD overlap region is still about 9 mm. Again, an exponential fit is chosen but now in the range 8 mm $< |x| <$ 14 mm with the same reasoning as before. The exponential slopes for all eight detectors for both the nominal black curve and the red curve used for systematics are listed in Table 7.1.

Vertical track distribution and efficiencies

The nominal setting for the template construction is a flat vertical track profile and 100 % efficient fibers and MAPMTs. Any deviation from this assumption will change the number of events in a given tracklet and thereby the entire template and hence also the distance measurement. Since the overlap between the ODs is only about three fibers,

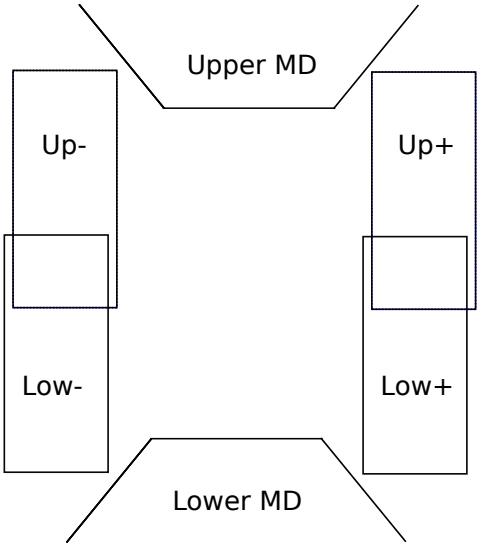

Figure 7.5: Sketch of the ODs in an ALFA station, where Up/Low is the upper/lower OD and +/− is positive/negative side. Lower ODs are slightly displaced to show the overlap region. The sketch is not to scale.

efficiency differences can have an important effect on the signal templates. The vertical track profile, fiber efficiencies and MAPMT efficiencies can not be separated, and no clear knowledge about the three effects is currently available. However, a rough estimation of the combined effect can be observed directly from the OD data.

The determination of the vertical profile must not be influenced by a bias due to the trigger logic in the ODs. The CTP logic for the ODs is

$$((\text{Up}- \text{ OR } \text{Up}+) \text{ AND } (\text{Low}- \text{ OR } \text{Low}+))$$

with the naming convention from Figure 7.5. When selecting events with this trigger item, the distribution of tracks in for example Up+ will therefore have an excess in the overlapping region with Low+, whereas an additional veto on the trigger in Low+ will give too few events. Assuming no correlation between particles in the two sides, the unbiased distribution of tracks in say Up+ is therefore found by requiring a trigger in Up+ and Low− with no selection depending on Low+.

It is not possible to determine the vertical profile using events triggered by something else than OD coincidence but still with some OD activity, e.g. an elastic event in coincidence with a halo particle in the OD. The events used for the distance measurement and the events used for the vertical profile must be triggered by the same CTP item, since the OD pattern turns out to be highly dependent on which type of physics triggered the event. Not even events selected with a random trigger can be used, as this will be a mixture of different physics processes. If selection criterion no. 5 in Section 7.1.2 is not used, the events used for the distance measurement will be a mixture of physics processes. It will be impossible to use the exact same mixture for the vertical profile estimation, hence the input to the signal templates will be wrong which will bias the final distance.

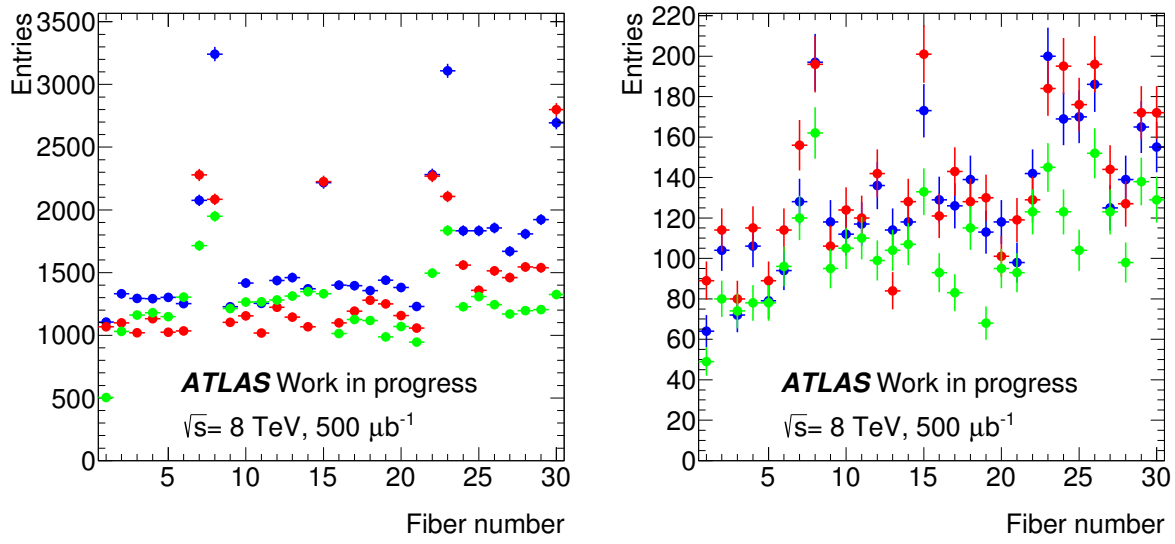

(a) Loosest cuts.

(b) Minimum one overlapping fiber.

Figure 7.6: Fiber hits for detector A7R1U+ used to determine the convoluted effect of the vertical track profile and efficiencies. The error bars indicate the statistical uncertainty. Blue is OD layer 1, red is layer 2, and green is layer 3.

The rates of the individual fibers in an OD is used to scale the signal and background templates instead of the rates of the tracklets themselves. In contrast to the tracklets, the individual fiber rates are independent of the particle angle, and a given combined track in the template is simply scaled by the six fiber rates (3 fibers in each OD).

Events are selected similar to the events for the distance measurement except that for e.g. Up− nothing is required about Low−. The fiber rates for a given layer is found when the layer has only one fiber hit and is shown in Figure 7.6a for detector A7R1U+. The higher the fiber number, the closer we are to the beam center in the vertical direction and as expected there is a slight increase. However, a more striking feature of the plot are the spikes at fiber number 7, 8, 15, 22, 23, and 30, which are more significant than statistical fluctuations, and similar spikes are present for almost all the detectors. Another selection criterion has been used in Figure 7.6b in order to investigate the spikes. Here, the fiber in question should overlap with at least one hit fiber from any of the two other layers, i.e. maximum one fiber hit is missing to have a tracklet. A slight bias is introduced with this method as the rates will depend on how much the fiber overlaps with the other two layers. This bias can be particularly important for the outer-most fibers where the fiber staggering results in a small overlap with other fibers. The cut reduces the spikes, hence it is concluded that the spikes are due to noise. In Figure 7.7, the fiber rates are mapped to the MAPMT channels. The spikes are seen to be an effect of the MAPMTs in the upper and lower rows and have nothing to do with the detector geometry or physics processes. The rates in Figure 7.6a are therefore not useful to estimate the correct template input. Because of the low statistics and the unavoidable bias in Figure 7.6b, it was decided to use these rates only for a systematic uncertainty and use the flat profile and 100 %

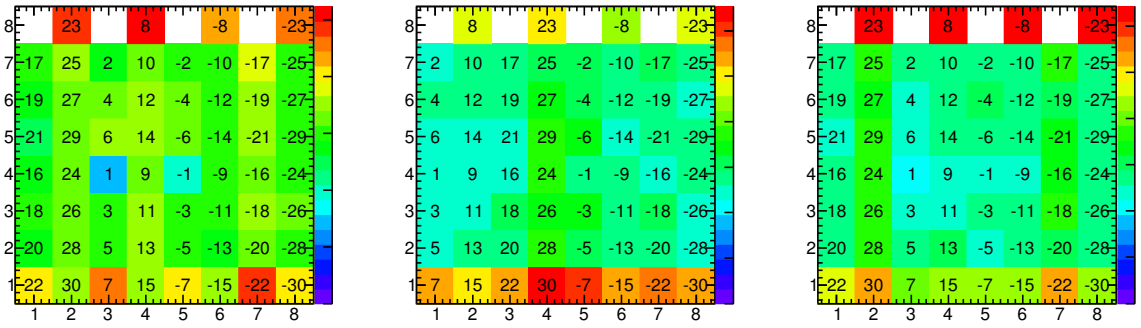

Figure 7.7: MAPMT channel rates for detector A7R1U+ normalized to the number of events in the OD layer. The number refers to the fiber number, where (−) means a fiber in the OD in the negative side.

efficiency as the nominal. The difference in distance is taken as a one standard deviation systematic uncertainty.

Vertical angular distribution

The fundamental assumption in the distance procedure is that the rate of a given track scales with the size of the overlap between the tracklets. This is only valid when the particles have no vertical angle. It is clear from Figure 7.1 that the probability for that track is enhanced if the particle has a downgoing trajectory. Due to the 4 cm distance in the z-direction between the upper and lower OD, a vertical angle can have a significant effect on the rates of the tracks. However, any vertical angular model can be implemented in the construction of the templates, and the angular profile is then found by profiling over the parameters of the model.

A tool has been developed to provide a visualization of the result of the template fit since Figure 7.2 is not very intuitive and it is non-trivial to judge the goodness-of-fit. The visualization tool is based on the assumption that the probability distribution for the true particle trajectory is flat inside the tracklet fiber overlap. The distance probability distribution for a single track is therefore the convolution of a flat distribution in the lower OD - whose range is given by the tracklet size - and a similar flat distribution in the upper OD. Using this information, an averaged probability over tracks as a function of distance is made, and for convenience it is normalized such that the peak in data has a value of 1. Since a single track therefore spans over many distances, there are complicated correlations between the different distances, hence the error bars can only be used to guide the eye and should not be used for any calculations.

In Figure 7.8, the visualization tool has been used to compare the data with the template fit for three different angular distributions. The template with no vertical angles does not describe the tails, Figure 7.8a. The angular profile of the beam core is expected to be approximately Gaussian with zero mean, but from the poor template fit in Figure 7.8b one can conclude that this is not the case for the beam halo hitting the ODs. The double Gaussian angular profile with zero means keeps a Gaussian distribution

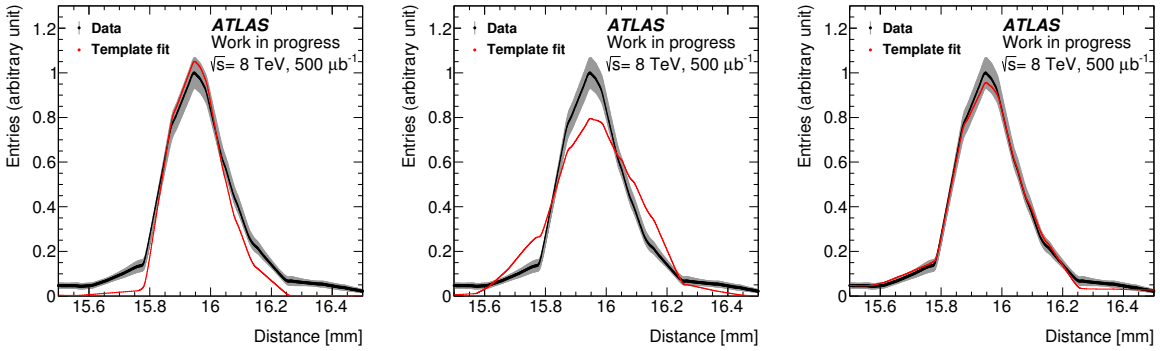

(a) No angles **(b)** Gaussian **(c)** Double Gaussian

Figure 7.8: Visualization of the fit result overlayed on the data from detector B7L1− for three different types of vertical angular distributions. Only a region around the distance peak is shown. Details on the visualization are decribed in the text. For convenience the distributions are normalized such that the peak in data has a value of 1.

in the core while the tails are described by a wider Gaussian, and this gives an adequate description of the data. The template fit is profiling over the widths and normalizations of the double Gaussian, hence the uncertainty due to the vertical angle is contained in the likelihood function, and the statistical uncertainty and the vertical angle uncertainty are therefore convoluted.

Horizontal angular distribution

The effect of a horizontal angular distribution is considered to be negligible, and no horizontal angles are used in the templates.

7.1.4 Incomplete template description

The templates do not give a perfect description of the data. The input parameters are only approximate, and things such as interactions with the detector material are completely ignored since no detector simulation for the ODs has been validated. The incomplete description results in different distance outcomes for different selection criteria. With a complete description of the data, the distance would be stable, hence the normal phrase of an 'uncertainty due to selection criteria' is actually more an uncertainty due to a poor description by the simulation. In this case it is necessary to vary the selection cuts and quote the difference in distance as a systematic uncertainty.

A data sample without the selection criteria number 3, 4, and 8 is chosen to find the systematic uncertainty. This is the most inclusive sample available, which is not dominated by background events. Figure 7.9 shows a zoom of the template fit for the standard sample along with the fit for the most inclusive sample. The incompleteness of the template fit is clearly visible in Figure 7.9b where there is a region to the left of the large signal peak which is not well described. The fit tries to describe the data with a large spread on the second Gaussian in the angular profile and it captures some

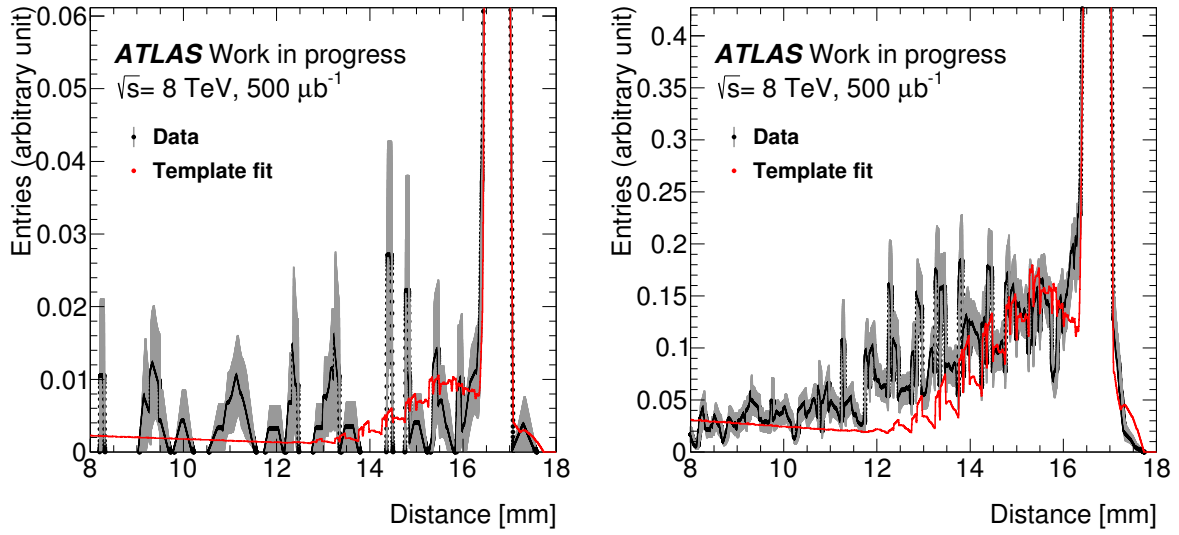

(a) Standard sample.

(b) Most inclusive sample.

Figure 7.9: Zoom of the visualization of the fit result overlayed on data from detector A7L1− for class 1 events for different selection criteria. Details on the visualization are described in the text.

of it. Due to this incomplete template description, the sample is useless for the distance measurement but serves well for the systematic uncertainty. The difference in distance between the two samples is taken as a one standard deviation systematic uncertainty.

The data has some very narrow spikes that come from hits in tracks with a small overlap between the tracklets. Such events are much more likely if the particles have vertical angles which make some of the effective overlaps larger. Uncorrelated tracklets do not show this feature, hence the spikes are unlikely to be background events. Therefore, more sophisticated shapes of the angular profile have been tried to give a better description of the data and thereby reduce the systematic uncertainty due to the selection criteria. Non-zero means in the double Gaussian, a Breit-Wigner shape, a completely flat distribution in angle, etc. were investigated, and improvements from the standard double Gaussian were possible. However, since the more complicated distributions did still not give an appropriate description, and the angular profiles seemed unphysical, it was decided in the ALFA community not to go further in this direction.

7.1.5 Stability of the distance procedure

It has been investigated whether the distance procedure itself gives rise to an uncertainty in the distance measurement. The distance was reconstructed in 100 pseudo-experiments with the same distance and signal-to-background ratio as in the data but with a 1000 times more events. All reconstructions yielded the same distance as the input within less than a micrometer. Therefore, it was concluded that the distance procedure does not add additional uncertainties to the distance.

Station	B7L1	A7L1	A7R1	B7R1
Distance	16073	16756	16638	15875
Uncertainties				
Statistical and vertical angular distribution	5	3	4	5
Selection	12	14	5	19
Vertical track distribution and efficiencies	4	4	3	4
Horizontal track distribution	3	2	3	1
MD-OD calibration	80	8	9	8
Combined uncertainty	81	17	12	22

Table 7.2: Distances and their uncertainties between the ALFA Main Detector edges for $\sqrt{s} = 8$ TeV , $\beta^* = 90$ m. All numbers are in micro meters.

7.1.6 Results

The results for the distance measurement is given in Table 7.2 along with the uncertainties. The distance for a station is found as the average of the two OD sides and the statistical uncertainties convoluted with the vertical angular distribution uncertainties are determined by error propagation. The difference in distance for the two OD sides is up to 200 μm due to unintended rotations in the $x - y$ plane of the detectors. The MD-OD calibration uncertainty was described in Section 6.3.1. The combined uncertainty is found by adding in quadrature, though only the statistical uncertainty is truly Gaussian.

7.1.7 Discussion

The precision of the distance measurement is slightly better than in Ref. [28] used in the elastic analysis in Ref. [32] despite the very small overlap between the upper and lower OD. A more precise measurement is expected if the distance is smaller:

Except for station B7L1, the dominating uncertainty comes from the selection uncertainty which is really an uncertainty due to the incomplete template description of the data. For station A7R1, the selection uncertainty is smaller than for the other stations. The reason is that the effects of selection are in opposite directions for A7R1+ and A7R1− and hence cancels out when averaging. It was discussed in Section 7.1.4 that further investigations of the vertical angular profile have the greatest importance if the distance uncertainties should be further reduced. The ODs were barely overlapping in this data set and edge effects can be the reason for the large effect. It is expected that the effect will be reduced for future running with smaller distances and thereby a larger overlap between the ODs.

The statistical uncertainty is not significant even though very tight selection criteria have been applied. This uncertainty will benefit from a smaller distance between the detectors where the overlap between the upper and lower OD is larger since this enhances the acceptance of signal events.

The effects of the horizontal and vertical track distributions are visible but not dominating the total uncertainty. With a smaller distance, the measurement will be less sensitive to the vertical profile and efficiencies since more fibers are used for the signal. Therefore, a few fibers with high or low rates will have a smaller effect.

For smaller distances, there is also an opportunity to reduce the MD-OD calibration uncertainty. The uncertainties on the positions of the individual OD fibers are 3-5 μm. The combined uncertainty on the MD-OD calibration is therefore overestimated by adding this number in quadrature (Section 6.3.1), since it corresponds to the case where all fibers are misplaced by the same amount and in the same direction. A more correct uncertainty for the combined effect of the fiber position uncertainties can be found using pseudo-experiments: For each experiment, the position of each fiber is taken randomly from a Gaussian with a width corresponding to the uncertainty for that fiber. The experiments are made with the same distance and signal-to-background ratio as in the data but with such high statistics that only the fiber uncertainty effect is present. The distance for the pseudo-experiments are plotted in a histogram. Taking the RMS for that distribution gives a more Gaussian-like uncertainty to be added in quadrature with the other MD-OD effects. It was decided by the ALFA community not to use this approach for this data set. The distances are so large that the number of overlapping fibers in the ODs is less than five and the RMS will be 2-3 μm, i.e. not a large improvement. However, for other runs with smaller distances between the upper and lower MD, the approach will be more useful since the RMS is seen to be as low as 0-1 μm. This is because many fibers contribute to the distance measurement.

7.2 High Voltage optimization for the OD MAPMTs

The data quality of the ODs can be optimized by adjusting the high voltage (HV) over the MAPMTs, since the HV determines the gain and thereby the signal-to-noise ratio for the OD fibers. A higher voltage reduces the probability of a particle passing through the OD without leaving hit fibers, but it also enhances the probability that events with good clean tracks will get more noisy. A lower voltage gives cleaner tracks, but some tracks will be lost.

7.2.1 Experimental setup

The effect of a HV change was investigated in the BBA run 267236. Once the detector stations B7R1 and A7R1 were in data taking position, data was recorded in station B7R1 for four periods of approximately 15 minutes each: The first was with the nominal HV of 900 V, the second was with a HV of 850 V, the third with a HV of 800 V, and the fourth again with a HV of 900 V to test that other conditions did not change during the run. It was decided not to try a HV above 900 V, as experience with the categorization of events in Section 7.1.2 showed that noise is a larger problem than missing tracks.

7.2.2 Selection criteria

The HV investigation is made on three event samples using different selection criteria in order to make sure that the potential benefit of changing the HV is not only a feature of very specific selection cuts:

Distance cuts: The selection criteria for this sample is chosen to resemble the ones used for the distance measurement as much as possible. However, in order to have enough statistics for the HV investigation with only about 15 minutes of data taking for each setting, only a subset of the cuts in Section 7.1.2 have been applied. The mandatory trigger coincidence between the upper and lower OD is kept. Furthermore, each OD must have at least one layer with only one fiber hit, and the tracklets in each OD must be isolated (none of the neighboring six fibers to the track must be hit).

Standard track cuts: It follows the logic of the track reconstruction in the MDs described in Section 6.2.1 and is much looser than the cuts used for the distance analysis. An overlap of fibers in all three layers are required, and the overlap must not exceed 480 μm which corresponds to the width of the active part of a fiber. Only single tracklet events are considered.

Restricted standard track cuts: In addition to the standard track cuts, at least one layer in both the upper and lower OD must be clean, i.e. have exactly one fiber hit.

7.2.3 Results

Figure 7.10 shows the signal peak with the *distance cuts* for the four different HV scenarios using the visualization method described in Section 7.1.3. Each signal peak has been normalized with the number of trigger coincidences between the upper and lower OD in that period, and it is seen that a HV of 800 V gives the largest signal per trigger coincidence. The strengths of the signals for the four different HV settings are given in Table 7.3 for all three kinds of selection criteria, where the signal is defined as tracks in the distance range $[5.5 \text{ mm}; 7.0 \text{ mm}]$.

The signal strength is largest with a HV at 800 V. It is not an effect of a change in other conditions during the data taking since - for all three selection cuts - the two periods with a HV at 900 V give the same signal strength. The 800 V does not give a significantly larger signal than 850 V for the data with the distance cuts due to the large statistical uncertainties, but the effect is clear for the two other track cuts.

The change in HV does not change the shape of the signal but only the statistics available for the distance measurement. This can be observed in Figure 7.11 where the signal peaks are normalized to the same height, and the shapes of the peaks are very similar. The HV will therefore not give a systematic uncertainty to the distance measurement but only change the available statistics.

Table 7.4 shows that also the signal-to-noise ratio is independent of the change in HV within the uncertainties. As for Table 7.3, all events within the distance range $[5.5 \text{ mm}; 7.0 \text{ mm}]$ is considered as signal and the rest as background.

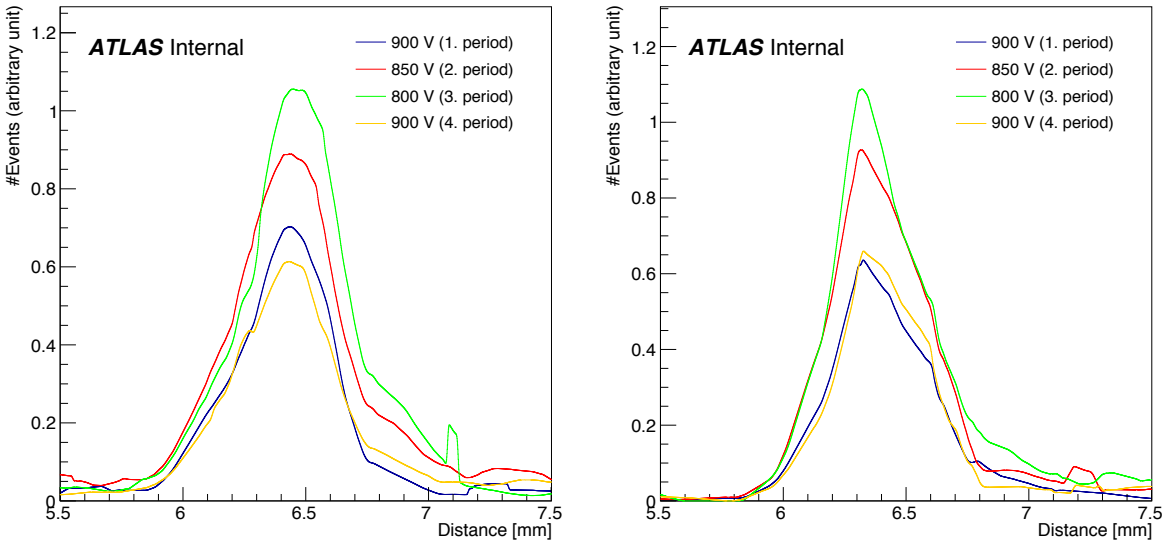

(a) B7R1+ **(b)** B7R1-

Figure 7.10: Signal strength per OD trigger coincidence using distance cuts in ALFA station B7R1 for four settings of the OD MAPMT high voltage in run 267236. Statistical uncertainties are not shown.

		Distance cuts	Standard track cuts	Restricted standard track cuts
900 V	left	3.4 ± 0.3	47.1 ± 1.1	6.7 ± 0.4
	right	3.0 ± 0.3	50.5 ± 1.1	6.3 ± 0.4
850 V	left	5.0 ± 0.4	65.7 ± 1.5	9.9 ± 0.6
	right	4.4 ± 0.4	73.0 ± 1.5	8.4 ± 0.5
800 V	left	5.6 ± 0.5	75.3 ± 1.9	12.5 ± 0.8
	right	4.9 ± 0.5	90.0 ± 2.0	10.0 ± 0.7
900 V	left	3.2 ± 0.3	47.8 ± 1.2	6.9 ± 0.4
	right	3.0 ± 0.3	51.6 ± 1.2	6.4 ± 0.4

Table 7.3: Number of signal events per 10000 trigger coincidences for four settings of the OD MAPMT high voltage in run 267236. Three different track criteria are compared. The uncertainties are only statistical.

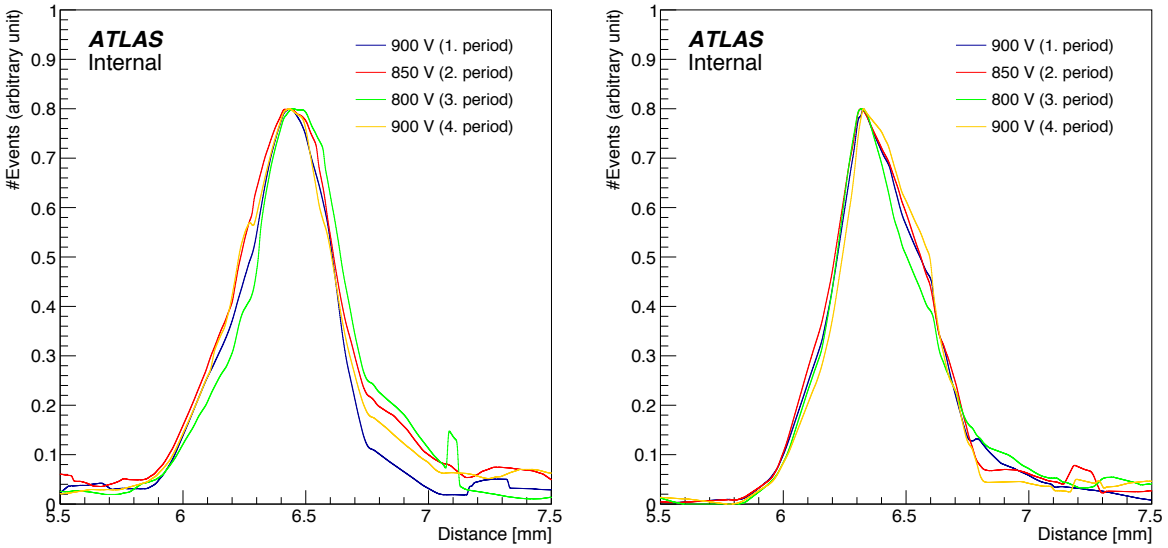

(a) B7R1+ **(b)** B7R1-

Figure 7.11: Signal shape with distance cuts in ALFA station B7R1 for four settings of the OD MAPMT high voltage in run 267236. All peaks are normalized to the same height. Statistical uncertainties are not shown.

		Distance cuts	Standard track cuts	Restricted standard track cuts
900 V	left	1.7 ± 0.2	0.217 ± 0.006	1.4 ± 0.1
	right	2.2 ± 0.4	0.315 ± 0.008	1.5 ± 0.1
850 V	left	1.4 ± 0.2	0.221 ± 0.006	1.3 ± 0.1
	right	2.0 ± 0.3	0.314 ± 0.007	1.3 ± 0.1
800 V	left	1.6 ± 0.2	0.222 ± 0.006	1.5 ± 0.1
	right	1.7 ± 0.3	0.308 ± 0.008	1.3 ± 0.1
900 V	left	1.7 ± 0.3	0.220 ± 0.006	1.3 ± 0.1
	right	2.1 ± 0.4	0.315 ± 0.008	1.4 ± 0.1

Table 7.4: Signal-to-noise ratio for four settings of the OD MAPMT high voltage in run 267236. Three different track criteria are compared. The uncertainties are only statistical.

7.2.4 Conclusion

Based on the results of this test, all HV on the OD MAMPTs are changed to 800 V. The HV test shows a clear benefit in the signal strength for B7R1 if the voltage is changed to 800 V, and neither the shape of the signal nor the signal-to-noise ratio is affected by this change. It is reasonable to assume that B7L1 will benefit similarly from a HV change as the A-side and C-side are identical. A part of the events in the outer stations comes from interactions in the inner stations, hence it is not given that the inner stations will show the same behavior under a change of the HV. However, the effect in B7R1 is large and the fiber multiplicity distribution in the inner stations are similar to the outer stations, hence a benefit in also the inner stations is highly expected.

7.3 Online distance histograms

Online histograms filled continuously during data taking are heavily used in ALFA. Only about eight hours per year are dedicated to elastic ALFA physics, hence it is crucial to monitor the data quality on-the-fly and change settings if needed. This section describes the implementation of online distance histograms which serves as a check that the quality of the data recorded with the ODs can be used for an offline distance measurement.

7.3.1 Selection criteria

The selection of events must be loose enough to fill the distance histograms at a rate such that poor data quality can be quickly identified and reacted upon, but also strict enough to get a clear signal over background. Since the precision of the distance is not needed to be better than 100 μm, the following cuts are sufficient:

1) Trigger coincidence between the upper and lower OD to ensure that particles are inside the area where the OD fibers are horizontal.

2) An overlap of fibers in all three layers are required for a track and the overlap must not exceed 480 μm. Neighboring fiber hits are allowed.

3) At least one layer in both ODs must have only one fiber hit in order to reduce the noise level.

7.3.2 Implementation

The processing of online histograms are made on the ATLAS HLT trigger farm, but an actual track reconstruction algorithm is still too slow. Therefore, a look-up table has been prepared for the OD tracks where all possible combinations of fiber hits giving a track are listed together with the positions of the tracklets. The positions of the tracklets were calculated with the actual fiber positions in the 16 ODs and given wrt. the MD edge.

Given a tracklet position in both the upper and lower OD, a histogram is filled with $d = D - d_{\text{up}} - d_{\text{low}}$ from Figure 6.4, i.e. the single track estimate of the distance between

the MDs in the station. The resolution of the track, is not taken into account and hence will produce a slight bias in the average distance as discussed in Section 7.1. However, it is well below the 100 μm precision which is the aim of the online distance measurement.

7.3.3 Results from run 281712

The first use of the online distance histograms was in the elastic run 281712 on October 13, 2015, with $\sqrt{s} = 13$ TeV, $\beta^* = 90$ m. The histograms after a couple of hours of data taking are shown in Figure 7.12. Clear spikes are visible for both sides in all four stations which show that the data quality is high enough to do a more precise offline distance measurement in the actual data analysis.

7.3.4 Concluding remarks

The importance of good OD data can hardly be underestimated. As discussed in Section 7.1, the number of overlapping fibers were only about three in Ref. [11]. If no fibers were overlapping or if the ODs were not working properly, the offline distance measurement would be impossible and hence also the correct translation from detector to beam coordinate system of the MD tracks. In the past, the quality of the OD data was only investigated in the offline analysis. With these new online distance histograms, it is possible to realize OD problems (or non-overlapping ODs) in less than 30 minutes - fast enough to change settings and ensure good data taking for the offline analysis.

7.4 Trigger efficiency

The efficiency of the ALFA MD trigger system is an important calibration factor in the determination of the elastic cross section since it is based on event counts. The author had the responsibility for the trigger efficiency determination in Ref. [11] and also in the data analysis presented in Part III in this thesis. This section describes the procedure used in both data sets to find the trigger efficiency for elastic events. All results shown here are for the data used in Ref. [11]. More details about the trigger efficiency is presented in an internal ATLAS note, Ref. [33].

The trigger efficiency is defined as the probability to have an elastic trigger signal for an elastic event. It can be found using elastic events selected with a trigger R which is unrelated to elastic events:

$$P(T|ER) = \frac{P(TER)}{P(ER)} = \frac{P(TE) \cdot P(R)}{P(E) \cdot P(R)} = P(T|E) \ , \tag{7.2}$$

where T stands for elastic trigger and E for an elastic event inside the detector acceptance.

The starting point of the trigger efficiency determination is to define the selection criteria for the elastic events. Then it will be shown that the probability to store an elastic event in the calibration stream is 100 % which allows to include data from the entire calibration stream in the efficiency study and not only events selected with the R trigger. Thereby, a smaller statistical uncertainty is obtained than using Equation (7.2).

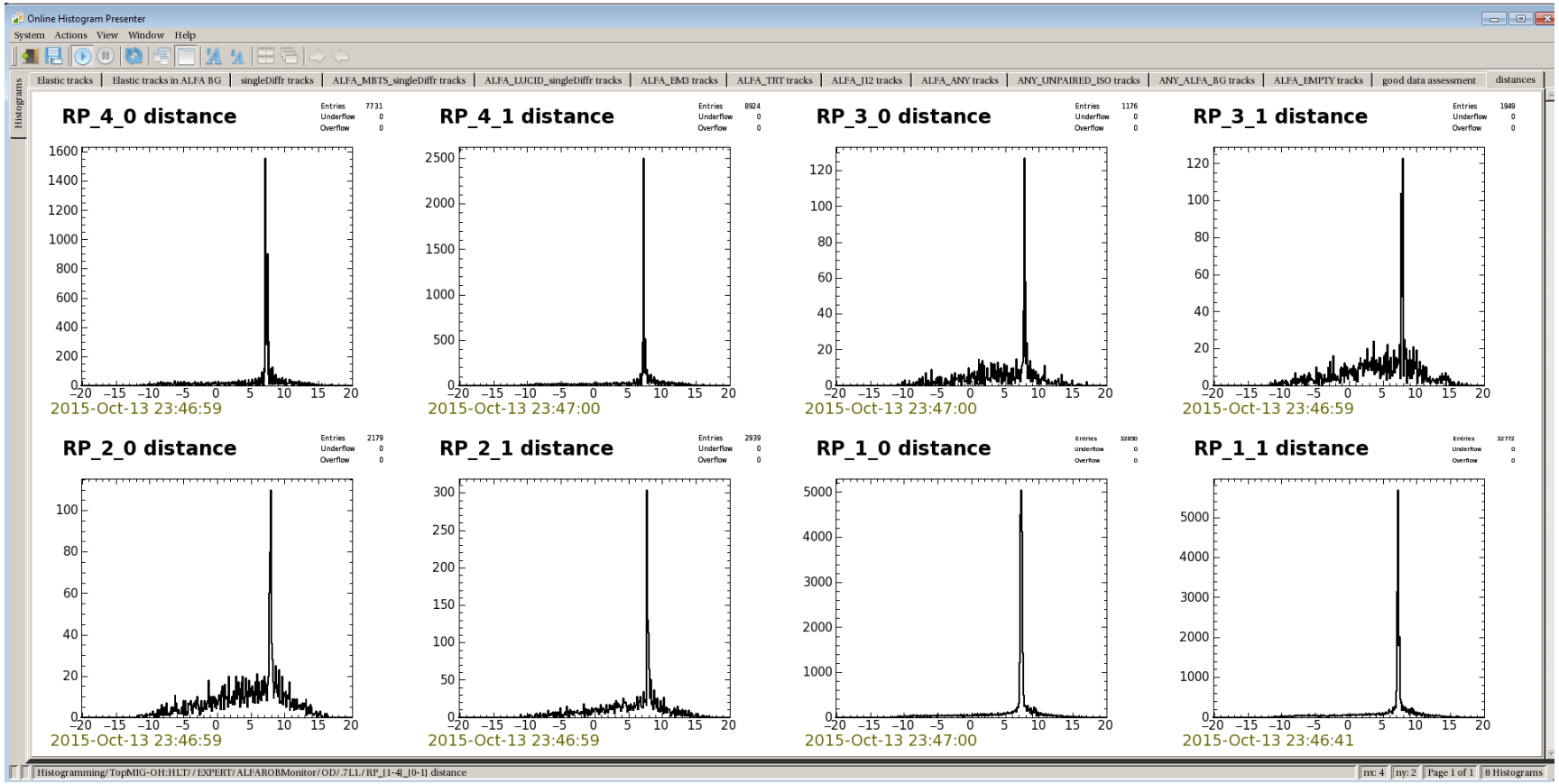

Figure 7.12: Screen shot of online distance histograms for ATLAS run 281712. The first number in the histogram title refers to the station number, where 1 is B7L1, 2 is A7L1, 3 is A7R1 and 4 is B7R1. The second number refers to the OD side where 0 is the positive side and 1 is the negative side.

7.4.1 Event selection

The determination of the elastic trigger efficiency is based on elastic events in the ALFA calibration stream. The same selection criteria as in the elastic physics analysis is used except for the elastic trigger requirement. A description of the different types of selection criteria can be found in Ref. [11]. An additional veto on events with more than one track in any of the four detectors in the elastic arm is used since it is impossible to determine which track fired the trigger. No background subtraction is used but the effect of background will be estimated and included as a systematic uncertainty.

7.4.2 Elastics in the calibration stream

The bunch group trigger, which takes the role as a random trigger when the bunch configuration allows for collisions, is used to find the probability of storing an elastic event in the calibration stream. An elastic event is saved in the ALFA calibration stream due to the L1_ALFA_ANY trigger item if any of the four detectors in the elastic arm sends a trigger signal to the CTP. If all detectors fail, the event will not be saved in the ALFA calibration stream unless another signal unrelated to the elastic event is sent to the CTP. Since the bunch group trigger saves random events, it will also contain elastic events even if all four detectors fail to send a trigger signal, i.e. it can play the role as the R trigger in Equation (7.2).

Figure 7.13 shows that the probability for missing an elastic event in the ALFA calibration stream due to failed trigger signals in all of the four detectors is $(1.2 \pm 0.8) \cdot 10^{-5}$ for elastic arm 1 (Arm 1368 in the figure) and $(7 \pm 7) \cdot 10^{-6}$ for elastic arm 2 (Arm 2457 in the figure) when selecting events with the bunch group trigger. The bunch group trigger is prescaled, hence the failing rate is found with only a subset of the data, but since the bunch group trigger takes random events, the obtained failing rate applies for the entire calibration stream.

7.4.3 Efficiency of the elastic CTP items

As mentioned in Section 6.5, one generally requires a trigger signal in more than one detector to save an event in the physics stream. Otherwise, the background level and therefore the trigger rates would be too high. The trigger efficiency for a specific CTP item is defined as:

$$\varepsilon_{\text{CTP item}} = \frac{\#\text{elastic events fulfilling the trigger logic}}{\#\text{elastic events}} \, . \tag{7.3}$$

It was shown above that

$$P(C|E) \simeq 1 \Rightarrow P(CE) = P(E) \, , \tag{7.4}$$

where $P(C)$ is the probability to save an event in the calibration stream. We therefore have

$$P(T|EC) = \frac{P(TEC)}{P(EC)} \simeq \frac{P(TE)}{P(E)} = P(T|E) \, , \tag{7.5}$$

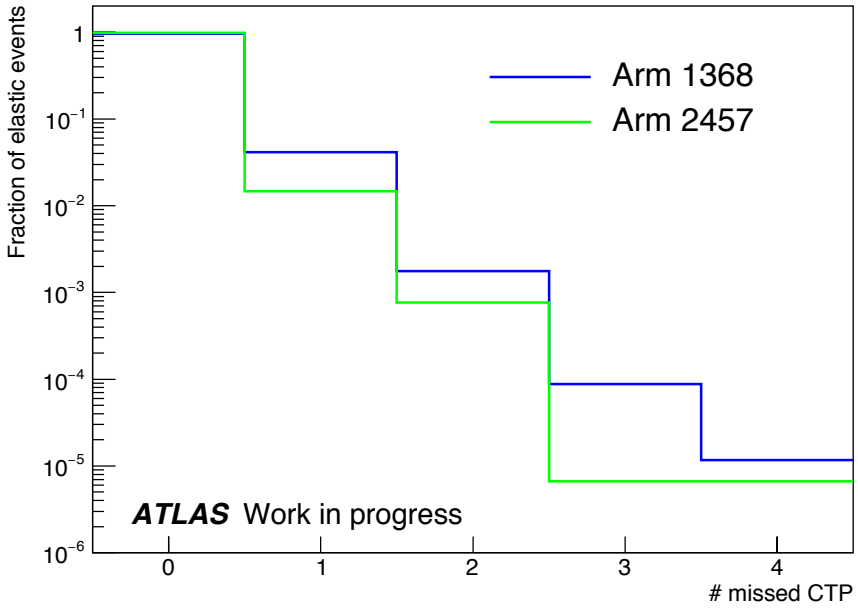

Figure 7.13: Normalized distribution of the number of detectors with a missing CTP signal for elastic events selected with the bunch group trigger.

hence Equation (7.3) can be written as

$$\varepsilon_{\text{CTP item}} = \frac{\#\text{elastic events in the calib. stream fulfilling the trigger logic}}{\#\text{elastic events in the calib. stream}} \,. \tag{7.6}$$

The efficiencies for the elastic CTP items along with statistical and systematic uncertainties are shown in Table 7.5. The systematic uncertainty is taken as the difference in efficiency for a sample where no selection cuts are used except for a track in all four detectors, i.e. no background events are rejected. The results for the items L1_ALFA_ELAST15 and L1_ALFA_ELAST18 are highlighted as those items are used for the actual event read-out. They benefit from a looser logic and hence have higher efficiencies.

It is important to investigate whether there is a geometrical dependence on the trigger efficiency, as the trigger efficiency would then not only contribute to the normalization of the differential elastic cross section but also the shape. Figure 7.14 shows that there is no geometrical dependence on the trigger efficiency in detector B7L1U. The track distribution for all elastic events is compared with the distribution for those elastic events without a CTP signal and no significant deviation is observed. Detector B7L1U has been chosen for this study since it is the detector with the highest failure rate. For the other detectors, the statistics on failed events is so low that nothing can be concluded.

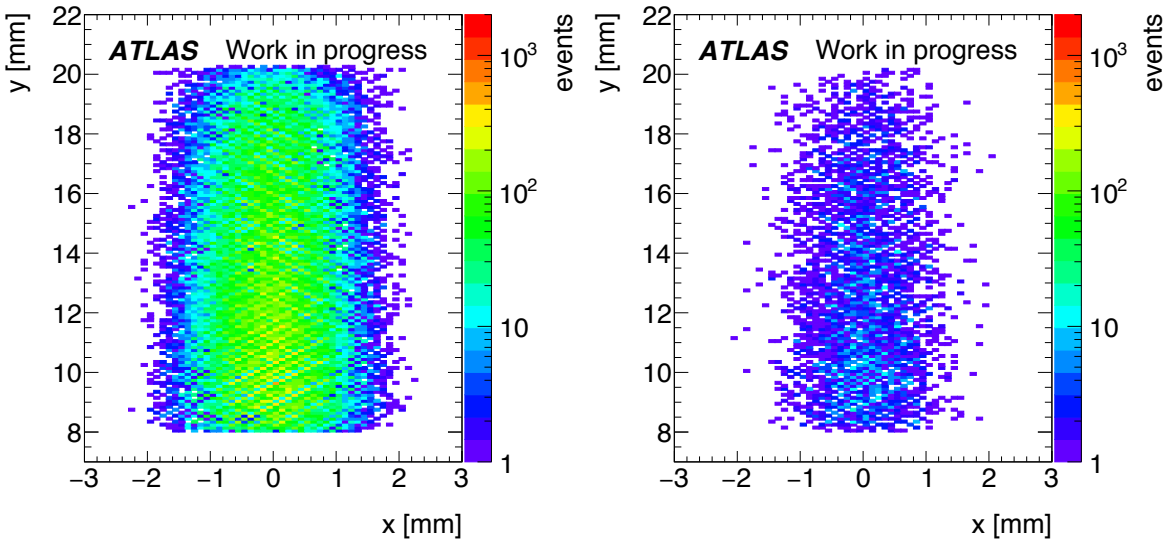

(a) Correct CTP.

(b) Wrong CTP.

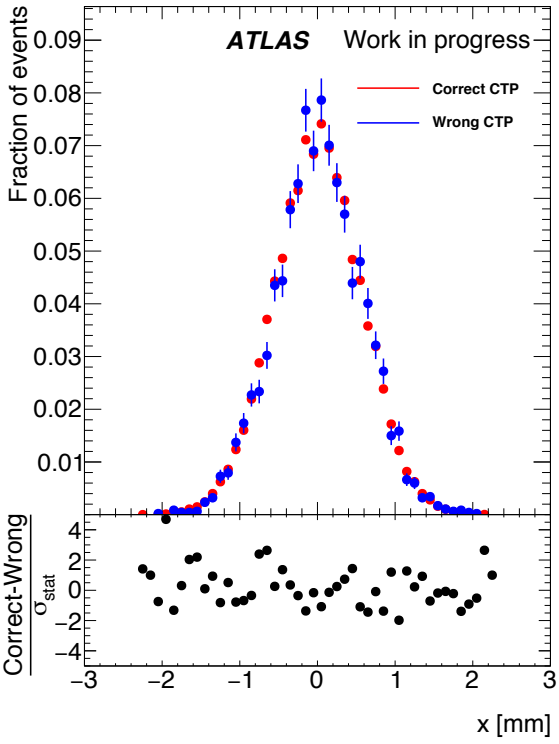

(c) Projection along x-axis.

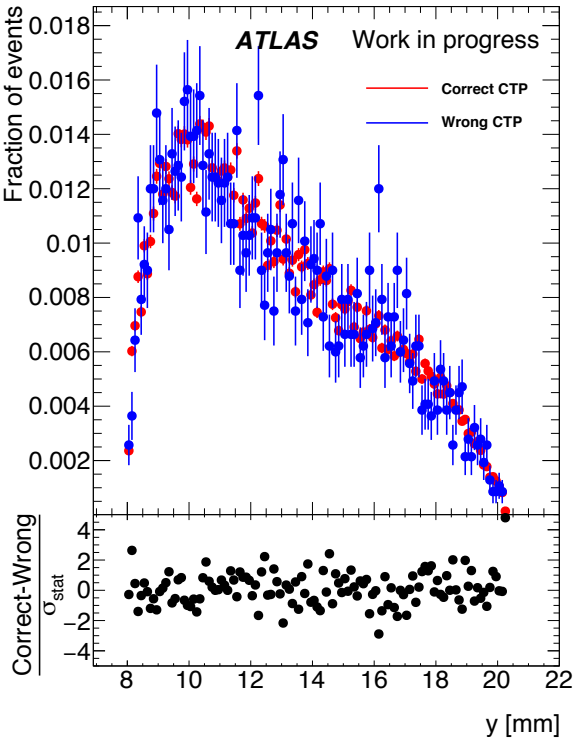

(d) Projection along y-axis.

Figure 7.14: Upper plots show the track distribution for elastic events. Lower plots show the normalized projected distribution of tracks. All plots are for detector B7L1U.

	Trigger logic	Efficiency ± stat. ± syst.
$\varepsilon_{\text{L1\_ALFA\_ELAST11}}$	B7L1U AND A7L1U AND A7R1L AND B7R1L	$95.75 \pm 0.02 \pm 0.06$
$\varepsilon_{\text{L1\_ALFA\_ELAST12}}$	B7L1L AND A7L1L AND A7R1U AND B7R1U	$98.48 \pm 0.01 \pm 0.01$
$\varepsilon_{\text{L1\_ALFA\_ELAST13}}$	(B7L1U OR A7L1U) AND A7R1L AND B7R1L	$98.56 \pm 0.01 \pm 0.01$
$\varepsilon_{\text{L1\_ALFA\_ELAST14}}$	B7L1U AND A7L1U AND (A7R1L OR B7R1L)	$97.00 \pm 0.02 \pm 0.05$
$\varepsilon_{\text{L1\_ALFA\_ELAST15}}$	**(B7L1U OR A7L1U) AND (A7R1L OR B7R1L)**	$\mathbf{99.887 \pm 0.003 \pm 0.001}$
$\varepsilon_{\text{L1\_ALFA\_ELAST16}}$	(B7L1L OR A7L1L) AND A7R1U AND B7R1U	$99.178 \pm 0.009 \pm 0.002$
$\varepsilon_{\text{L1\_ALFA\_ELAST17}}$	B7L1L AND A7L1L AND (A7R1U OR B7R1U)	$99.221 \pm 0.008 \pm 0.002$
$\varepsilon_{\text{L1\_ALFA\_ELAST18}}$	**(B7L1L OR A7L1L) AND (A7R1U OR B7R1U)**	$\mathbf{99.936 \pm 0.002 \pm 0.001}$

Table 7.5: Efficiencies for the different elastic CTP items. All numbers are in percent.

7.4.4 Fraction of events in the physics stream

As mentioned in Section 6.5, the physics stream contains a more condensed subset of events with a larger fraction of elastic events. It should in principle contain the same amount of events fulfilling L1_ALFA_ELAST15/18 as the calibration stream, but in the past it was observed that this is not always the case [34]. Therefore, the number of events collected with L1_ALFA_ELAST15/18 in both the physics stream and the calibration stream is compared as a consistency check. Fortunately, they turn out to be identical and no correction is needed.

Part III

Data analysis

8 | Data taking

The elastic data analyzed in this thesis was collected at the LHC on the 24^{th} to 25^{th} October 2012. A total of 74.4 μb^{-1} pp collision data was taken with the aim to observe the CNI region in the differential elastic cross section. This chapter describes the configurations used to fulfill this goal. The figures in this chapter are from Ref. [26] where also more details can be found.

8.1 Optics

The optics plays a crucial role to reach the very low t-values as discussed in Section 4.4.3. The β^* value should be maximized, and therefore the LHC magnet settings around the ATLAS IP were adjusted to provide a dedicated optics with $\beta^* = 1$ km. The design values of the transport matrix elements are shown in Table 8.1. The M_{12}^y elements were maximized which give large absolute vertical positions of the scattered protons at the ALFA stations and thus enhance the acceptance for small scattering angles. Unfortunately, only small M_{12}^x's for the inner ALFA stations were possible due to constraints on the power cables for the LHC magnets. This limits the resolution of the horizontal scattering angle. For the outer ALFA stations, the M_{12}^x's were essentially zero, i.e. they provide no information about the horizontal scattering angle. The M_{11}^y elements were very small, which means that the optics featured the parallel-to-point optics in the vertical direction.

	M_{11}	M_{12}	M_{21}	M_{22}
x, 241 m, A-Side	−0.5060	−0.7319	0.006942	−1.966
x, 237 m, A-Side	−0.5348	7.415	0.006942	−1.966
x, 237 m, C-Side	−0.5379	7.721	0.006902	−1.958
x, 241 m, C-Side	−0.5092	−0.4039	0.006902	−1.958
y, 241 m, A-Side	−0.004844	315.7	−0.003147	−1.340
y, 237 m, A-Side	0.008197	321.2	−0.003147	−1.340
y, 237 m, C-Side	0.008209	321.4	−0.003144	−1.288
y, 241 m, C-Side	−0.004837	316.1	−0.003144	−1.288

Table 8.1: Design values for the LHC transport matrix elements around the ATLAS Interaction Point.

8.2 Bunch structure

A probe with $\sim 10^{10}$ protons and three bunches each with $\sim 10^{11}$ protons were injected in each beam. The probe and two of the bunches were colliding. The last bunch was non-colliding and could have been used for background studies, but unfortunately the emittance was different than for the colliding bunches hence the background information is limited. The low intensity of the bunches and the large β^*, which means that the transverse size of the beam is large at the IP, gave an average collision rate of $\mu \lesssim 0.01$. This means that the probability for two or more interactions in the same bunch crossing is negligible.

8.3 Emittance

The emittance was made as small as possible before the injection to the LHC. The emittance was measured by wire scans approximately half way through the run because it plays an important role in the determination of the resolution of t. Unfortunately, the horizontal emittance in beam 2 was growing during the transition from injection optics with $\beta^* = 11$ m to the final optics with $\beta^* = 1$ km. Not only does it limit the t-resolution, but is also enhanced the intensity drop during scraping described in the following.

8.4 Collimator setup

A special collimator setup was used for the data taking in order to significantly reduce the beam halo background. Many tests were planned to investigate the optimal collimator settings, but unfortunately LHC experienced some problems unrelated to ALFA. In the end it was decided to do the steps illustrated in Figure 8.1:

1: The beam was scraped down with the primary collimator to only 2 nominal sigmas. This produced a large shower from beam particles hitting the collimator.

2: After step 1, the beam was now only 2 nominal sigmas wide. The primary collimator was retracted half a sigma to minimize the probability of further shower development from interactions with the beam particles. The ALFA detectors were moved into data taking position which was half a sigma further from the beam than the primary collimator, i.e. at 3 nominal sigmas.

3: The beam halo started to repopulate which gave two kinds of background contributions: Actual beam halo particles hitting the ALFA detector and leaving a track, but also an increase in shower development from the collimator which lightened up too many ALFA fibers to be able to reconstruct a track from a possible elastic event.

4: When the background level had reached an unacceptable level, the primary collimator again scraped down the beam to 2 nominal sigmas which gave enormous

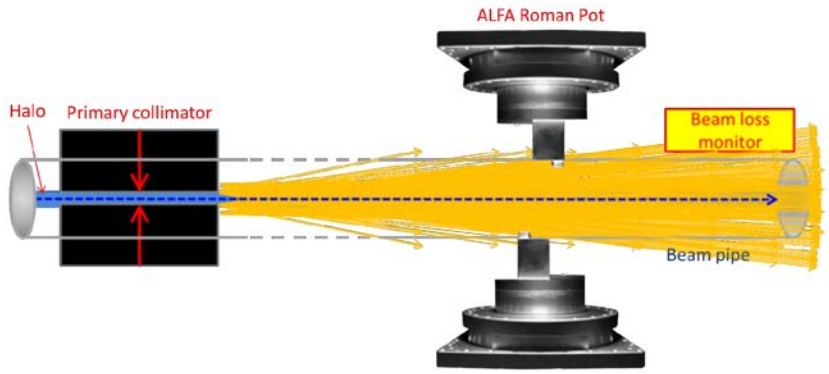

(a) Step 1: Primary collimator scrapes down the beam to 2 σ_{nominal}.

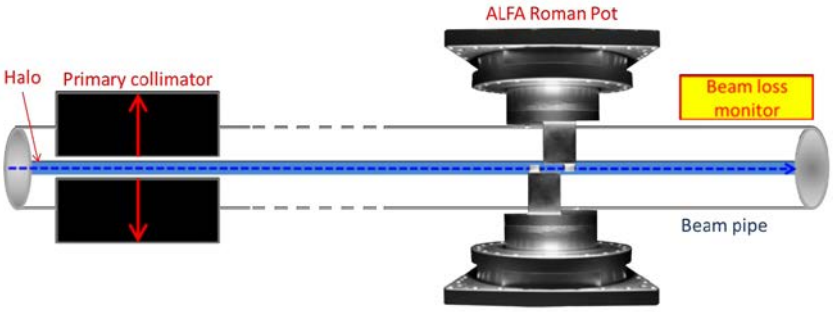

(b) Step 2: ALFA detectors in data taking position at 3 σ_{nominal} and primary collimator retracted to 2.5 σ_{nominal}.

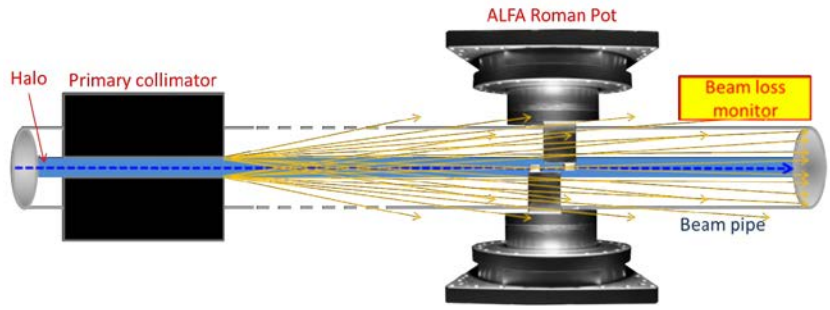

(c) Step 3: Beam halo increases and hits the primary collimators which sprays the ALFA detectors.

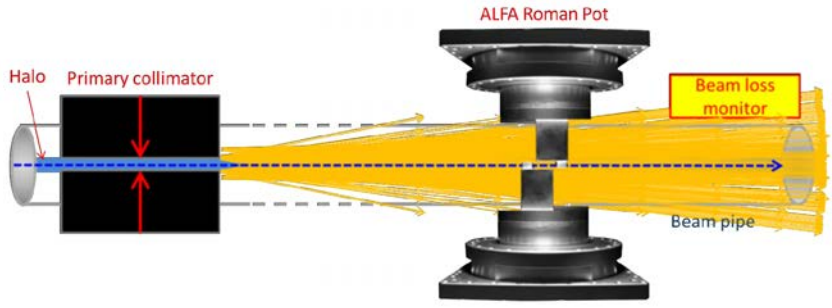

(d) Step 4: Primary collimator scrapes down the beam to 2 σ_{nominal} with ALFA in data taking position.

Figure 8.1: Illustration of the use of the primary collimator in ATLAS run 213268.

trigger rates in the ALFA detectors. Step 2 was now repeated and more data with a low background rate could be collected. The ALFA detectors were kept in data taking position during step 4 except the first time.

Step 2, 3, and 4 were repeated to give in total six periods of elastic data. The decision about when to repeat step 4 was based on a comparison between the elastic trigger rates (L1_ALFA_ELAST15/18) and the rates in the antigolden configurations (L1_ALFA_SYST11/12) where all four upper/lower detectors have been hit. The antigolden configuration is an approximate measure of the background rate in the elastic configuration and will be discussed later. Figure 8.2 shows these trigger rates as a function of time. The ratio between elastic and background trigger rates was high right after scraping where the background from the beam halo was at the minimum, but it approached a value of 1 after only about 30 minutes, meaning that background dominated the trigger rates in the two elastic arms. The rates were enormous during the scraping periods, and no useful elastic data could be recorded. The luminosity dropped during each scraping since parts of the two beams were removed, and in the end the luminosity was so low that it was decided to dump the beam.

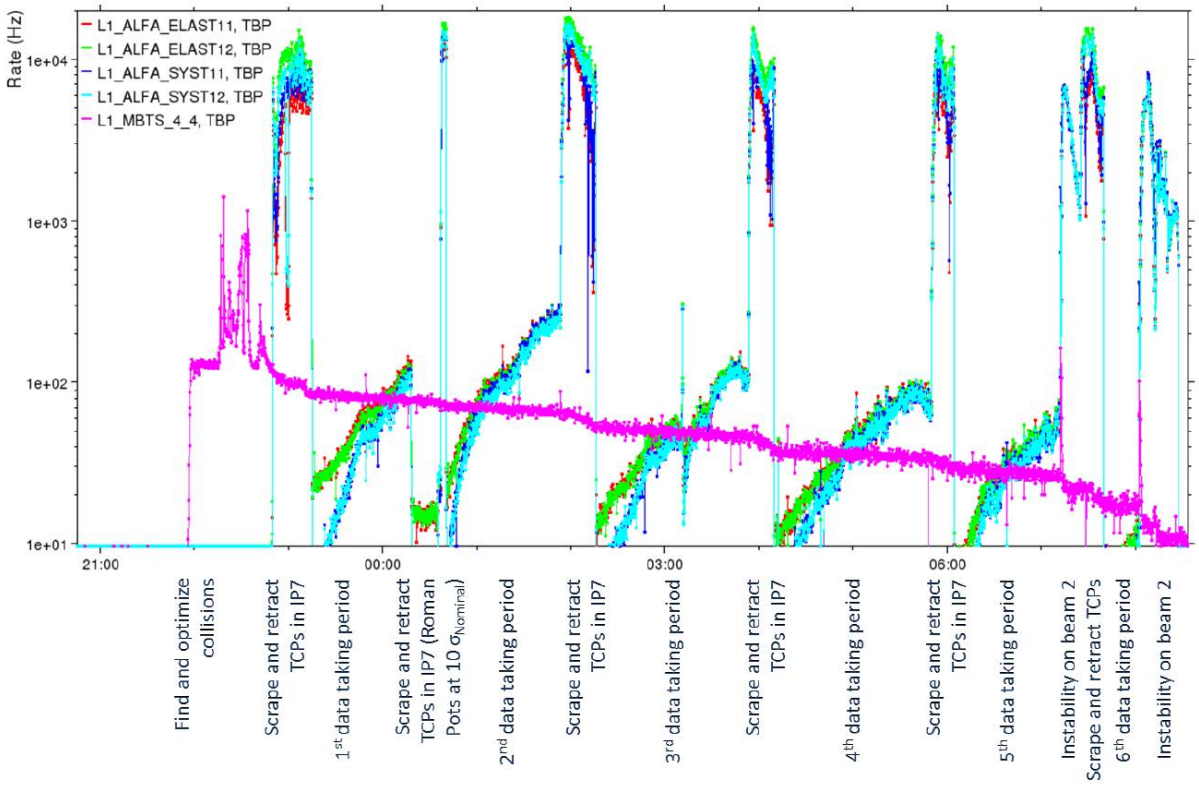

Figure 8.2: Rates for elastic (ELAST) and background (SYST) trigger signature. The L1_MBTS_4_4 rate scales to first order with the luminosity.

9 | Event selection

The only outcome of an elastic collision is two protons with opposite momentum where no energy has been lost to the surroundings. No particles will therefore be detected by ATLAS, but ALFA covers part of the phase-space for the two protons. Two categories of elastic events will be considered: In elastic arm 1 events, the proton on the A-side is scattered above the beam and gives a signal in the detectors B7L1U and A7L1U, and the proton on the C-side is scattered below the beam and is detected by A7R1L and B7R1L, see the green trajectories in Figure 9.1. The other category is elastic arm 2 (red trajectories) where the proton on the A-side is scattered below the beam and the proton on the C-side above, giving signals in B7L1L, A7L1L, A7R1U, and B7R1U.

The cut flow is shown in Table 9.1 and meaning of the cuts will be described in the following. The previous elastic ALFA analyses [11, 32] are used as inspiration[1], however this data set is more complex due to the special LHC setup described in the previous chapter, and new ideas have therefore been invented.

9.1 Trigger and data quality

The events are recorded online with the CTP items L1_ALFA_ELAST15 for arm 1 and L1_ALFA_ELAST18 for arm 2. These are the loosest possible elastic triggers which have low enough rates to be used unprescaled. Offline, the elastic events must have a trigger signal in all the four detectors in the relevant arm. The online trigger criterion was sufficient in the previous analyses, but in this data set the beam conditions are much harsher. Using the more strict offline trigger criterion, the number of upstream shower

[1]Further details about these analyses can be found in Ref. [35] which is an internal ATLAS note.

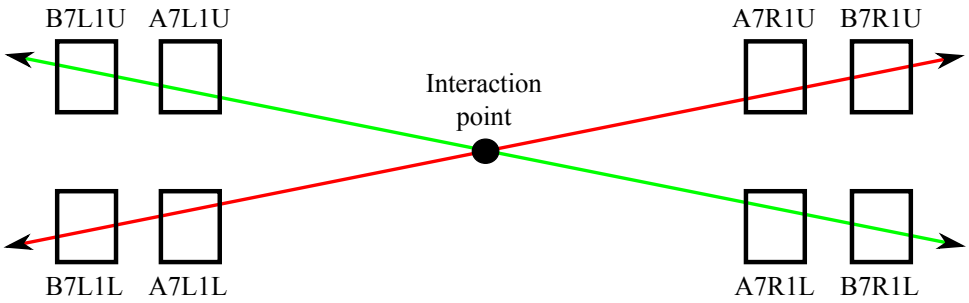

Figure 9.1: Illustration of the two elastic arms and the corresponding detectors that are hit.

	Number of events	
Selection criterion	Arm 1	Arm 2
Online trigger, LB, dead time	765326	1117989
Offline trigger	556052	731603
Tracks in all detectors	128038	156038
Edge cut	120529	125672
Beam screen cut	116848	122669
Cut on y_A vs. y_C	112824	117932
Cut on x vs. θ_x	107226	108071
Cut on x_A vs. x_C	104204	96101
Estimated background	781	3372
Total elastic candidates	103423	92729

Table 9.1: Number of events after each stage of the selection.

events is greatly reduced which simplifies a later analysis step.

As described in Chapter 8, the beams were scraped several times during the run by the LHC collimators in order to reduce the repopulating beam halo. Only luminosity blocks outside the scraping periods are used for the elastic analysis since the background is enormous during the scraping and ATLAS goes busy. Furthermore, only luminosity blocks with a dead time below 5 % and a duration above 55 seconds are used. Events from the two colliding bunches are used but not events from the probe since the luminosity is very low.

9.2 Track definition

The elastic analysis is based on the tracks of the protons. An event must have a reconstructed track in all four detectors to be considered for the elastic analysis. Otherwise, it will complicate later analysis steps.

The idea behind the tracking algorithm was discussed in Section 6.2.1, and Figure 9.2a shows a hitmap where the track criteria from the previous analyses have been used. The elastic signal is visible as the vertical band around $x \approx 0$. However, the most striking feature is the two bands at $\pm 45°$ which cannot be explained by any real proton tracks. They are fake tracks and need to be removed by the track criteria. These fake tracks are a consequence of the fiber layout in the MDs and the large amount of background at the detector edge: When two protons hit the detector, there are four possible track combinations (Section 6.2.1). If one proton hits around the detector edge at $(x, y) \approx (0, -135)$ mm and another one hits in the elastic band, the two fake tracks will be in exactly the bands at $\pm 45°$ with a y-coordinate given by the average of the two real tracks. The amount of these fake tracks increases with the background level at the detector edge and is therefore larger than in the previous analyses.

The procedure used in Ref. [32] was to look at the detectors with only one track, and based on that information select the best elastic track candidate for the detector(s) with

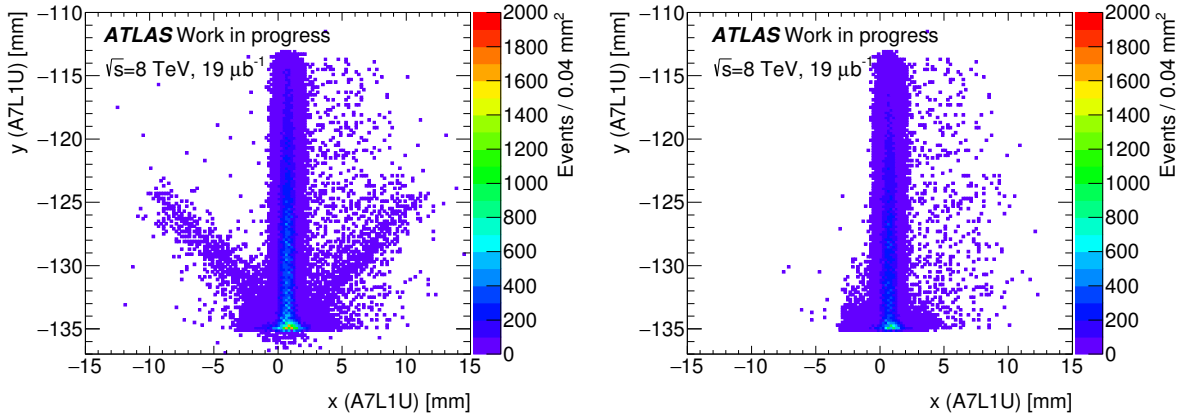

(a) Standard. **(b)** Final.

Figure 9.2: Hitmaps for different track criteria described in the text. The detector coordinate system is used where the MD edge is at $y \simeq -135$ mm.

multiple tracks. Such a procedure is difficult if the background proton is close to the elastic proton. There will be a risk of selecting either a fake track or the background track instead of the elastic track. Since the background events are primarily close to the detector edge, this effect will be greatest in the interesting CNI region at small scattering angles.

In Ref. [11] the best quality track in terms of the number of overlapping fibers in the U- and V-plane and the size of the overlap was chosen. These are the criteria used in Figure 9.2a. Clearly, this procedure is not useful in this analysis. There is a chance of selecting a completely wrong track, and the event will be rejected by the correlation criteria described later.

Instead of dealing with the multiple tracks, a safe procedure is chosen. If one or more detectors have multiple tracks, the entire event is rejected. This will naturally lower the efficiency for selecting an elastic event, but it simplifies the determination of the efficiency performed in a later analysis step.

Another kind of fake tracks comes from uncorrelated fiber hits which add up to a track by happenstance. The fiber hits can be cross-talk or noisy fibers. Both effects are more likely in this data set wrt. the previous analyses because the detector hit rate from the beam is much higher. A simple way to reduce such fake tracks is to require a high amount of overlapping fibers. The layer efficiency was measured in a test beam campaign to be around 90 % [36]. Figure 9.3 shows the probability to reject an elastic track for different criteria on the number of overlapping fibers in the U- and V-plane. Based on this plot, it was decided to increase the cut from three to six overlapping fibers.

Figure 9.2b shows the hitmap for the final track criteria. The number of events is lower, but the orthogonal bands are gone, and so are the fake tracks below the detector edge at $y \simeq -135$ mm. The elastic band is still clearly visible. The broad distribution of events close to the detector edge is background from the beam. The events on the positive x-side of the elastic band at all y-values are background events from diffractive processes.

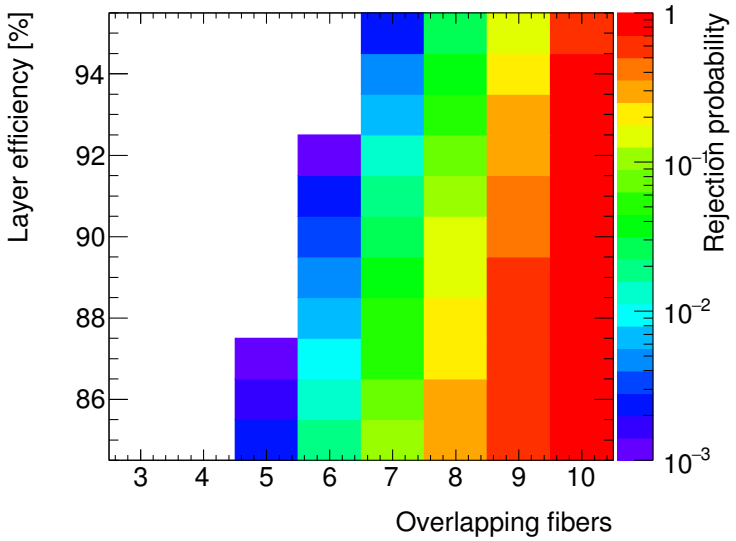

Figure 9.3: Probability to reject an elastic track as a function of the layer efficiency and the criterion on the minimum number of overlapping fibers. The probability is calculated from a binomial distribution. The white bins are underflow bins.

9.3 Edge cut

All events where a track in any of the detectors is less than 90 μm from the detector edge are rejected in order to ensure that the trigger tiles overlap with the MD tracking region. This will remove some of the interesting events at small scattering angles, but without the edge cut the trigger efficiency will unavoidable be position dependent which complicates the analysis. Furthermore, the cut ensures a full track detection for the events.

The value of the edge cut is the same as in Ref. [11], however the application is different. In Ref. [11] it was applied after the offline track based alignment of the detectors described in Section 10.6, whereas in this analysis the cut is applied in the detector coordinate system before alignment. The overlap of the MD tracking region with the trigger tiles will of course not depend on the alignment, and with this new procedure one can avoid to update the edge cut for each alignment update.

9.4 Beam screen cut

Figure 9.4 shows the y-distribution in the high y-range for all the eight detectors. For all detectors, there is a significant decrease at $y \sim -114$ mm caused by the LHC beam screen. Therefore, a beam screen cut must be applied to the data to remove this effect. For simplicity, the beam screen cut value is chosen as 1 mm from the kink in B7L1L, hence events where one of the tracks have a y-value above $y = -115.6$ mm are rejected. A slightly larger acceptance at large scattering angles could be obtained with individual detector beam screen cuts. Again, the cut is applied in the detector coordinate system with the same reasoning as for the edge cut.

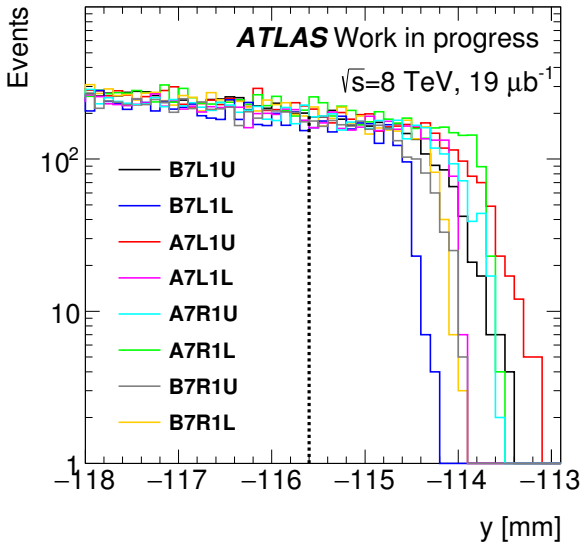

Figure 9.4: Zoom of the y-distributions at large distance to the beam for the eight detectors. The beam screen cut at $y = -115.6$ mm is shown as the dashed black vertical line.

9.5 Correlation cuts

The last type of elastic selection cuts is based on the correlations between the coordinates of the reconstructed tracks in the four detectors. The momentum conservation in elastic scattering provides strong bounds on the coordinates, which can be found from a simulation. The simulation needs input in terms of the detector resolution, beam properties and the optics, which is the subject of the next chapter.

Two of the most important correlations are shown in Figure 9.5 for simulated elastic events. The black lines and ellipse show the 3.5σ contour which will be used to select elastic events in the data. Figure 9.6 shows the same correlations for the data events. The value of 3.5σ is taken from the previous analyses. The plots show no need to change this value.

The correlations used to select elastic events are:

$$
\begin{aligned}
&y^A_{\text{inner}} - y^C_{\text{inner}} \ , \\
&y^A_{\text{outer}} - y^C_{\text{outer}} \ , \\
&x^A_{\text{inner}} - x^C_{\text{inner}} \ , \\
&x^A_{\text{outer}} - x^C_{\text{outer}} \ , \\
&x^A_{\text{inner}} - \theta^A_x \ , \\
&x^C_{\text{inner}} - \theta^C_x \ .
\end{aligned}
$$

The local horizontal angle at the ALFA stations, θ_x, is calculated as the difference between the x-coordinates in the inner and outer detectors divided by the distance. A bachelor project co-supervised by the author [37] searched for additional correlation plots to further reduce non-elastic events. However, it turned out that the gain was minimal.

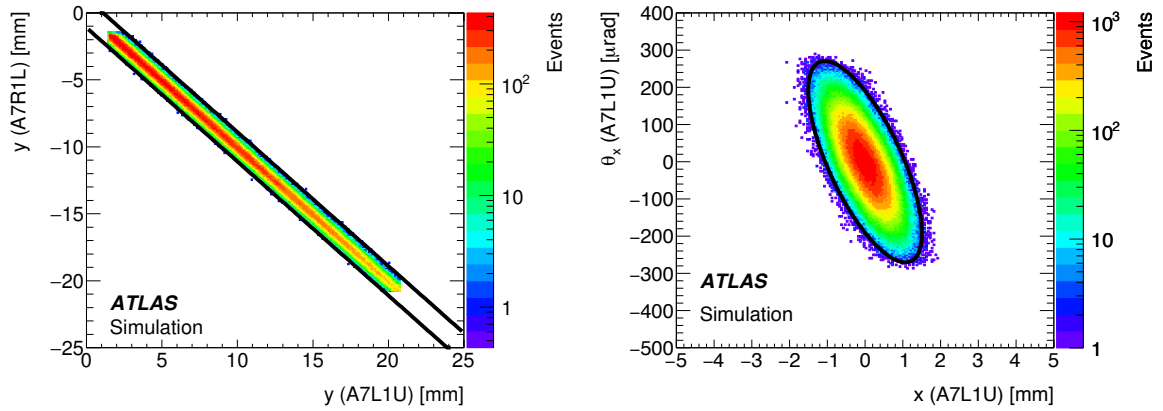

Figure 9.5: Position correlation plots for a simulation of elastic events. The black lines and ellipse show the 3.5σ contour.

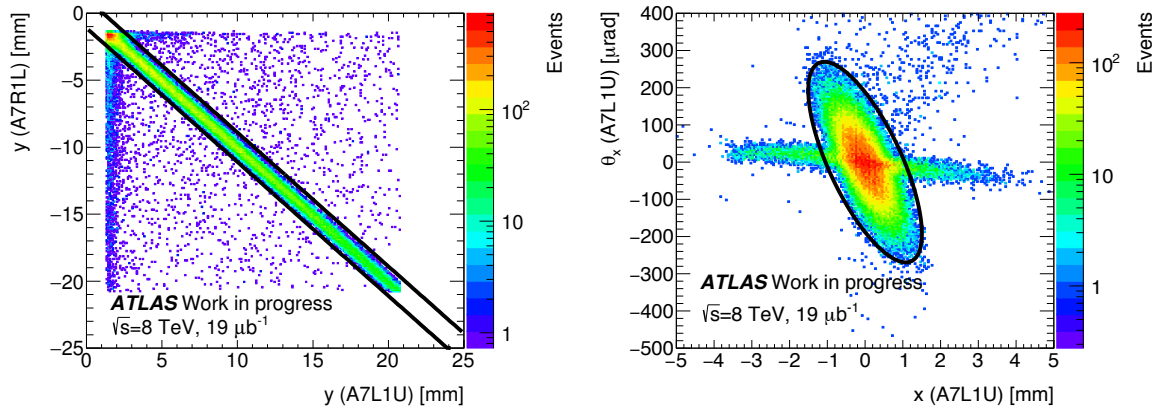

Figure 9.6: Position correlation plots for data events. The black lines and ellipse show the 3.5σ contour of elastic events determined from a simulation.

9.6 Background estimation

The background sources for an elastic event come from beam halo protons and single diffractive scattered (SD) protons in accidental coincidence as well as protons from double pomeron exchange (DPE). A fraction of these events fulfill all the elastic selection criteria and are hence impossible to completely remove from the elastic sample. Instead, the background level and shape need to be determined and subtracted from the sample of elastic candidates.

In the following, the *antigolden* background estimation method used in the previous ALFA analyses is discussed, and it will be argued that the method is not appropriate for this analysis. Therefore, a new background estimation method has been developed.

9.6.1 Background estimation from antigolden events

The antigolden background estimation uses events with tracks in all four upper or all four lower detectors. Such events contain all the three kinds of background sources. The y-coordinates in the two detectors on one side of the IP are flipped in sign to mimic hits in the opposite detectors, all the elastic event selection cuts are applied, and the four-momentum transfer, t, is calculated just like for elastic events described later. The resulting t-spectrum is then used as an estimate of the background.

The antigolden method is only valid when the upper and lower detectors have the same distance to the beam center. This is not the case in this data set as will be shown later. As an example, consider the case where the four detectors in elastic arm 1 are closer to the beam than the four detectors in elastic arm 2[2]. With such a setup, the antigolden events would never get as low in t as the elastic arm 1. Therefore, the estimated background shape at low t would be wrong which would destroy a study in the CNI region. Furthermore, the background level predicted by the antigolden method is not valid with an asymmetric detector setup. If the background falls rapidly with increasing distance to the beam, the background level in elastic arm 1 (elastic arm 2) would be greatly underestimated (overestimated) by either of the antigolden configurations, and the sum of events in the two antigolden configurations will in general not be similar to the sum of background events in the two elastic arms.

Furthermore, the antigolden method relies on the assumption of symmetric background in the upper and lower detectors. If the background level and/or shape is different in the upper and lower detectors, the antigolden method is not guaranteed to give a reliable background estimate. From simulation, it has previously been shown [11] that DPE events have a similar probability to be in the golden as in the antigolden topology and the same is assumed for SD+SD coincidence. However, this needs not to be the case for halo particles. Figure 9.7 shows a comparison of one of the correlation plots between the two elastic arms. It is clear that the distributions outside the elastic selection region are not the same in the two arms, i.e. the background is not symmetric and the antigolden method is doubtful as a good background estimator.

9.6.2 Background shape from accidental coincidence

Beam halo and SD protons can hit the ALFA detectors simultaneously in the A- and C-side in accidental coincidence which give three different contributions: halo+halo, SD+SD and halo+SD. Simulations exist for SD processes, whereas no reliable simulation of neither the level nor the shape of the beam halo exists. The non-colliding bunches offer an opportunity to estimate the halo background as there will be no contribution from physics processes. Unfortunately, the emittances of the non-colliding bunches were different than for the colliding bunches by up to a factor of 2 for unknown reasons, hence the halo shape cannot be directly translated to the colliding bunches. Therefore, the combined halo+halo, SD+SD and halo+SD background contribution (hereafter called RUC for Random Uncorrelated Coincidence) is estimated from the colliding bunches themselves.

[2]TOTEM used such a configuration for their $\beta^* = 1$ km data taking [2].

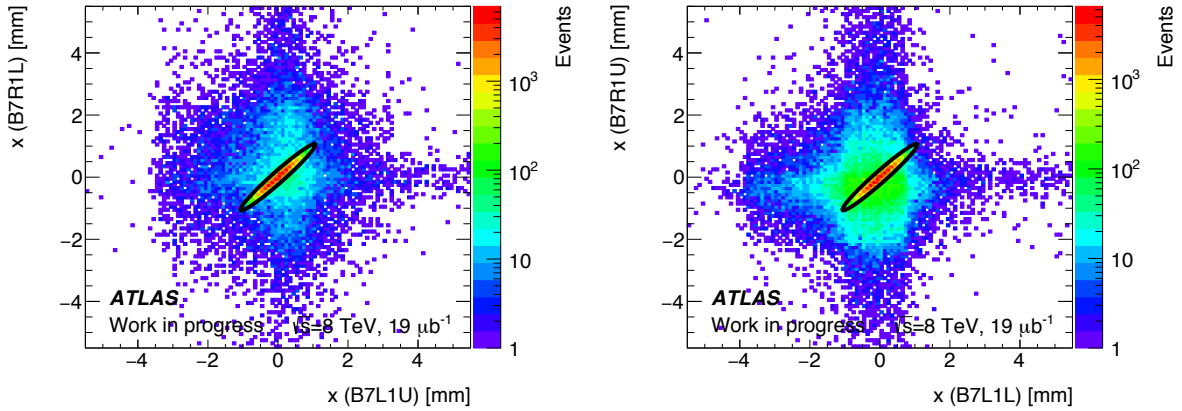

(a) Elastic arm 1. **(b)** Elastic arm 2.

Figure 9.7: Correlation between the outer x-coordinates in the two elastic arms. The black ellipses show the 3.5σ contour of elastic events determined from a simulation.

A combined background template for RUC in elastic arm 1 is constructed as follows:

1) Make a sample of events with tracks and triggers in the detectors B7L1U and A7L1U. Veto on triggers in A7R1L and B7R1L to remove elastic events. Require the trigger item L1_ALFA_ANY to have fired to avoid a trigger bias in the ratio between halo and SD protons.

2) Make a similar sample of events with tracks and triggers in the detectors B7R1L and A7R1L and with a veto on triggers in A7L1U and B7L1U. Require L1_ALFA_ANY to have fired.

3) Combine an event from the first sample with an event from the second sample.

4) Treat the combination as a single event and apply all the elastic selection criteria.

The background template for elastic arm 2 is constructed in a similar way using the other four detectors. The shape and the composition of halo+halo, SD+SD and halo+SD is the same as in the data, but the normalization is different and needs to be determined.

9.6.3 Background shape for DPE events

The distribution of DPE events is estimated from a Monte Carlo simulation by a collaborator using the MBR model in Pythia8 [38]. Both the shape and the level of DPE are not well determined by theory. Therefore, the level will be determined from the data as described in the following. Fortunately, the DPE background contribution turns out to be negligible, and hence also the specific choice of the theoretical model.

9.6.4 Background level

For both RUC and DPE, the background level is found with a side-band method using the same correlation plots as in the elastic event selection. A region O is chosen well

outside the elastic signal region and hence contains only background. The background template is then scaled such that the integral of events in O in the template matches the integral of events in O in the data. The scaled events in the background template inside the elastic selection now estimates the true background.

There are no events inside O in Figure 9.8a for DPE events, whereas there is a large amount in Figure 9.8b for RUC events. The events inside O in the data in Figure 9.8c therefore come only from halo/SD coincidence, hence the region is suitable for the RUC template scaling. Figure 9.8d shows another correlation plot for the RUC template after the scaling. There are basically no events inside the red triangles, however DPE events are likely to populate this region, Figure 9.8e. Therefore, the events inside the red triangles in Figure 9.8f must be dominated by DPE, and the red triangles are used to scale the DPE template.

9.6.5 Time and bunch dependence

The RUC template contains both halo and SD events which are of completely different nature: Whereas the SD level decreases with time due to the decreasing luminosity, the halo level increases with time after each scraping period because the beam halo repopulates. This means that the SD/halo ratio is time-dependent for both the data and the RUC template, but the dependences need not to be the same: Data contains true coincidences which are therefore described by products of probabilities at a certain time, whereas the coincidences in the template are artificial and in general events happening at different times are combined. The background estimation procedure is only valid if the SD/halo ratio is the same for the data and the background template, since SD and halo have different shapes. Therefore, the background estimation must be made time-dependent to catch this effect.

The beam properties also affect the SD/halo ratio. Since the beam properties can be different for each colliding bunch, the background estimation must be performed for each bunch separately in order to correctly account for this.

Three different cases will be used to investigate the influence of the time and bunch dependence:

1. **Split in LB and BCId:** Background templates are constructed for each luminosity block and bunch ID and scaled accordingly. This is an easy way to handle the time and bunch dependent halo/SD ratio.

2. **Combined LB and BCId:** The halo/SD time dependence and bunch differences are neglected by making a combined template for all luminosity blocks and bunches.

3. **Combined LB and BCId with MBTS veto:** The same as in case 2 but with an additional veto on a MBTS trigger signal in the template. Such a veto was used in the previous analyses to estimate the effect of a reduction in the SD background fraction and will here be used to change the halo/SD ratio.

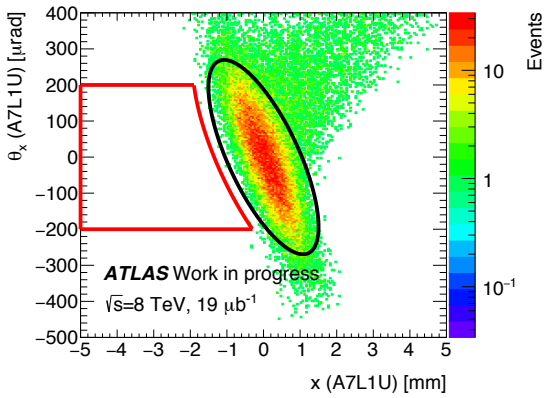

(a) DPE correlation with the RUC selection region.

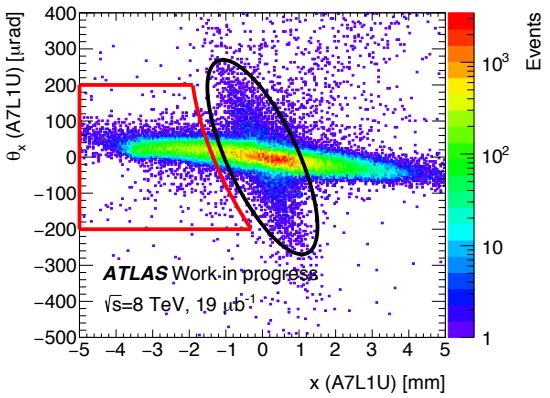

(b) RUC correlation with the RUC selection region.

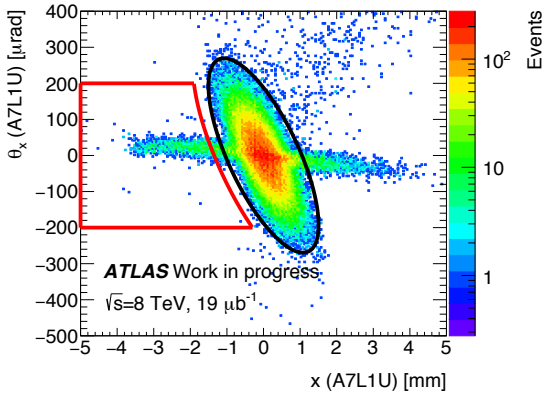

(c) Data correlation with the RUC selection region.

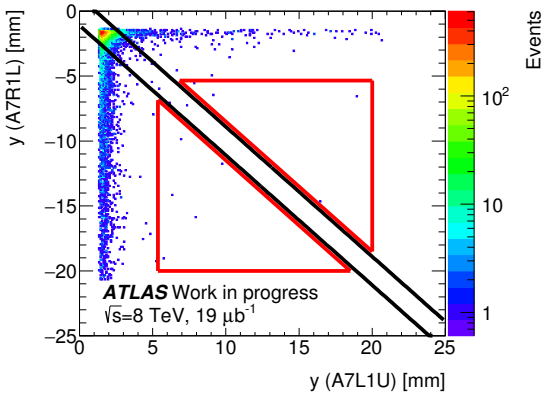

(d) RUC correlation with the DPE selection region (scaled).

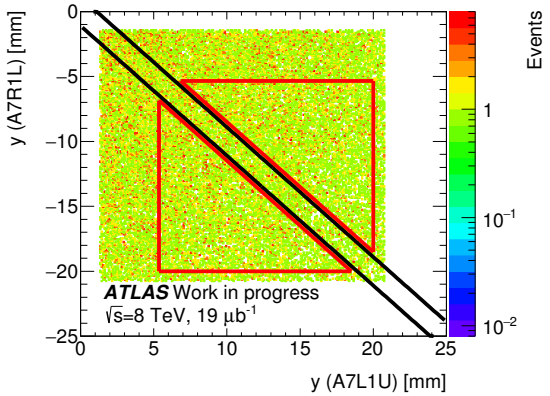

(e) DPE correlation with the DPE selection region.

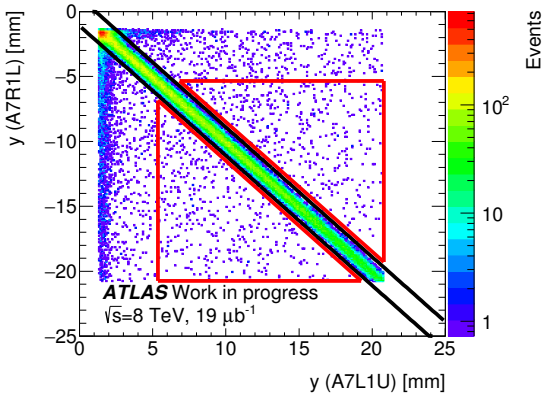

(f) Data correlation with the DPE selection region.

Figure 9.8: Correlation plots used to determine the background level. The black lines and ellipses show the elastic selection criteria, whereas the red lines show the boundaries for the regions used for the background template scaling. Figure 9.8d is scaled using Figure 9.8b and 9.8c.

9.7 Results

The number of events as a function of the four-momentum transfer, t, forms the basis for the final elastic measurement. Therefore, the following results are presented in terms of the t-spectrum. The details on how to reconstruct the t-spectrum from the data is the subject of Chapter 10.

The influence of the time and bunch dependence on the RUC background estimation is investigated in Figure 9.9 in a t-range where the background is non-negligible. The ratio between the predicted background in case 1 and 2 shows no significant difference in shape. The RUC background shape is therefore not sensitive to the time variations. The reason is deduced from the ratio between the predicted background in case 3 and 2, where the case 3 template has a reduced amount of SD due to the MBTS veto: Since also no shape difference is observed here, the fraction of SD events must be negligible compared to the fraction of halo events, hence the time dependent shape is also negligible.

Case 1 gives in principle the most correct background estimation, however it has a drawback: The many scaling factors for the individual templates for each luminosity block and bunch give non-trivial correlations between the t-bins, and this will complicate a later analysis step. Case 3 has different selection criteria than the data and should therefore only be used as a sanity check. Therefore, the case 2 background estimation is used as the nominal. However, the statistical uncertainty on the scaling does not cover the difference in scaling to case 1. Therefore, the scaling uncertainty is taken as 5.3 % for elastic arm 1 and 6.4 % for elastic arm 2 according to the fit results in Figure 9.9.

The $x - \theta_x$ correlation is not the only possibility for the template scaling. The other correlations involving the x-coordinates have been used as stability checks of the normalization, but it has not been necessary to increase the scaling uncertainty any further.

The raw t-spectrum for elastic candidates is shown in Figure 9.10 along with the estimated background from RUC and DPE. Three important observations can be made: First, the RUC background peaks at small t-values which gives a poor signal-to-noise ratio in particular for elastic arm 2. Second, the background shapes in the two arms are very different at small t confirming the inapplicability of the antigolden method. The last point is that the DPE level is down by about three orders of magnitude over the entire range. This is expected since the cross section for DPE is small compared to the elastic cross section, and furthermore it was seen in Figure 9.8e that most of the DPE events are removed by the elastic selection criteria. The DPE background contribution is therefore ignored in the rest of the analysis.

The number of elastic events and estimated background per luminosity block are shown in Figure 9.11. The periods of empty luminosity blocks are when the scraping takes place and the data taking is paused. The background level is lowest right after scraping but increases as the beam halo repopulates. The overall background level is 0.76 % in elastic arm 1 and 3.6 % in elastic arm 2. However as was shown in Figure 9.10, the background events peak at small t-values giving a poor signal-to-noise ratio in the most interesting CNI region. Another striking feature in Figure 9.11 is that the number of elastic events right after scraping is higher than right before scraping. Therefore, there must be at least one background dependent efficiency on the true elastic events.

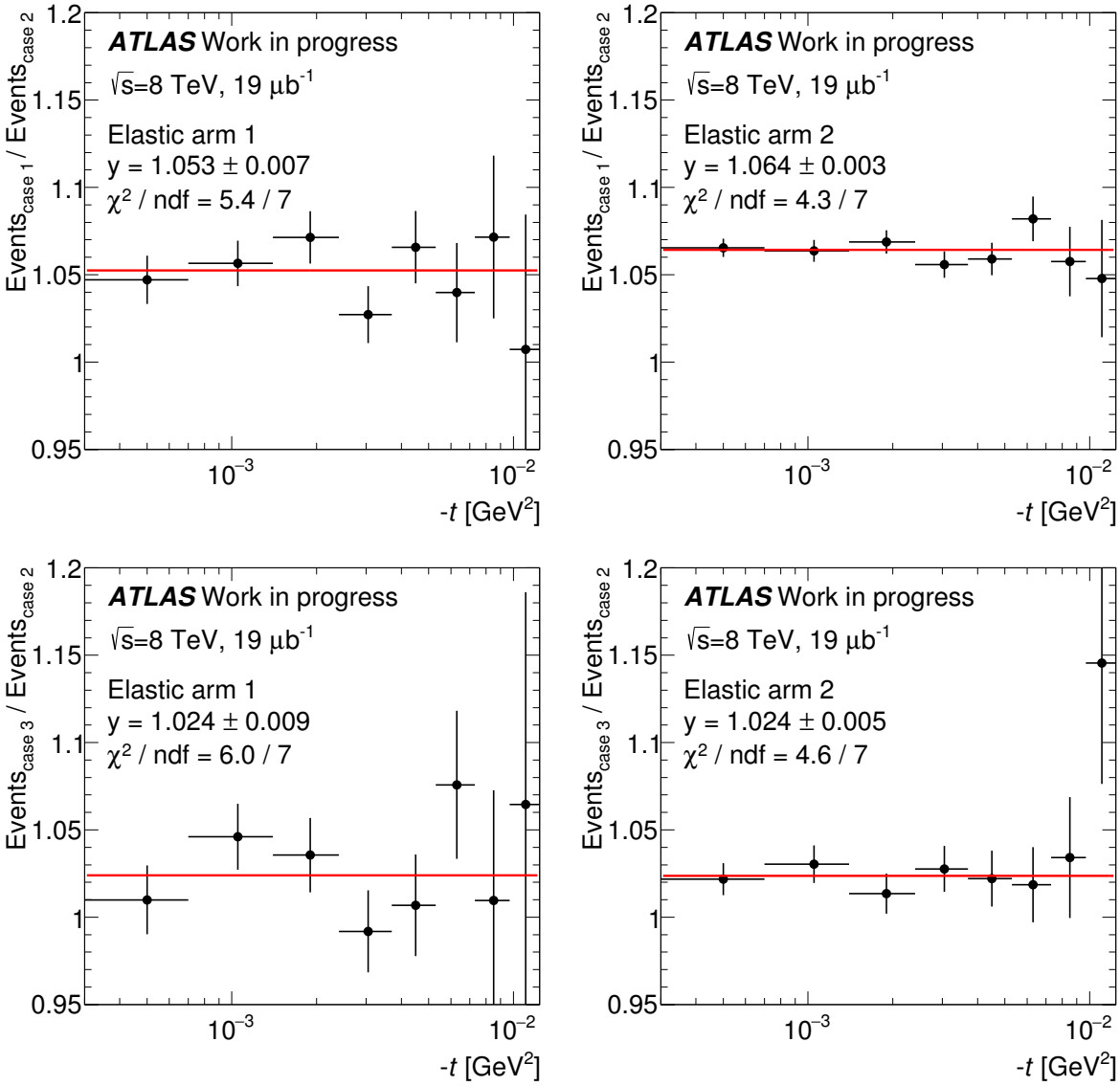

Figure 9.9: Ratio of the estimated RUC background spectrum between case 1 and 2 and case 3 and 2. The scaling uncertainty is not propagated, hence the bins are uncorrelated. The scale uncertainty for case 2 amounts to 2.9 % for arm 1 and 2.0 % for arm 2. A constant line is fitted to the data points.

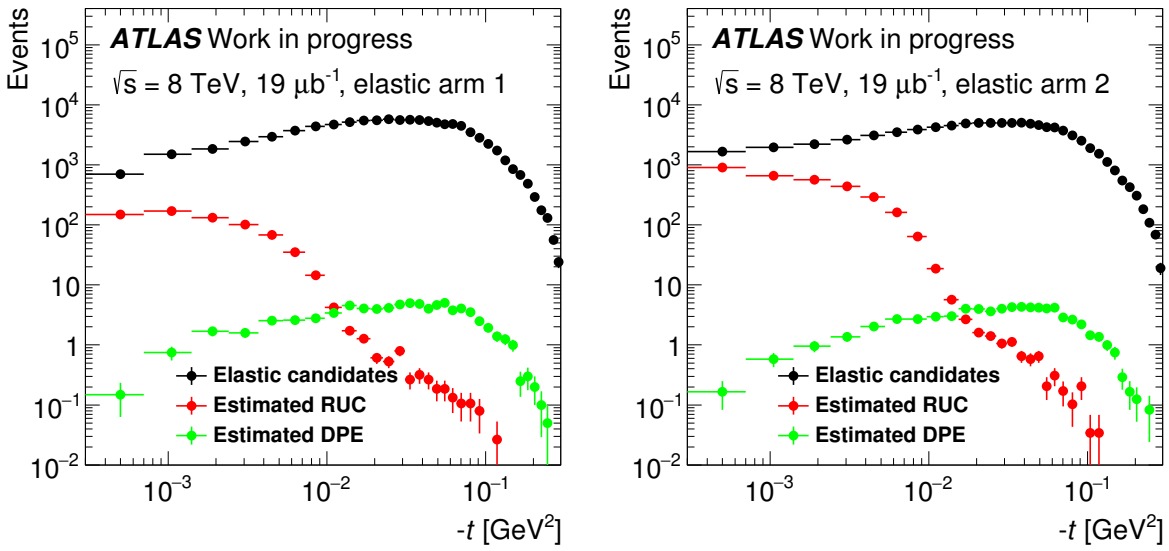

Figure 9.10: Raw t-spectrum for the elastic candidates and the estimated background.

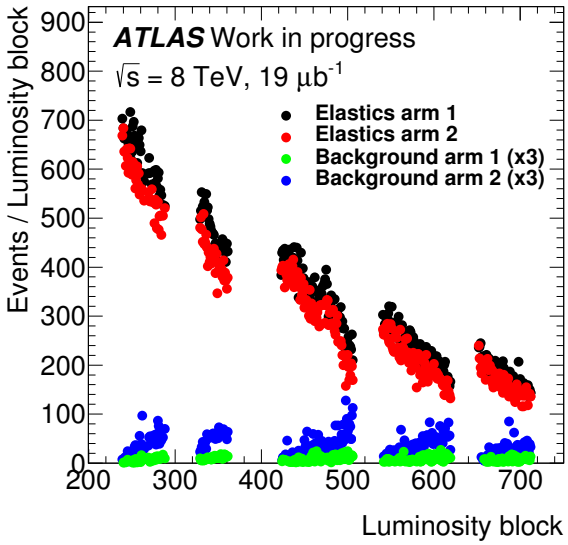

Figure 9.11: Number of elastic events after background subtraction as a function of luminosity block. The estimated background (x3) is also shown.

10 | Event reconstruction

The differential elastic cross section as a function of the four-momentum transfer, t, contains all relevant information about elastic scattering. The four-momentum transfer in elastic scattering at small angles can be written as

$$t \simeq -(p\theta^*)^2 \,, \tag{10.1}$$

where θ^* is the scattering angle at the IP and p is the proton momentum which for elastic scattering equals the beam energy. The beam energy is given by the LHC, whereas the scattering angles are inferred from the measured tracks in the ALFA detectors using knowledge about the LHC optics between the IP and ALFA as described in Section 4.4.1. The resolution of the tracks in ALFA and the beam emittance affect the precision on the reconstructed scattering angles, and the luminosity and detector efficiencies determine the scaling factor which must be applied for each event to obtain a cross section. This chapter describes the determination of all these experimental effects. Again, the previous elastic ALFA analyses have served as inspiration, but also new ideas have been invented.

Many of the effects are determined from the elastic data, and internal dependencies are unavoidable as shown in Figure 10.1: The elastic event selection described in the previous chapter depends on the detector alignment through the correlation cuts, and the alignment itself is determined from the elastic sample. Furthermore, the trigger and tracking efficiencies are determined from the elastic sample but are also needed as input to the vertical alignment. The detector resolution and the optics are both data driven and - along with the beam emittance - given as input to the fast simulation of elastic events used to find the boundaries for the correlation cuts in the event selection. In addition, the fast simulation is used to find phase-space corrections for the tracking efficiency. Therefore, the procedure is to iterate over the determination of all these effects until they jointly have converged to a stable solution.

The contents of this chapter is as follows: First, the beam parameters in terms of beam energy, emittance, optics, and luminosity are determined. Then follows the determination of the distance, alignment, resolution, and trigger and tracking efficiencies of the ALFA detectors. In the end, the t-reconstruction algorithms are presented along with their performance.

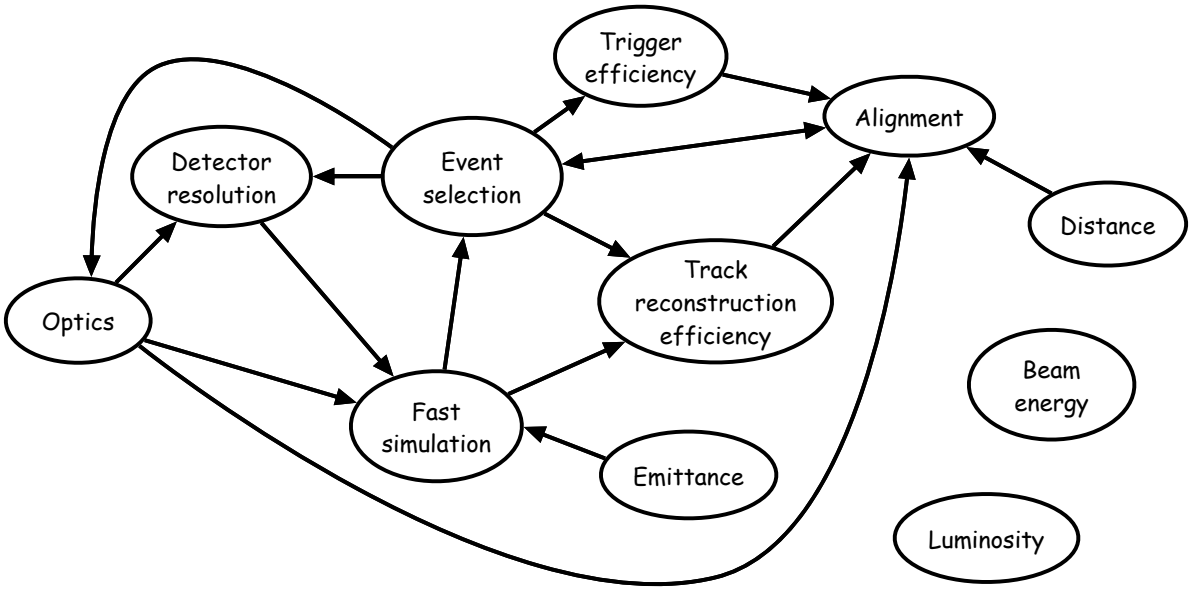

Figure 10.1: Experimental effects and their internal dependencies.

10.1 Beam energy

The beam energy needs to be known since the square of the beam energy is proportional to t and thus has a direct influence on the t-spectrum. The LHC beam energy was measured in special runs with protons in one beam and lead ions in the other beam. The proton beam has a different revolution frequency than the lead beam due to the different mass-per-charge ratio, and the proton momentum can be deduced from this revolution difference. The result is [39]:

$$E_{\text{beam}} = 3988 \pm 26 \text{ GeV} . \tag{10.2}$$

This is currently the official LHC beam energy.

10.2 Optics

From the transport Equation (4.7), the following six equations can be written, where the fact that the two elastic scattered protons naturally share the same IP has been used, and that $\theta_u^{*A} = -\theta_u^{*C}$ due to momentum conservation:

$$u_{241}^A = M_{11,241}^A u^* + M_{12,241}^A(\theta_u^* + D_u^A) \tag{10.3}$$
$$u_{237}^A = M_{11,237}^A u^* + M_{12,237}^A(\theta_u^* + D_u^A) \tag{10.4}$$
$$u_{237}^C = M_{11,237}^C u^* - M_{12,237}^C(\theta_u^* - D_u^C) \tag{10.5}$$
$$u_{241}^C = M_{11,241}^C u^* - M_{12,241}^C(\theta_u^* - D_u^C) \tag{10.6}$$
$$\theta^A = M_{21}^A u^* + M_{22}^A(\theta_u^* + D_u^A) \tag{10.7}$$
$$\theta^C = M_{21}^C u^* - M_{22}^C(\theta_u^* - D_u^C) \tag{10.8}$$

The contributions from the beam divergences are also included. From these equations and the measured positions in the ALFA detectors, it is possible to reconstruct the scattering angle, θ_u^*. The values of the matrix elements in the design optics were shown in Table 8.1. It is clear that the values of the transport matrix elements directly affects the reconstruction of the four-momentum transfer. Investigations of the optics in the previous ALFA analyses showed the need to find corrections to the design optics in order to describe the elastic data. This section briefly describes the procedure to determine the optics, which closely follows the procedure from the previous analyses. It is done by two collaborators and is not finished at the time of writing. The author has invented a new method to handle the systematic uncertainties from the optics, which will be presented at the end of the section.

10.2.1 Optics constraints from elastic data

The elastic data is used to measure constraints between the matrix elements. One example is the correlation between the y-coordinates in the inner stations on each side of the IP (see Figure 9.6 left). The coordinates are given by Equation (10.4) and (10.5), and since the M_{11}^y's are very small, this correlation provides a measurement of the $M_{12,237}^{C,y}/M_{12,237}^{A,y}$ ratio, which the true optics has to fulfill. The measured matrix ratio in the data is influenced by detector resolution and beam divergence, and the effects are determined by simulation. The simulation is provided by the author and is described in detail in the next chapter. In a similar way, other coordinate correlations are used to derive ratios between other matrix elements.

Another type of constraints come from the reconstructed scattering angles. Since elastic scattering is isotropic in azimuth angle, the M_{12}^x/M_{12}^y ratio can be determined from a plot of θ_x^* vs. θ_y^*. If the optics is correct, the contours of equal density will be circles. If not, it will be ellipses.

The Equations (10.3)-(10.8) can be combined in different ways to obtain the scattering angles. The different combinations should on average yield the same scattering angle, and a measurement of the difference between them gives further constraints for the true optics.

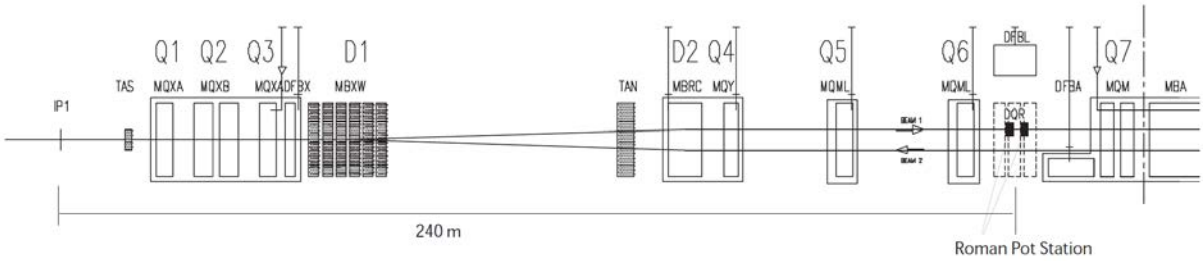

Figure 10.2: Sketch of the magnets between ATLAS and ALFA. Quadrupoles are labelled with a Q and dipoles with a D [29].

10.2.2 Optics fit

The magnets between the ATLAS IP and ALFA are shown in Figure 10.2. The design optics is adjusted by changing the magnet currents of the six quadrupole magnets, Q1-6, which change the magnetic fields. A precision of 0.1 % for the magnet currents was used in the previous analyses. The constraints on the matrix elements along with their uncertainties are used in a χ^2 minimization with some of the magnet currents as free parameters. The currents of the Q4s are not varied as they had a negligible effect on the optics in the past, and the currents of Q1 and Q3 are combined to a single variation. This gives in total eight magnet currents to be varied. The ALFA constraints do not give information about single matrix elements, and there exist several different combinations of magnet strengths that minimizes the χ^2. The resulting optics is therefore referred to as the *effective* optics.

In the previous analyses, the Q1 and Q3 magnet currents were varied together to obtain the effective optics, but this was just one possible solution. At the time of writing, it is unknown which magnets will be used in the fit. However, preliminary studies by the collaborators responsible for the optics show that the design optics with all magnet currents at their nominal values fulfill the matrix constraints to a reasonable degree. In the absence of the final effective optics, the design optics will therefore be used throughout the analysis.

10.2.3 Systematic uncertainty

The systematic uncertainty from the optics on the reconstructed t-spectrum is determined by variations of the magnet currents. The procedure in the previous analyses was to make all possible optics variations with the magnet currents at $\pm 1\sigma$ from their effective optics values. The systematic uncertainty at a given t-value was then taken as the maximum difference between the effective optics and any of the variations. Such a procedure will not be used in this analysis for two reasons:

1) There is a risk to overestimate the systematic uncertainty by taking the variation with the maximum deviation from the effective optics as a 1σ systematic uncertainty. Consider the case where the maximum deviation occurs when all magnet currents are moved up by one standard deviation. This scenario will not have a

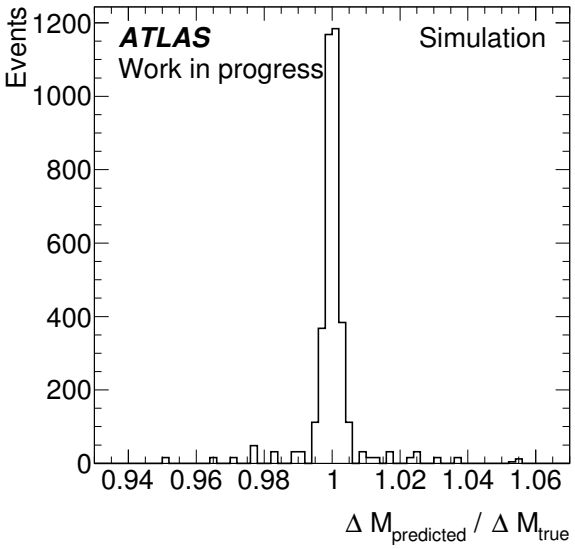

Figure 10.3: Ratio of the predicted and true matrix element correction when the magnet currents are varied with one standard deviation.

34.1 % probability to happen unless the calibration of the magnet currents are 100 % correlated.

2) The maximum deviation from the effective optics is taken for each t-value individually. This means that one variation yields the systematic uncertainty at one t-value whereas a different variation can be used for another t-value, i.e. inconsistent set of optics are used to address the systematic uncertainty.

Instead, an approximate functional dependence of the magnet currents on the matrix elements are derived such that the magnet current uncertainties can be propagated directly to the t-spectrum. From MadX [40], a collaborator has provided $2^8 = 256$ variations of the optics where the eight magnet currents are at $\pm 1\sigma$ from the design optics. It is assumed that the corrections of the matrix elements from the design optics can be written as a linear combination of the magnet currents. Each of the proportionality constants are derived in two cases: With all other magnet currents set to -1σ and with all other magnet currents set to $+1\sigma$. The difference is typically less than 5 % and the average is therefore used. Figure 10.3 shows the ratio between the matrix element corrections predicted by the simple linear combination of the magnet currents and the true correction found with MadX. All matrix element corrections for all 256 optics variations are plotted. The difference is less than 1 % for the vast majority of events. Since it is the uncertainty on the optics uncertainty, the simple linear combination is considered sufficient.

	Horizontal		Vertical	
	Beam 1	Beam 2	Beam 1	Beam 2
BCId 101 in-going	2.464	4.592	1.375	2.516
BCId 101 out-going	2.205	3.968	1.378	2.468
BCId 1886 in-going	2.392	—	1.402	2.294
BCId 1886 out-going	2.240	4.238	1.393	2.282

Table 10.1: Normalized emittance in $\mu\text{m} \cdot \text{rad}$ in ATLAS run 213268 from wire scans in luminosity block 540 [41]. One wire scan failed.

10.3 Emittance

The emittances of the LHC beams have direct influence on the measured t-spectrum. The emittance is related to the beam divergence which contributes to the angles of the outgoing protons and therefore also the reconstruction of t. Furthermore, the emittance determines the beam spot width. Since there is no reconstructed vertex in the ATLAS ID for an elastic collision, the beam spot is used in Equations (10.3)-(10.8) to reconstruct t which gives an additional uncertainty on t; a large emittance gives a large beam spot width and hence a worse resolution on t.

The emittance was measured approximately half way through the run by wire scans and the values are shown in Table 10.1. The in-going and the out-going measurement of a given bunch in a beam should return the same emittance. The uncertainties on the wire scans were set to 10 % in the previous analyses, and it is seen that the emittances of the two colliding bunches agree within the uncertainties. Therefore, a combined value for the two bunches will be used. A simple average is used, and to be conservative the measurements are assumed to be 100 % correlated meaning that the uncertainty is 10 % of the mean. The results are

$$\begin{aligned}
\epsilon_x^{\text{Beam 1}} &= 2.33 \pm 0.23 \ \mu\text{m} \cdot \text{rad} \ , \\
\epsilon_x^{\text{Beam 2}} &= 4.27 \pm 0.43 \ \mu\text{m} \cdot \text{rad} \ , \\
\epsilon_y^{\text{Beam 1}} &= 1.39 \pm 0.14 \ \mu\text{m} \cdot \text{rad} \ , \\
\epsilon_y^{\text{Beam 2}} &= 2.39 \pm 0.24 \ \mu\text{m} \cdot \text{rad} \ .
\end{aligned}$$

In the following, alternative emittance determinations from other inputs are used as stability checks of the wirescans.

A measurement of the beam spot width is used as a stability check of the wire scans. The width is related to the emittance through the formula

$$\sigma_{\text{Beam spot}} = \left(\frac{1}{\sigma^2_{\text{Beam 1}}} + \frac{1}{\sigma^2_{\text{Beam 2}}} \right)^{-1/2} = \frac{\sqrt{\beta^*/\gamma}}{\sqrt{1/\epsilon^{\text{Beam 1}} + 1/\epsilon^{\text{Beam 2}}}} \ , \tag{10.9}$$

where it has been used that $\sigma^2 = \epsilon\gamma\beta^*$ and a Gaussian distribution is assumed for both beams. The beam spot width is measured by the ATLAS ID for inelastic events and is shown in Figure 10.4. By eye, the average widths are 0.58 mm in x and 0.48 mm in y

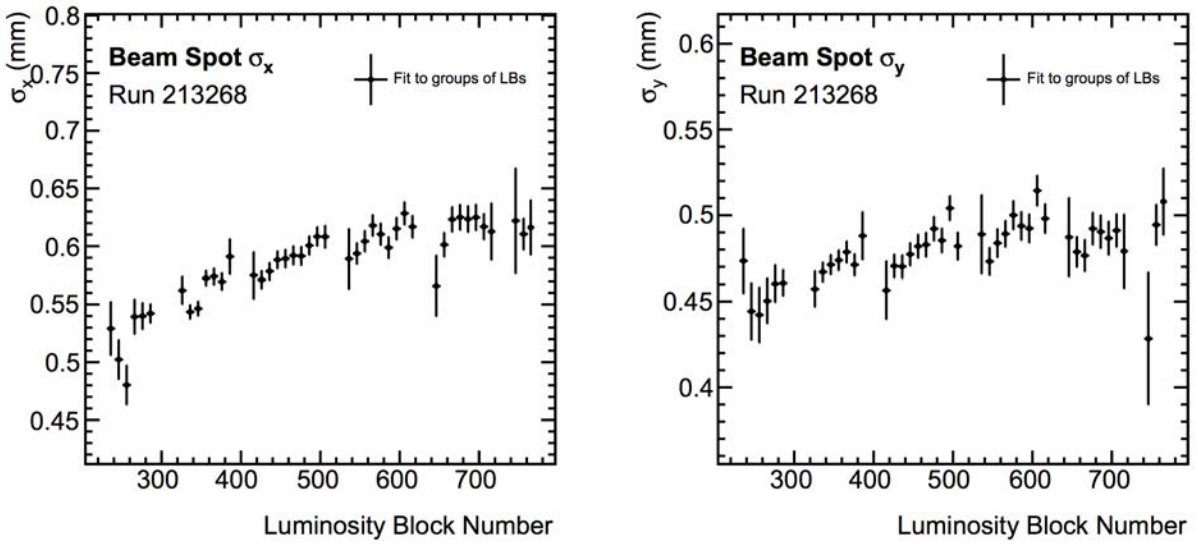

Figure 10.4: Beam spot measurement from the ATLAS inner detector in run 213268 [42].

which agree well with the calculations from the emittance of 0.594 ± 0.022 mm in x and 0.454 ± 0.017 mm in y. However, it is seen that the beam spot width and therefore also the emittance changes over time in a non-trivial way in both x and y. Instead of trying to infer the time dependence of the emittance from the beam spot width, the uncertainty on the emittance is increased from 10 % to 30 % such that the uncertainty band of $\pm 1\sigma$ covers the interval of the measured beam spot width.

Another stability check is available via the convoluted divergence in vertical direction, D_{conv}, found directly from elastic ALFA data, since

$$D_{\text{conv}} = \sqrt{\frac{\epsilon_y^{\text{Beam 1}} + \epsilon_y^{\text{Beam2}}}{\gamma\beta^*}} \, . \tag{10.10}$$

The vertical angle is calculated on both sides of the IP and the width of the distribution of

$$\theta^*_{y,A} + D_y^A + (-\theta^*_{y,C} - D_y^C) = D_y^A - D_y^C \tag{10.11}$$

is a measure of the convoluted divergence of the two beams. The relative contribution from the detector resolution to the width is of the order 1 % and can be neglected. The distribution is shown in Figure 10.5 along with a Gaussian fit. The convoluted divergence calculated from the emittance (with increased uncertainties) is 0.94 ± 0.10 μrad. Though the fit does not describe the tails of the distribution, it still allows to conclude that the width of the distribution is inside the 1σ uncertainty band from the wire scans.

The final emittance estimates are

$$\epsilon_x^{\text{Beam 1}} = 2.33 \pm 0.70 \ \mu\text{m} \cdot \text{rad} \, , \tag{10.12}$$

$$\epsilon_x^{\text{Beam 2}} = 4.27 \pm 1.28 \ \mu\text{m} \cdot \text{rad} \, , \tag{10.13}$$

$$\epsilon_y^{\text{Beam 1}} = 1.39 \pm 0.42 \ \mu\text{m} \cdot \text{rad} \, , \tag{10.14}$$

$$\epsilon_y^{\text{Beam 2}} = 2.39 \pm 0.72 \ \mu\text{m} \cdot \text{rad} \, . \tag{10.15}$$

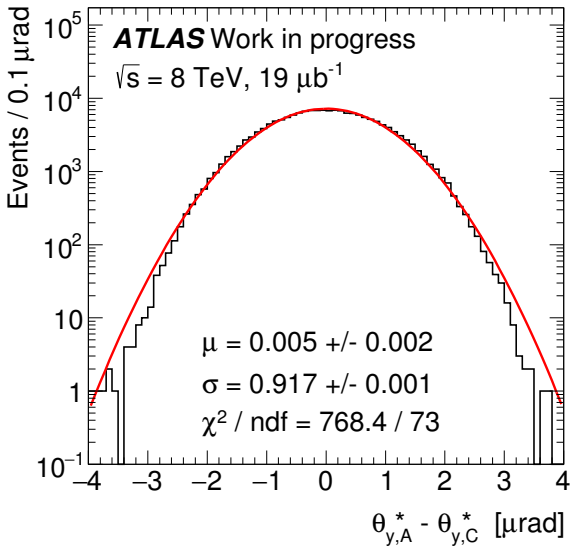

Figure 10.5: Convoluted vertical divergence from the reconstructed vertical scattering angles for elastic events.

10.4 Luminosity

The luminosity measurement is provided by the ATLAS luminosity group and is shown in Figure 10.6 for the three algorithms that are most reliable for this run. Details about the luminosity estimation can be found in Ref. [24].

The three algorithms are in very good agreement. The systematic uncertainty on the LUCID and BCM algorithms come from the VdM calibration and from background subtraction. The background subtraction is dominating for BCM which gives a higher systematic uncertainty. Therefore, LUCID is chosen as the default luminometer, and the total uncertainty is given as the statistical and systematic uncertainties added in quadrature. The systematic uncertainty for the vertex counting algorithm is not yet available but the agreement with the LUCID algorithm is good even within only the statistical uncertainty.

10.5 Distance

The distance measurement is the first step in the alignment of the detectors. The procedure follows closely what was done in Ref. [11], as described in Section 7.1. Therefore, only the differences will be highlighted as well as the results.

The selection criteria have been relaxed in order to keep a low statistical uncertainty. The veto on the MD triggers is not used, since the MDs are so close to the beam that they will fire much more frequently. As will be described below, the amount of large angle events are negligible for this data set, hence criterion no. 4 is also removed. Criterion no. 5 was introduced to avoid a trigger bias in the determination of the vertical profile. With this cut included, the statistical uncertainties are much larger than the effect of the

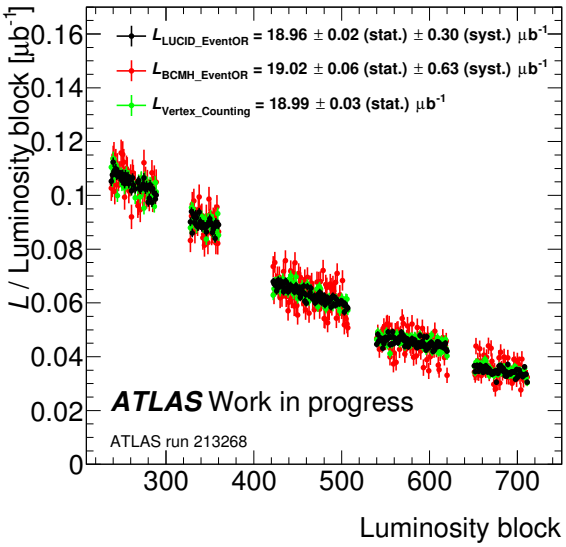

Figure 10.6: Luminosity for ATLAS run 213268 for three different algorithm. The systematic uncertainty on the vertex counting is not determined at the time of writing.

vertical profile. Therefore, criterion no. 5 is not used since the vertical profile is anyway only used to address a systematic uncertainty. Furthermore, the veto on fiber hits in the opposite sided OD (criterion no. 8) is removed. It will however by used for a systematic check.

The horizontal distribution of tracks in the ODs is important since the OD fibers are not exactly horizontal. In Section 7.1.3, the horizontal distribution was estimated in the MDs and extrapolated to the ODs. Unfortunately, this procedure is not possible in this data set, because the number of hits at large x-values is too small. Instead, the default horizontal distribution is chosen to be uniform. There exists no reliable halo simulation for normal running conditions, and in this run the halo is disturbed by the scraping and is even less known. To specify the systematic uncertainty, the most extreme scenario is used where all events are considered to hit the OD right at the vertical edge closest to the beam. Such a scenario is not completely unlikely because of the LHC beam screen located only four meters before ALFA.

The determination of the vertical distribution of tracks combined with fiber and MAPMT efficiencies is performed exactly as in Section 7.1.3. Again, it is only used for systematics.

The fit procedure has also not changed, except that only a single Gaussian is used for the vertical angular profile. The double Gaussian was introduced to describe events with large angles, but such events are negligible in this data set. Figure 10.7 shows the fit to data in one of the stations using a single Gaussian, and the agreement is excellent. The difference in distance between using a single Gaussian and a double Gaussian is well within the statistical uncertainty and is not included as a systematic uncertainty.

In the distance measurement for Ref. [11], the templates did not describe the data in a region next to the signal peak (see Section 7.1.4). Fortunately, there is no such

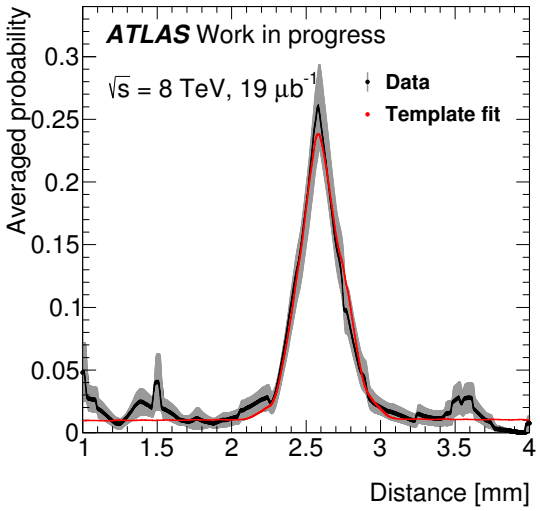

Figure 10.7: Visualization of the fit result overlayed on the data from detector A7L1+. Only a region around the distance peak is shown. Details on the visualization are described in Section 7.1.3.

discrepancy between this data and the template fit as seen on Figure 10.7, and a similar procedure is therefore not needed. Anyway, a more inclusive sample is used to find a potential bias due to the selection criteria. The criteria no. 3 and 4 are not used in this data set, which leaves only criterion no. 8 for the systematic check. This will catch the effect of MAPMT cross-talk.

The results are shown in Table 10.2. The observed difference in the distance for a systematic variation is taken as the 1σ uncertainty, and the combined uncertainty is found by adding the individual contributions in quadrature. The systematic uncertainty related to the horizontal track distribution is dominating, closely followed by the MD-OD calibration. The combined uncertainty is comparable to the results in Section 7.1.6.

Station	B7L1	A7L1	A7R1	B7R1
Distance	2580	2544	2457	2429
Uncertainties				
Statistical and vertical angular distribution	2	5	4	3
Selection	3	2	4	1
Vertical track distribution and efficiencies	0	2	3	6
Horizontal track distribution	20	11	7	9
MD-OD calibration	80	8	9	8
Combined uncertainty	83	15	13	14

Table 10.2: Distances and their uncertainties between the ALFA Main Detector edges for the $\sqrt{s} = 8$ TeV, $\beta^* = 1$ km run. All numbers are in micro meters.

10.6 Alignment

The track based alignment is made by a collaborator with the same procedure as in Ref. [11]. It depends on inputs from the optics and the elastic track reconstruction efficiency which is not finished at the time of writing. Therefore, the final results for the alignment including systematic uncertainties have not yet been worked out.

The alignment of each of the detectors consists of three parts: The rotation in the $x - y$ plane, the horizontal position and the vertical position. The procedure is based on the azimuth scattering symmetry of elastic events. The elastic events are selected as described in Chapter 9 except that the edge cut is increased to 2 mm in order to remove the majority of background events, whose pattern is not guaranteed to be symmetric. This cut will not give a bias in the alignment but only increase the statistical uncertainty. It is clear that the event selection depends on the alignment through the correlation cuts and vice versa, hence both must be done in iterations until convergence is met.

10.6.1 Rotation

The detectors can happen to be rotated in the $x - y$ plane wrt. the beam. The LHC magnets between the IP and ALFA do not mix the horizontal and vertical positions, hence the linear correlation between the x and y coordinates for elastic events is a measure of the rotation of the detector.

The statistical uncertainty on the rotation correction is found with the bootstrap method where a set of pseudo data is obtained by weighting each event by a Poisson number with a mean of one. The spread in the rotation correction for many sets of pseudo data is then used as the uncertainty. The systematic uncertainties come from the choice of boundaries for the elastic correlation plots and from the iterative stability of the event selection and alignment. The statistical uncertainty is about 0.5 mrad for each detector, and though the systematics are only preliminary, it can be concluded that the statistical uncertainty is completely dominating. Therefore, the uncertainties can be treated as fully independent between the detectors.

10.6.2 Horizontal position

The distribution of x-coordinates for elastic events must have a center at zero in the beam coordinate system, since the elastic scattering angle is symmetric in azimuth angle. Any offset in this distribution comes from a misalignment in the horizontal position. Three different methods to find the offset are considered: A Gaussian fit to the distribution, an arithmetic mean, and a median value. Both the Gaussian fit and the median can be biased due to the fiber pattern in the detector, whereas outliers can bias the arithmetic mean. The median is chosen as the default method and the others are used for systematics. As for the rotation, additional systematic uncertainties come from the event selection and iterative stability. The statistical uncertainty of 2 μm obtained with the bootstrap method is dominating over systematics, and the horizontal positions of the detectors are treated as fully independent.

10.6.3 Vertical position

The vertical position is decomposed into two measurements: The distance between the detectors in a station, which was described in detail above, and an offset of the station wrt. the beam center. The determination of the offset uses the azimuth symmetry of elastic events, i.e. the number of events at $-y$ in the lower detector equals the number of events at $+y$ in the upper detector for correctly aligned detectors. The distribution of y-coordinates in the upper and lower detectors are compared with a sliding window technique. The number of events in a given y-range in the upper detector is found, and the station offset is adjusted until the similar y-range in the lower detector has the same event yield. A total of 5000 windows with different widths and positions are used. The offset found for each window is plotted in a histogram and the peak of the distribution is used for the final offset. In addition, a Kolmogorov-Smirnov test comparing the distributions in the upper and lower detector is used to find the offset, and the difference to the sliding window result is taken as a one standard deviation systematic uncertainty.

It is clear that a difference in efficiencies between the upper and lower detectors needs to be corrected for before the vertical offset can be found. The efficiencies are addressed in the coming sections, and the efficiency uncertainties are propagated to the vertical offset as a systematic uncertainty. The allowed y-range for the windows and the iterative stability with the event selection are also subject to systematic variations. The statistical uncertainty is again found with the bootstrap method and dominates over systematic uncertainties.

10.6.4 Vertical optimization

The very small value of the transport matrix element M_{11} in the vertical plane (Table 8.1) allows to correlate the vertical positions between the stations and thereby reduce the uncertainty on the vertical alignment. The y-position of an elastic track is to a good approximation determined only by the scattering angle:

$$y^A_{241} \simeq M^A_{12,241} \cdot (\theta^*_y + D^A_y) \tag{10.16}$$

$$y^A_{237} \simeq M^A_{12,237} \cdot (\theta^*_y + D^A_y) \tag{10.17}$$

which means that the y-value in the inner station can be extrapolated to the outer station as:

$$y^{\text{extrapolated}}_{241} = y^{\text{measured}}_{237} \cdot \frac{M^y_{12,241}}{M^y_{12,237}} \ . \tag{10.18}$$

A non-zero mean in the distribution of $y^{\text{measured}}_{241} - y^{\text{extrapolated}}_{241}$ shows a misalignment between the inner and outer station. The same procedure can be applied for two stations on each side of the IP, but here the beam divergence limits the precision of the extrapolation because the angle in no longer exactly the same. The beam divergence is sufficiently small in this data set that the extrapolation across the IP is actually meaningful, in contrast to Ref. [11] where another procedure had to be followed.

	D_1	D_2	D_3	D_4	O_1	O_2	O_3	O_4	Uncertainty
D_1	1.000	0.986	0.960	0.957	0.000	0.001	-0.005	-0.004	13.9 μm
D_2	0.986	1.000	0.963	0.959	-0.001	-0.001	-0.002	-0.002	14.1 μm
D_3	0.960	0.963	1.000	0.986	0.001	0.001	0.002	0.002	14.1 μm
D_4	0.957	0.959	0.986	1.000	0.002	0.002	0.001	0.003	14.0 μm
O_1	0.000	-0.001	0.001	0.002	1.000	1.000	-0.999	-0.999	43.4 μm
O_2	0.001	-0.001	0.001	0.002	1.000	1.000	-0.999	-0.999	44.1 μm
O_3	-0.005	-0.002	0.002	0.001	-0.999	-0.999	1.000	1.000	44.2 μm
O_4	-0.004	-0.002	0.002	0.003	-0.999	-0.999	1.000	1.000	43.5 μm

Table 10.3: Correlation matrix and uncertainties for the four distances D and the four offsets O in the vertical alignment. The subscript refers to the station number, where 1 is B7L1, 2 is A7L1, 3 is A7R1 and 4 is B7R1.

The constraints from the extrapolation are used in a χ^2 minimization routine which takes the individual uncertainties on the distances and offsets into account and produces the final distances and offsets[1].

The correlation matrix between the eight parameters returned by the χ^2 minimization is listed in Table 10.3 along with the parameter uncertainties. The four distances are highly correlated and so are the four offsets, but there is close to zero correlation between the offsets and distances. This is as expected, since the extrapolation constraints do not mix the detectors in the two elastic arms. The distance uncertainty on station B7L1 is greatly reduced wrt. the actual distance measurement in Table 10.2 due to the strong correlation with A7L1. This means that a precise distance measurement in the inner stations is actually sufficient.

The offsets are -0.059 mm, -0.088 mm, 0.114 mm, and 0.149 mm, for station B7L1, A7L1, A7R1, and B7R1, respectively. This means that elastic arm 2 is on average about 100 μm closer to the beam than elastic arm 1, which can partly explain why the background level is much higher. The rather asymmetric alignment was not intended but can be explained because a BBA was only performed in a previous LHC fill to save beam time for data taking.

10.7 Detector resolution

The resolutions of the detectors influence the precision on the reconstructed scattering angles and must be determined. The overall procedure is the same as in the previous analyses: The convoluted resolution of an inner and outer detector is measured with the elastic data, and the ratio between the contributions is taken from a full simulation.

The extrapolation of the y-coordinate from the inner to outer detector is used like for the vertical alignment, Equation (10.18). However, now the spread in the distribution of $y_{241}^{\text{measured}} - y_{241}^{\text{extrapolated}}$ is of interest since it is a measure of the convoluted resolution of

[1]The precision on the distance measurement for station B7R1 has manually been set to 100 μm before the optimization because a miscalibration of this scale was observed in the previous analyses.

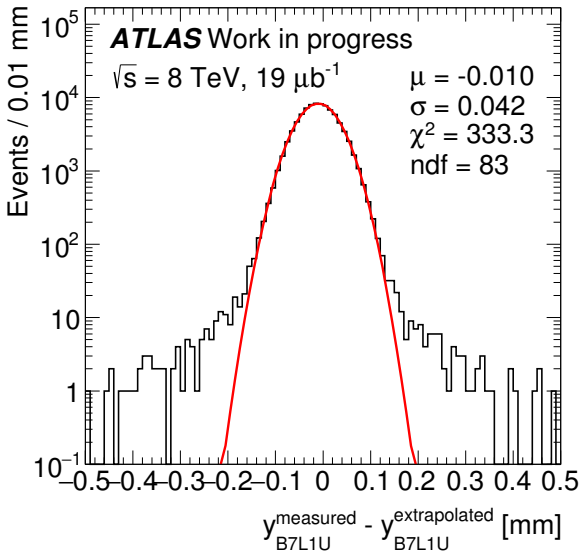

Figure 10.8: Convoluted resolution for the detector pair B7L1U-A7L1U.

the inner and outer detector. Figure 10.8 shows this distribution for one of the detector pairs along with a Gaussian fit. Clearly, there are non-Gaussian tails in the distribution, and a double Gaussian fit used in Ref. [11] is required to give a good description of the data. However, for simplicity reasons the single Gaussian fit is used here since the broad Gaussian constitutes less than 0.1 % of the events, and the previous analyses showed that the effect of detector resolution on the physics parameters is small.

It was observed in the previous analyses that the resolution depends on the position in the detector. This is still the case in this data set as shown in Figure 10.9 where there is a clear trend of increasing precision further away from the beam for the upper detectors. For the lower detectors, the resolution is more constant. The decrease in precision closer to the beam is understood as a consequence of the larger distance to the support point of the fibers on the titanium plates. The deviation of the fibers from the design positions are suspected to be larger farther from the titanium. It is not clear why there is a difference between the upper and lower detectors.

A straight line is fit to the data, which provides a sufficient description. There are large fluctuations in the spectra and similar fluctuations are observed in the previous analyses. Therefore, the interpretation is that it is a result of the fiber patterns. In order to reduce the effect of the fluctuations, a total number of 1000 histograms with different bin sizes and positions are fitted with a straight line. The average slope and intercept are used as the nominal values and the RMS as the uncertainties. This is in contrast to the procedure in Ref. [11] where a y-independent resolution was used as the nominal and a single straight line fit for systematics.

The same procedure can not be used for the x-coordinate. The M_{11}^x/M_{12}^x ratio is higher than in y which means that the x-coordinate depends on both x^* and θ_x^*. Therefore, the extrapolation will not work. Fortunately, both test beam results [43] and a full simulation at $\sqrt{s} = 7$ TeV (see Ref. [44] for details) show that the resolution in x is the same as in y.

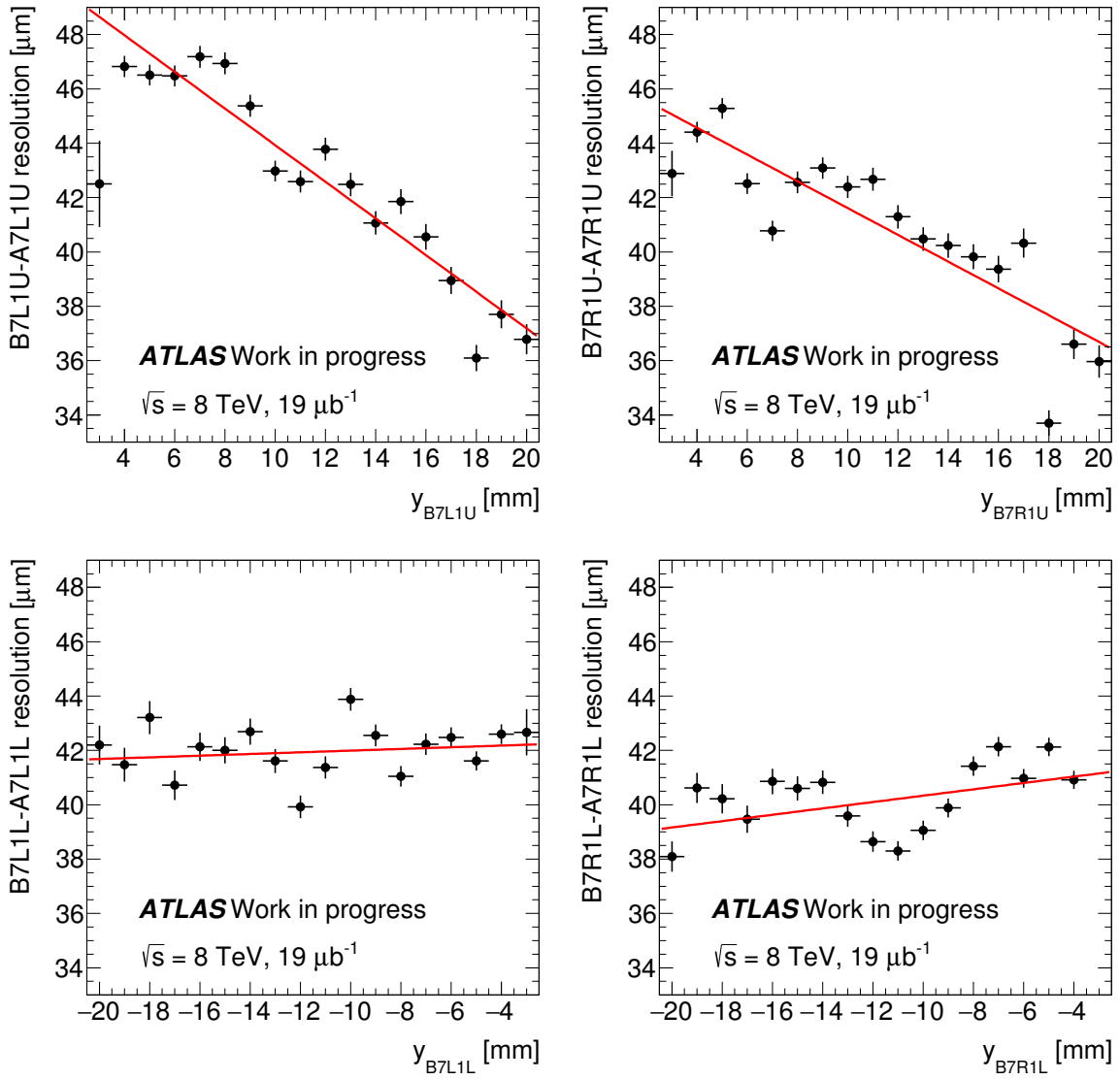

Figure 10.9: Convoluted resolution in the four detector pairs as a function of the y-coordinate in the outer station. A straight line is fit to the data.

	Slope [μm/mm]	Intercept [μm]	Outer/inner ratio
B7L1U-A7L1U	-0.67 ± 0.01	50.5 ± 0.1	1.073 ± 0.026
B7L1L-A7L1L	0.03 ± 0.01	42.2 ± 0.1	1.192 ± 0.067
B7R1U-A7R1U	-0.49 ± 0.01	46.4 ± 0.1	0.919 ± 0.037
B7R1L-A7R1L	0.12 ± 0.01	41.5 ± 0.1	1.162 ± 0.23

Table 10.4: Results for the resolution in the four detector pairs.

	Trigger logic	Efficiency $\pm$ stat. $\pm$ syst.
$\varepsilon_{\text{L1\_ALFA\_ELAST11}}$	B7L1U AND A7L1U AND A7R1L AND B7R1L	$97.58 \pm 0.05 \pm 0.02$
$\varepsilon_{\text{L1\_ALFA\_ELAST12}}$	B7L1L AND A7L1L AND A7R1U AND B7R1U	$98.66 \pm 0.04 \pm 0.02$
$\varepsilon_{\text{L1\_ALFA\_ELAST15}}$	(B7L1U OR A7L1U) AND (A7R1L OR B7R1L)	$\mathbf{99.72 \pm 0.02 \pm 0.01}$
$\varepsilon_{\text{L1\_ALFA\_ELAST18}}$	(B7L1L OR A7L1L) AND (A7R1U OR B7R1U)	$\mathbf{99.75 \pm 0.02 \pm 0.01}$

Table 10.5: Efficiencies for the different elastic CTP items. All numbers are in percent.

This is completely expected considering that the coordinates are transformed from the U-V coordinate system of the fibers. Therefore, the x-resolution is taken as the resolution for the y-coordinate.

The individual detector resolutions are calculated from the convoluted resolutions by a full simulation of the ratio between the outer and inner detector resolutions. The full simulation was made at $\sqrt{s} = 7$ TeV, but since it predicts the correct convoluted resolution in the detector pairs to within 1 μm, the ratios are considered to be appropriate. The detector resolutions measured in a 120 GeV hadron test beam [43] are not reliable since the detector resolution improves with increasing energy. Instead, the difference between the test beam ratio and the ratio in the full simulation is taken as a one standard deviation systematic uncertainty. Table 10.4 summarizes the results. The large uncertainty for the ratio in the B7R1L-A7R1L detector pair is unknown.

10.8 Trigger efficiency

The elastic trigger efficiency is performed by a student under supervision of the author. It follows closely the procedure described in Section 6.5 and only the results and a discussion will be given here.

The efficiencies for some of the elastic trigger items are shown in Table 10.5. The items L1_ALFA_ELAST15/18 are used for the actual triggering and the efficiencies are close to 100 %. As explained in Section 9.1, the L1_ALFA_ELAST11/12 are used as an offline criterion. This will reject up to 2 % more elastic events, but the criterion is expected to increase the precision of the elastic track reconstruction efficiency described in the next section.

The statistical uncertainty has increased wrt. the results for Ref. [11] in Table 7.5 since the number of recorded elastic events is smaller by about a factor 20. Furthermore, the systematic uncertainty has increased with the main contribution coming from whether or not the track correlation cuts are used. Without these cuts, there will be a significant amount of background events. The efficiency decreases when these events are included, hence the background trigger efficiency must by slightly lower than for elastic events.

10.9 Elastic track reconstruction efficiency

The elastic analysis is based on events where all four ALFA detectors in an elastic arm have a track. However, for some events the tracking algorithm fails for one or more detectors. One of the reasons for a failed track reconstruction are fiber efficiencies lower than 100 % which give too few fiber hits to fulfill the requirement on the number of overlapping fibers. Other reasons are random fiber/MAPMT noise or pile-up of shower and background events which give too many fiber hits for a track to be identified.

The elastic track reconstruction efficiency, $\varepsilon_{\text{reco}}$, is the probability to have tracks in all four detectors for an elastic event and is estimated from the data. It has been necessary to reformulate almost the entire procedure compared to the previous analyses due to the much higher (and time dependent) background level. The author has provided many of the ideas whereas a collaborator is responsible for the final results.

The elastic track reconstruction efficiency is defined as

$$\varepsilon_{\text{reco}} = \frac{E_4}{E_{\text{total}}} = \frac{E_4}{E_4 + E_3 + E_2 + E_1 + E_0} \,, \tag{10.19}$$

where E_n is the number of elastic events inside the detector acceptance with tracks in n detectors. It must be determined for both elastic arms. What is really measured in the detectors is the number of events that fulfill the elastic selection criteria, hence the irreducible background must be estimated and subtracted. The formula is therefore rewritten as

$$\varepsilon_{\text{reco}} = \frac{N_4 - B_4}{N_4 - B_4 + N_3 - B_3 + N_2 - B_2 + N_1 - B_1 + N_0 - B_0} \,, \tag{10.20}$$

where N_n is the number of elastic candidates and B_n is the estimated background. Several different combinations of failed detectors exist where $n = 1, 2, 3$, and $N_{n=1,2,3}$ and $B_{n=1,2,3}$ are therefore short hand notation for the sum of events in these topologies.

10.9.1 Signal definition

The N_4 is selected with the criteria described in Chapter 9. The $N_{n<4}$ can be selected in the same way but only a reduced set of the correlation criteria can be applied, e.g. in an event with a missing track in the first station the $x^A_{241} - x^C_{241}$, $y^A_{241} - y^C_{241}$, and $x^A_{237} - \theta^A$ correlations are not available. The edge and beam screen cuts for the first station are of course also not available. This means that the acceptance for such an elastic event will

be higher than in the N_4 case. Therefore, an acceptance correction denoted the Elastic Overestimation Factor (EOF) has to be applied to the $n < 4$ events in the formula (10.20):

$$\varepsilon_{\text{reco}} = \frac{N_4 - B_4}{N_4 - B_4 + (N_3 - B_3)\,EOF_3 + (N_2 - B_2)\,EOF_2 + (N_1 - B_1)\,EOF_1 + (N_0 - B_0)\,EOF_0} \tag{10.21}$$

There are different combinations of failing detectors which give the same n and the EOFs must be determined for each combination. The EOFs were introduced in Ref. [11], where it was data driven: For events with tracks in all four detetectors, it was measured how many events passed the N_4 criteria wrt. the number of events passing the available $N_{n<4}$ criteria. In this analysis, the EOFs are found with a simulation of elastic events but using the same procedure. This gives a higher statistical precision on the EOFs, and background events are also not an issue. Instead, the EOFs now depend on the input parameters of the simulation. The simulation is the same as the one used to determine the correlation bands in Section 9.5 and the optics in Section 10.2. The EOFs are t-dependent, and the integrated EOFs over all t-values can be as low as 0.97.

The MD trigger tiles are up to 100 μm closer to the beam than the tracking region, hence events can hit the trigger tiles while being outside the tracking region. This is an acceptance effect and should not be counted in $\varepsilon_{\text{reco}}$, hence the events have to be removed. The effect needs careful treatment especially in this data set where the amount of beam halo protons is large close to the detector edge. Therefore, it is required that at least four U-layers and four V-layers are hit in a failed detector without a track. Otherwise, the absence of a track is considered to be due to the acceptance. The criterion is more strict than in the previous analyses where it was required that the entire detector should have a least five fiber hits. But the five fiber hits can come from a noise burst in one of the MAPMTs, hence the criterion is considered as insufficient. The new criterion is more stable in this regard, and though it is more strict, it can be concluded from Figure 9.3 that the probability to reject an elastic event due to this criterion is negligible.

10.9.2 Background estimation

The background estimation procedure described in Section 9.6 for B_4 is adopted to some of the failed cases. However, the template construction has to be slightly modified as the background shape is not guaranteed to be the same for failed and fully reconstructed events. As an example, consider the case in elastic arm 1 where B7R1L does not have a track which means that one of the B_3's needs to be estimated. An event with tracks and triggers in B7L1U and A7L1U is then randomly combined with an event with triggers in A7R1L and B7R1L but which has only a reconstructed track in A7R1L. One of the $x-\theta_x$ correlations is available for the template scaling in all the topologies where both detectors on the same side of the IP have a track. The background in the remaining topologies are found using probability calculations as described below. The DPE background contribution is safely neglected in the track reconstruction efficiency, as it was shown in Section 9.7 that the contribution is very small.

	Elastic arm 1		Elastic arm 2	
Topology	w/o trigger	w trigger	w/o trigger	w trigger
1234	106483	104204	97167	96101
123	15607	15302	18976	18521
124	7627	7441	8487	8372
134	9303	9109	12067	11923
234	19690	19280	26557	26095
12	60757	56420	109570	75864
34	37224	35092	80616	64287
13	1904	1832	3535	3286
14	666	650	1105	1083
23	2841	2791	5479	5248
24	1774	1705	3826	3466
1	14442	12953	26116	16739
2	20673	19158	55279	37026
3	12665	11669	28075	20596
4	7032	6204	16453	11040
0	65021	49116	115239	51238

Table 10.6: Number of elastic candidates with and without the offline trigger requirement. All available selection criteria have been applied. The topology number reflects the detector stations with a reconstructed track, where B7L1=1, A7L1=2, A7R1=3, and B7R1=4. The 0 topology refers to the case with no reconstructed tracks at all.

Even with an infinitely precise background estimation, the uncertainty on the number of true elastic events would still be

$$\sigma_E = \sqrt{\sigma_N^2 + \sigma_B^2} = \sqrt{N + \sigma_B^2} \geq \sqrt{N} \,. \tag{10.22}$$

In order to improve the precision of $\varepsilon_{\text{reco}}$, one should therefore focus on the reduction of definite non-elastic events before the background estimation. In this way, N will be smaller and hence also the uncertainty.

An important difference to the previous analyses is the introduction of the more strict offline trigger criterion, where all four detectors in an elastic arm are required to have a fired trigger. Table 10.6 shows the number of events passing the elastic selection criteria with and without the offline trigger requirement. The number of fully reconstructed elastic candidates is slightly decreased as expected from the trigger efficiencies of L1_ALFA_ELAST15/18 and L1_ALFA_ELAST11/12 in the previous section. The greatest difference is for the two topologies in elastic arm 2 where two detectors on one side of the IP have a track but not the others. It is expected that the reduction is more pronounced in elastic arm 2 because this is where one of the detectors have the detector edge closer to the beam than the trigger tiles, as described in Section 6.5. There is no reason why the trigger efficiency should depend on the ability to reconstruct a track, hence it must be primarily background events that are removed by the offline trigger criterion. Therefore, the offline trigger criterion reduces the statistical uncertainty on $\varepsilon_{\text{reco}}$.

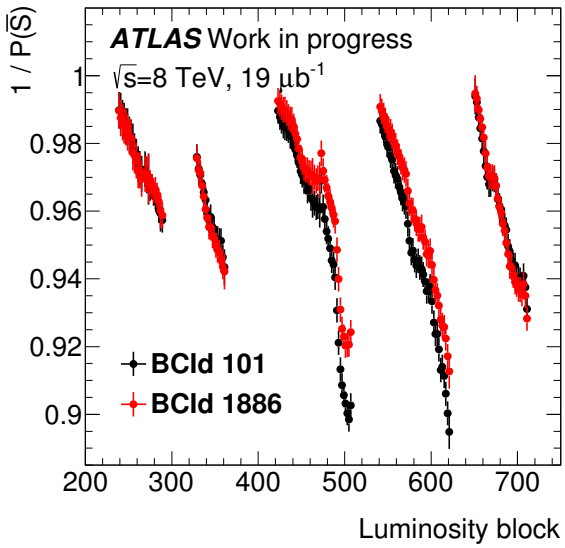

Figure 10.10: The probability to not have a shower as a function of luminosity block for the two colliding bunches, where a shower is defined as both the upper and lower inner detector having at least 200 fiber hits.

10.9.3 Further background suppression

As seen from Table 10.6, there is a large amount of events in the case where both detectors on one side of the IP fail to reconstruct tracks. From the large reduction of this type of events in Table 10.6, it is expected that a large fraction of these events are background. Therefore, a procedure to suppress definite non-elastic events in these topologies before the actual background estimation was used in previous analyses for both ALFA and TOTEM [7]: If both the upper and lower inner detectors on the failed side have a high fiber hit multiplicity, the event is removed from the failed sample, as it is most likely an upstream beam shower unrelated to an elastic event. In addition, a veto on other forward ATLAS sub-detectors have been used to suppress SD events where fragments of the dissociated proton hit ALFA with a shower.

This simple procedure is not valid when the probability of not having a shower in an elastic arm, $P(\bar{S})$, is below 1. If all shower events are rejected, also elastic events in coincidence with a shower will be rejected and the estimated $\varepsilon_{\text{reco}}$ will consequently be too high. The number of failed elastic events obtained with a shower veto must be multiplied by a factor $1/P(\bar{S})$ in order to find the true number of failed elastic events:

$$E_n^{\text{true}} = \frac{E_n^{\text{shower veto}}}{P(\bar{S})} \,. \tag{10.23}$$

Therefore, the author has developed a method to determine $P(\bar{S})$ which allows in principle an arbitrary strict shower definition. Events are selected with the unbiased bunch group trigger, and the fraction of events fulfilling the shower definition is found. The result is shown in Figure 10.10 for a possible shower definition. The probability for not having a shower decreases with time as the beam halo repopulates. It is significantly different

from one, hence the shower veto effect is non-negligible. The difference between the two colliding bunches means that the correction must be done for each bunch separately.

The bunch group trigger was prescaled by a factor 10 to 20 throughout the run which gives non-negligible statistical uncertainties on $P(\bar{S})$. Therefore, it is not straight forward to conclude whether the precision of $\varepsilon_{\text{reco}}$ benefits from a shower veto or not. In a first test, the shower veto did not give a significant improvement on the precision, and further investigations are needed to exploit the full potential of the shower veto. However, it is evident that a shower veto can not be used in this data set without the correction factor of $1/P(\bar{S})$.

10.9.4 Probability calculations of lower topologies

The B_0 is impossible to estimate since no correlation cuts are available for the side-band method, and it is therefore not possible to find E_0. Instead, an approximate calculation of E_0 based on the E_2 topologies was used in the previous analyses. However, it is also difficult to determine the B_1's, and Table 10.6 and the EOF values above 0.97 showed that the contributions from the N_1 topologies are significant. Therefore, the author has developed a procedure where the E_1's and the E_0 are calculated from probabilities of topologies with more tracks. In this way, the uncertain background estimation of the B_0 and B_1's are no longer needed.

The following probability calculations rely on the assumption that the ability to reconstruct a track in an elastic event in the detectors on the A-side is independent of what happens in the detectors on the C-side. The detectors on the A-side are about 500 meters from the detectors on the C-side, and they measure two different protons and in two different beams since the ingoing beam and the outgoing beam are already separated in two beam pipes at the position of the ALFA detectors. Hence, there is no reason why the track reconstruction in the A-side and C-side should be correlated. In contrast, the inner and outer detector on the same side are correlated, which has to be taken into account: A shower developed upstream before the detectors will hit both. Furthermore, a proton could develop a shower in the inner detector giving rise to a failed track reconstruction also in the outer detector.

Let p_{ij} denote the probability to have a track in station i and j. A $\bar{i}$ means that there is no reconstructed track in station i. The relations between the probabilities and the number of elastic events in the different topologies are then:

$$\begin{aligned}
p_{12} \cdot p_{34} \cdot E_{\text{total}} &= E_{1234} \ , \\
p_{12} \cdot p_{3\bar{4}} \cdot E_{\text{total}} &= E_{123\bar{4}} \ , \\
p_{12} \cdot p_{\bar{3}4} \cdot E_{\text{total}} &= E_{12\bar{3}4} \ , \\
p_{1\bar{2}} \cdot p_{34} \cdot E_{\text{total}} &= E_{1\bar{2}34} \ , \\
p_{\bar{1}2} \cdot p_{34} \cdot E_{\text{total}} &= E_{\bar{1}234} \ , \\
p_{12} \cdot p_{\bar{3}\bar{4}} \cdot E_{\text{total}} &= E_{12\bar{3}\bar{4}} \ , \\
p_{\bar{1}\bar{2}} \cdot p_{34} \cdot E_{\text{total}} &= E_{\bar{1}\bar{2}34} \ ,
\end{aligned} \tag{10.24}$$

where E_{total} is the total number of true elastic events inside the detector acceptance, and

$E_{ij\bar{k}\bar{l}}$ is the number of elastic events with no reconstructed track in station k corrected by the EOF. All of these event counts (except of course E_{total}) can be estimated with reasonable precision due to the availability of the $x - \theta_x$ correlation for the background subtraction in either the A-side or the C-side. The relations can therefore be used to calculate all the remaining E's, e.g.

$$E_{1\bar{2}\bar{3}4} = p_{1\bar{2}} \cdot p_{\bar{3}4} \cdot E_{\text{total}} = \frac{E_{1\bar{2}34}}{p_{34} \cdot E_{\text{total}}} \cdot \frac{E_{12\bar{3}4}}{p_{12} \cdot E_{\text{total}}} \cdot E_{\text{total}} = \frac{E_{1\bar{2}34} \cdot E_{12\bar{3}4}}{E_{1234}} \ .$$

These calculated values are then used to find $\varepsilon_{\text{reco}}$ instead of $(N - B) \cdot EOF$.

10.9.5 Extrapolation

Near the detector edge, there is an excess of events where both detectors on one side of the IP fail to reconstruct a track. This is not due to the track reconstruction but to the beam divergence: The reconstructed proton is inside the detector acceptance while the proton on the other side of the IP is outside and instead hits the Roman Pot window about 450 μm from the detector edge. The interaction with the Roman Pot can cause a shower development which spreads to the trigger tiles and gives a signal. Such events should only be treated as an acceptance effect and not in $\varepsilon_{\text{reco}}$. The effect was already observed in the previous analyses, and though it is smaller in this data set due to a smaller beam emittance and the offline trigger criterion, it must still be accounted for.

It was decided to apply a 2 mm edge cut in the determination of the efficiency and then extrapolate to the full detector area. A similar but less transparent extrapolation procedure was used in the previous analyses. The 2 mm edge cut is sufficient to completely remove the beam divergence effect. Furthermore, most of the background events are close to the beam, hence the edge cut reduces the statistical uncertainty on $\varepsilon_{\text{reco}}$.

10.9.6 t-dependence of $\varepsilon_{\text{reco}}$

It is of greatest importance to investigate the t-dependence of $\varepsilon_{\text{reco}}$ in order to perform a correct extrapolation to the detector area closest to the beam. Figure 10.11 shows the elastic track reconstruction efficiency in the full detector area including only those cases where maximum one detector has failed to reconstruct a track. With maximum one missing track, a precise determination of t is still possible, and the divergence effects are negligible. These type of plots were used in the previous analyses to conclude that the full $\varepsilon_{\text{reco}}$ was t-independent. The χ^2/ndf for a constant fit to the data in elastic arm 2 is sufficiently small to assume a t-independent $\varepsilon_{\text{reco}}$, whereas for elastic arm 1 the χ^2/ndf gives a probability of only 0.3 %. The efficiency seems to decrease at small t, which can in fact also be observed for elastic arm 2.

The reason for the low efficiency at small t is not yet understood. The background level is high a small t-values, but the track criteria should in principle ensure a t-independent $\varepsilon_{\text{reco}}$. However, the small t-region is more sensitive to a wrong background estimation. The EOFs give only a slight change in the spectrum, hence a wrong EOF determination is not the solution. The design of the MDs could also provide an explanation: As discussed

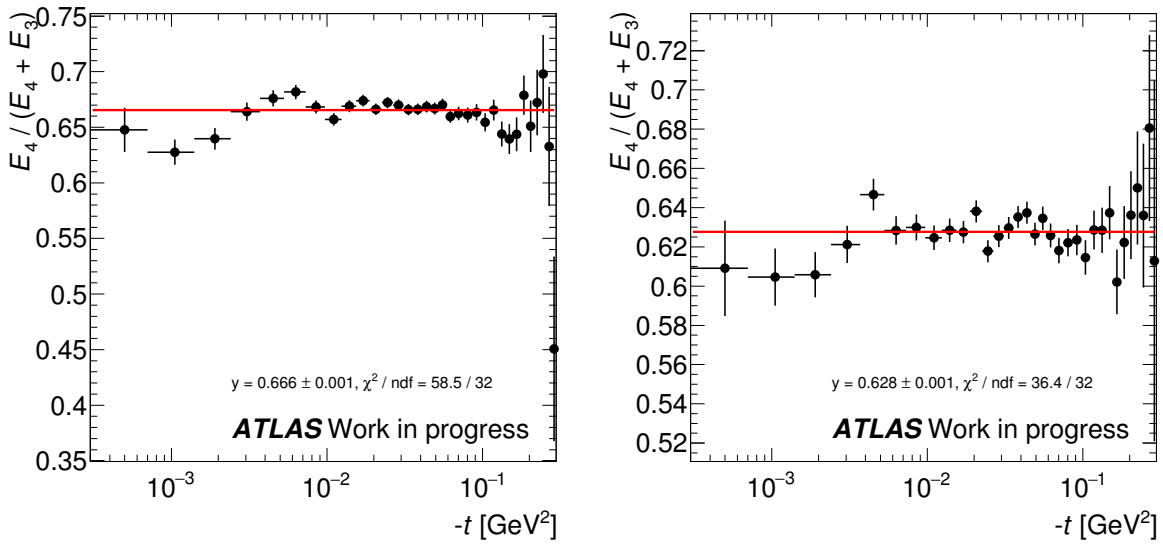

(a) Elastic arm 1. **(b)** Elastic arm 2.

Figure 10.11: Partial elastic track reconstruction efficiency where only events with one failed detector are included. The data is fitted with a constant.

in Section 10.7, it is possible that the positions of the fibers at the detector edge have shifted more from their design position, which give a worse track resolution. If the overlap of fibers between the layers are worse at the detector edge, it could influence the track reconstruction efficiency. More work is required to find the full explanation.

Despite the observed deviations at small t, the efficiency is considered to be constant throughout the analysis.

10.9.7 Stability checks

At the time of writing, the systematic variations have not yet been worked out. The relevant variations are:

- Vary the requirement on the number of U- and V-layers which must be hit for the failed detectors.
- Vary the boundaries for the background subtraction. This should result in variations within the statistical uncertainty on the background scaling if the templates describe the data.
- Vary the boundaries on the elastic selection. If $\varepsilon_{\text{reco}}$ is truly t-independent, this will not change the efficiency beyond statistical fluctuations.
- Vary the 2 mm edge cut used to reject the Roman Pot window effect. When the cut gets too small, the efficiency will decrease since events outside the detector acceptance are included in the failed sample.

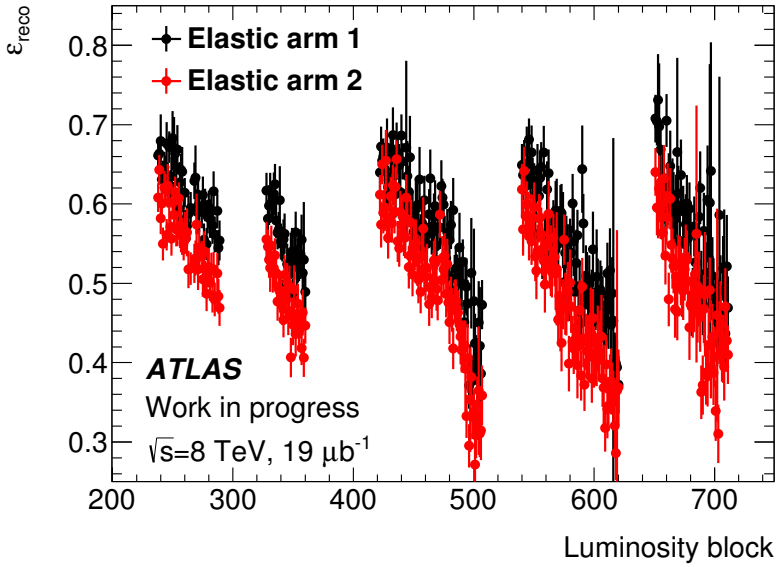

Figure 10.12: Elastic track reconstruction efficiency as a function of luminosity block. The uncertainties are only statistical.

- Vary the track criteria. The total number of elastic events corrected for the efficiency should remain constant.
- Estimate the number of elastic events where one detector on both sides of the IP have failed. These events can be determined reasonably well using a different correlation for the background subtraction and serves as a sanity check of the values from the probability calculations.
- Implement the background suppression for different shower veto definitions.

The difference in $\varepsilon_{\text{reco}}$ for a given variation will be taken as a one standard deviation systematic uncertainty in accordance with the previous analyses. The individual contributions are added in quadrature to obtain the full uncertainty.

10.9.8 Results

Figure 10.12 shows $\varepsilon_{\text{reco}}$ as a function of luminosity block. The efficiency is strongly decreasing as the beam halo repopulates since more shower events are produced and also the amount of multi-track events increases. The decrease in efficiency explains the elastic yield in Figure 9.11.

The final numbers for $\varepsilon_{\text{reco}}$ including systematic uncertainties from the collaborator are pending at the time of writing. Hence, the preliminary values obtained by the author:

$$\varepsilon_{\text{reco}}^{\text{arm 1}} = 0.573 \pm 0.02 \,, \tag{10.25}$$
$$\varepsilon_{\text{reco}}^{\text{arm 2}} = 0.504 \pm 0.02 \,, \tag{10.26}$$

will be used in the remainder of the data analysis. The uncertainties are an educated - but conservative - guess by the author. They are significantly higher than the uncertainties in Ref. [11] of $0.0034 - 0.0045$ due to the lower statistics in this run and the high background level. The uncertainties are assumed to be uncorrelated.

10.10 Reconstruction of four-momentum transfer

The scattering angles are calculated from the ALFA coordinates and then multiplied by the beam energy and squared to obtain the four-momentum transfer. Ignoring the beam divergence, it is clear that the set of Equations (10.3)-(10.8) over-constrains the problem, which gives several possible methods to determine the scattering angle. The traditional methods used in the previous analyses are described in the following, and also a new method developed by the author is presented. Finally, the resolutions of the different methods are investigated.

10.10.1 Traditional t-reconstruction methods

Since an elastic collision gives no tracks in the ATLAS ID, the u^* coordinate is unknown and at least two of the six equations must be used to find the scattering angle. Traditionally, four methods have been used, where the beam divergence is ignored:

Subtraction method

The Equations (10.3) and (10.6) are used to find an expression for θ_u^* based on the measurements in the outer ALFA stations:

$$\begin{aligned}\theta_u^* &= \frac{\frac{M_{11,241}^C}{M_{11,241}^A}u_{241}^A - u_{241}^C}{\frac{M_{11,241}^C}{M_{11,241}^A}M_{12,241}^A + M_{12,241}^C} \\ &\approx \frac{u_{241}^A - u_{241}^C}{M_{12,241}^A + M_{12,241}^C}\ ,\end{aligned} \tag{10.27}$$

where it has been used that M_{11} is approximately the same on the A- and C-side. Likewise, an expression based on the inner ALFA stations can be found and $(\theta_{u,\text{inner}}^* + \theta_{u,\text{outer}}^*)/2$ is then used as the best estimation of θ_u^*. It is clear that large values of the M_{12}'s reduce the uncertainty on θ_u^* from the detector resolution.

Using a simple average is only correct if the two expressions give the same precision in θ^*. Otherwise, the result will be biased towards the less precise measurement. Table 8.1 showed that $M_{12,237}^y \approx M_{12,241}^y$ which gives about the same resolution for θ_y^* in the inner and outer stations and hence justifies the use of an average. In this analysis, the determination of θ_x^* uses only the inner measurements because $M_{12,241}$ is an order of magnitude lower than $M_{12,237}$ giving a much worse resolution, hence the average is not a good estimate. Another option would be to use a weighted average.

Local subtraction

The Equations (10.3) and (10.4) are used to find an expression for θ_u^* based on the measurements on only one side of the IP:

$$\theta^*_{u,S} = \frac{M^S_{11,241} \cdot u^S_{237} - M^S_{11,237} \cdot u^S_{241}}{M^S_{11,241} \cdot M^S_{12,237} - M^S_{11,237} \cdot M^S_{12,241}} \ , \quad S = A, C \ . \tag{10.28}$$

The measurements on the A-side and on the C-side are averaged to give the final estimate of θ_u^*. The difference between the measurements is a measure of the convoluted beam divergence as described in Section 10.3. Again, the uncertainty on θ_u^* due to the detector resolution will be smaller with larger values of the M_{12}'s.

Local angle

The Equations (10.7) and (10.8) are used to find an expression for θ_u^* using the matrix elements from the lower row in Equation (4.7):

$$\begin{aligned} \theta^*_u &= \frac{\frac{M^C_{21}}{M^A_{21}}\theta^A_u - \theta^C_u}{\frac{M^C_{21}}{M^A_{21}}M^A_{22} + M^C_{22}} \\ &\approx \frac{\theta^A_u - \theta^C_u}{M^A_{22} + M^C_{22}} \ . \end{aligned} \tag{10.29}$$

The local angle θ_u is not measured directly in ALFA but since there are no magnets between the inner and outer ALFA stations, the local angle does not change and can be calculated as

$$\theta_u = \left(u_{241} - u_{237}\right)/d \ , \tag{10.30}$$

where d is the distance between the stations. For this method, large values of the M_{22}'s are important.

Lattice method

In the lattice method, the transport matrix in Equation (4.7) is inverted to find an expression for θ^*. In principle, the four ALFA measurements provide four estimates of θ^*, however the values obtained from the outer and inner station on same side of the IP are correlated through the local angle θ_u. In fact, it is easy to show that the expression for the lattice method reduces to the expression for the local subtraction method (see Appendix B), hence the lattice method will not be discussed any further in this analysis.

10.10.2 The χ^2 method

A new method to reconstruct t is invented by the author in order to correctly handle the relative information about θ^* provided by each of the four ALFA stations. Some ALFA stations add more information than others due to the different values of the matrix elements and detector resolution which is here taken into account.

The idea is to minimize a χ^2 function using the RHS of Equations (10.3)-(10.6) as the theoretical predictions. Terms for the vertex position and the beam divergences are also added such that the χ^2 function reads:

$$\begin{aligned}\chi^2 =& \frac{(u^A_{241} - (M^A_{11,241}u^* + M^A_{12,241}(\theta^* + D^A_u)))^2}{(\sigma_{u^A_{241}})^2} \\ &+ \frac{(u^A_{237} - (M^A_{11,237}u^* + M^A_{12,237}(\theta^* + D^A_u)))^2}{(\sigma_{u^A_{237}})^2} \\ &+ \frac{(u^C_{237} - (M^C_{11,237}u^* - M^C_{12,237}(\theta^* + D^C_u)))^2}{(\sigma_{u^C_{237}})^2} \\ &+ \frac{(u^C_{241} - (M^C_{11,241}u^* - M^C_{12,241}(\theta^* + D^C_u)))^2}{(\sigma_{u^C_{241}})^2} \\ &+ \frac{D^{A\,2}_u}{\sigma^2_{D^A_u}} + \frac{D^{C\,2}_u}{\sigma^2_{D^C_u}} + \frac{(u^*)^2}{(\sigma_{u^*})^2} \ ,\end{aligned}$$

where D is the divergence which is different for the two beams. The scattering angle, divergences and the vertex position are the free parameters. In this way, all available information is included in the determination of t which must give the best possible t-resolution. The uncertainties of the divergences and vertex are calculated from the emittance in Section 10.3 and the coordinate uncertainties are taken from Table 10.4.

10.10.3 Resolution of the reconstructed t

The resolution of t on an event-by-event basis is influenced by the detector resolution due to the measured coordinates and by the emittance which gives an initial angle of the protons before collision and a spread in the vertex position. The uncertainty on the optics gives an overall uncertainty of the sample of events as is not considered here. The t-resolution is not the same for the different t-reconstruction methods as shown in the following.

The scattering angle in x and y are reconstructed independently and t is then calculated as

$$t = -p^2(\theta^{*2}_x + \theta^{*2}_y) \ .$$

The resolution of θ^*_x is listed in Table 10.7 where the scattering angle for simulated elastic events have been reconstructed with the different methods. The subtraction method fails completely as expected from the very small value of M_{12} in the outer stations and should not be used to reconstruct t. Naturally, the χ^2 method is the most precise but it

	Detector smearing and emittance	Only emittance	Only detector resolution
Subtraction	19.264	1.014	19.182
Subtraction inner	2.751	0.631	2.679
Local subtraction	3.808	0.623	3.756
Local angle	3.711	0.624	3.659
χ^2 method	2.730	0.620	2.659

Table 10.7: Resolution of θ_x^* for the different reconstruction algorithms. Both the combined and the individual contributions to the resolution are shown. All numbers are in micro meters and the uncertainties on the numbers are less than 0.003 μm.

	Detector smearing and emittance	Only emittance	Only detector resolution
Subtraction	0.473	0.471	0.047
Subtraction inner	0.475	0.471	0.064
Local subtraction	0.473	0.471	0.050
Local angle	5.487	0.473	5.464
χ^2 method	0.457	0.455	0.048

Table 10.8: Resolution of θ_y^* for the different reconstruction algorithms. Both the combined and the individual contributions to the resolution are shown. All numbers are in micro meters and the uncertainties on the numbers are less than 0.003 μm.

outperforms the subtraction method using only the inner stations by less than a percent. This means that the subtraction inner method is almost as good as possible. The local subtraction and the local angle methods perform worst because they both rely on the local angle between the inner and outer station. In this case, the values of the matrix elements make the detector resolution much more important, which is also clear from the resolution with only emittance included. Here, the resolution for all methods (except for subtraction) is identical and small. To improve the θ_x^* resolution in the future, a better optics with larger values of the M_{12}'s and M_{22}'s is therefore needed whereas a smaller emittance will play only a minor role.

Table 10.8 shows the resolutions for θ_y^*. The χ^2 method performs again best with a resolution 3 % lower than the subtraction method. The local angle method is poor due to the small value of M_{22} which makes detector resolution very important. The other methods yield almost identical resolutions which are more than a factor 5 better than for θ_x^*. In contrast to θ_x^*, the emittance is now dominating the resolution, however a better optics in the horizontal plane is still of greatest importance for a more precise t-resolution in future ALFA running.

The resolutions of θ_x^* and θ_y^* are almost independent of the scattering angle[2]. Therefore, the relative resolution of t changes dramatically as can be seen on Figure 10.13 which shows the performance for some of the t-reconstruction algorithms.

[2]The resolution of θ_x^*, θ_y^* improves slightly with increasing θ_y because the detector resolution improves further away from the detector edge.

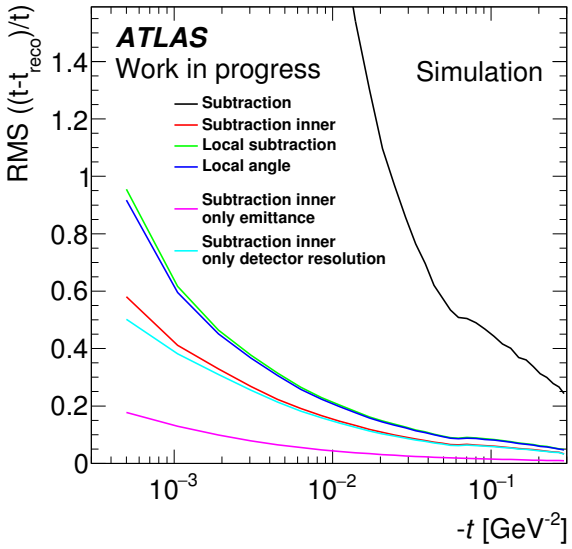

Figure 10.13: The relative resolution of t for different reconstruction algorithms. In all cases, the subtraction method was used for θ_y^* and the name therefore indicates the method used for θ_x^*. The χ^2 method is not shown as it lies almost exactly on top of the subtraction inner method.

The subtraction inner method will be used as the default t-reconstruction algorithm. The χ^2 method is better by less than one percent since the resolution in θ_x^* dominates the t-resolution. However, it is much slower, and speed is important in a later analysis step. Both the local subtraction and the local angle method are useful for systematic studies.

11 | Determination of physics parameters

With the events selected in Chapter 9 and the determination of the experimental effects allowing a reconstruction of the four-momentum transfer, t, in Chapter 10, the final step in the analysis chain is to fit the observed t-spectrum with theoretical predictions for the differential elastic cross section. In this way, models can be investigated and the parameters determined. The acceptance of ALFA as a function of t in Figure 11.1 shows that the data gives access to the CNI region at $-t \lesssim 10^{-3}$ GeV^2. This allows a measurement of the ρ parameter in addition to the total cross section.

The observed t-spectrum in the data is subjected to detector acceptance, efficiencies, resolution, and emittance, hence a theoretical model cannot be directly fitted to the data. In general, there are two options: Either the observed t-spectrum in the data is translated to a differential elastic cross section by a reverse mapping of the detector effects and then compared with a theoretical function. Or the theoretical prediction is translated to an 'observed' t-spectrum by applying the detector effects to a simulation of elastic events and then compared directly with the observed spectrum.

The former option was chosen in the previous elastic ALFA analyses. The exact procedure will be described below including a discussion of the simplifications being made and the possible problems they entail in view of the current data analysis. In order to avoid these simplifications, a new procedure is presented where the latter option is used. The two procedures should in principle give the same result if the simplifications of the former are valid.

11.1 Unfolding procedure

The idea behind the fit procedure used in the previous ALFA analyses is to determine the reverse mapping of the experimental effects discussed in the previous chapters and apply this mapping to the observed t-spectrum. Thereby, one obtains the $\mathrm{d}\sigma_{\mathrm{el}}/\mathrm{d}t$ which would have been observed with a perfect detector with full phase-space coverage, infinitesimal resolution, zero beam emittance, 100 % efficiency and no background.

The effects of limited phase-space coverage and inefficiencies are simply reversed by the multiplication of a (t-dependent) correction factor, and the estimated background is subtracted from the observed t-spectrum. In contrast, the effects of detector resolution and beam emittance are not straightforward to reverse. They give an uncertainty on

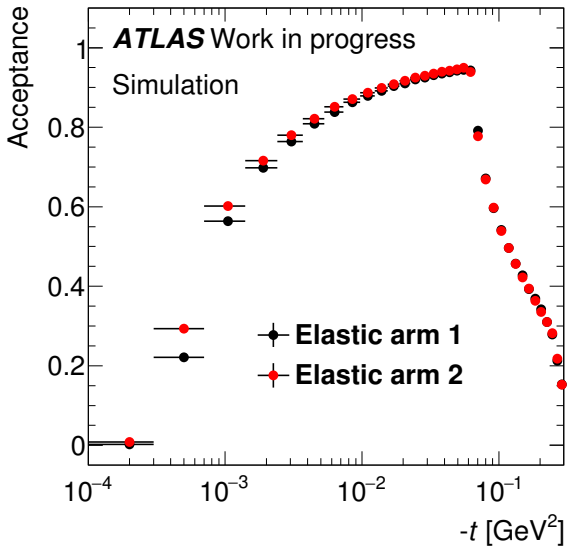

Figure 11.1: The acceptance of ALFA in the two elastic arms as a function of the four-momentum transfer, t. The difference in acceptance between the two arms is due to differences in the detector distances to the beam. Only statistical uncertainties are included, but they are too small to be visible.

the reconstructed four-momentum transfer, and the effect is reversed by *unfolding*. The idea behind unfolding is to apply the resolution and emittance effects to a simulation in order to know how a true value, t_{true}, translates into a reconstructed value, t_{reco}. This translation is written in matrix form as a so-called response matrix. A simplified inversion of the response matrix is applied to the observed t-spectrum which then estimates the spectrum without these effects.

The response matrix using the nominal values for the experimental effects from Chapter 10 is shown in Figure 11.2 for elastic arm 2. The fact that the response matrix has off-diagonal elements means that some events migrate from one bin in the t-spectrum to another. If these migration effects are too large, it will give unstabilities in the inversion of the response matrix. Therefore, the bin sizes for the t-spectrum have been chosen such that about 50 % of the events in each bin do not migrate to another bin.

The fit of a theory to the obtained $\mathrm{d}\sigma_{\text{el}}/\mathrm{d}t$ is performed with a profile minimization procedure [45], where the systematic uncertainties on the corrected $\mathrm{d}\sigma_{\text{el}}/\mathrm{d}t$ coming from the uncertainties on the experimental parameters are taken into account. The fit is performed by a minimization of the following χ^2 function, where the experimental effects are included as nuisance parameters:

$$\chi^2 = \sum_{i,j} \left[\left(D(i) - \left(1 + \sum_{l=1} \alpha_l \right) \times T(i) - \sum_{k=1} \beta_k \times \delta_k(i) \right) \times V^{-1}(i,j) \right.$$
$$\left. \times \left(D(j) - \left(1 + \sum_{l=1} \alpha_l \right) \times T(j) - \sum_{k=1} \beta_k \times \delta_k(j) \right) \right] + \sum_{k=1} \beta_k^2 + \sum_{l=1} \frac{\alpha_l^2}{\epsilon_l^2} \,, \quad (11.1)$$

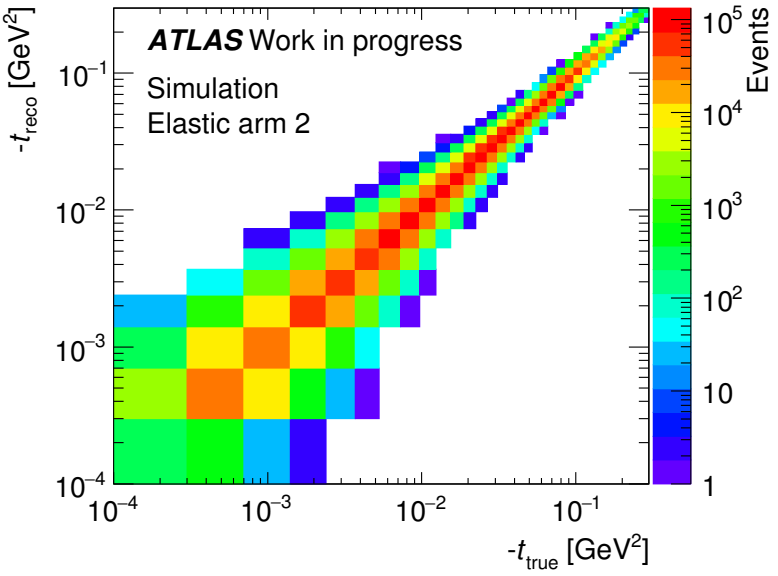

Figure 11.2: The true versus reconstructed four-momentum transfer, t, for elastic arm 2.

where

- $D(i)$ is the differential elastic cross section in bin i after the corrections for all experimental effects;
- $V(i,j)$ is the statistical covariance matrix returned by the unfolding procedure due to the bin-to-bin migrations;
- $T(i)$ is the theoretical prediction in bin i;
- α_l is a nuisance parameter which involves only an overall scaling of $D(i)$, e.g. luminosity;
- ϵ_l is the uncertainty on α_l determined in a subsidiary measurement;
- β_k is a nuisance parameter with a t-dependent effect on $D(i)$;
- $\delta_k(i)$ is the shift in bin i from a $\pm 1\sigma$ change of β_k where the σ has been determined in a subsidiary measurement.

The $\delta_k(i)$ is found by varying the corresponding nuisance parameter with its uncertainty and observe the difference in $\mathrm{d}\sigma_{\mathrm{el}}/\mathrm{d}t$. All other nuisance parameters are fixed to their nominal values. The probability distributions for the nuisance parameters are taken as Gaussians, and the last two terms in the χ^2 are penalty terms.

11.1.1 Limitations

This fitting procedure where unfolding is used to translate data to the theory world is clear and straightforward, however the simplifications impose certain limitations. One of

the primary concerns is the model dependence of the response matrix. The amount of bin-to-bin migration depends on the underlying distribution inside the bins, e.g. events from an exponential decay migrate less to bins at larger values than a flat distribution and more to smaller values. In the previous ALFA analyses, the systematic uncertainty due to the unknown true distribution was addressed by a variation in the nuclear slope parameter, B, and the influence on σ_{tot} was about one per mille. However, for a measurement in the CNI region, the underlying true distribution has more parameters and the functional form is not well known as discussed in Chapter 3. Therefore, it is not clear how to vary the input true distribution in a meaningful way to address the systematics. Furthermore, the effect of the model dependence is expected to be larger in the CNI region due to the more steep rise of $\mathrm{d}\sigma_{\text{el}}/\mathrm{d}t$.

Another limitation of the procedure is the assumption of linearity of the nuisance parameter effects, i.e. that it is parametrized as $\beta_k \times \delta_k$. In general, there is no proof that this is a valid assumption, though for small deviations it is often a good approximation. A better solution would be to make an actual parametrization for β_k.

The last point mentioned here is the assumption that the δ_k's are uncorrelated. In the ALFA analyses this is in general not true. As an example, consider just two nuisance parameters: The beam energy and the distance between the detectors. An increase in the beam energy shifts the events to larger t-values, since it is a multiplicative factor on the scattering angle. The distance on the other hand changes directly the value of the reconstructed vertical scattering angle and thereby also the acceptance. It is clear that if the distance is changed such that the acceptance in the first t-bin vanishes, the change in that bin due to the beam energy will now be different, as an increase in the beam energy can no longer shift events in that bin to other bins. In general, the δ_k's are therefore not independent of the other nuisance parameters, however the size of the effect is not known.

11.2 New fit procedure

The previous fit procedure relies on simplifications which are not guaranteed to be good approximations in the elastic analysis at small t-values. Therefore, it was decided to develop a new procedure, which does not rely on unfolding and the assumption that the change in the t-spectrum due to experimental effects can be expressed as a linear combination.

The new procedure exploits the simple nature of elastic scattering which allows a fast simulation. The idea is simple: The theoretical distribution is translated to the detector world. All the experimental effects are known from the previous chapters and can therefore be applied to simulated elastic events generated from a theoretical probability distribution. The final simulated distribution can now be directly compared to the observed t-spectrum. The t-spectrum in the data and simulation for the two elastic arms are compared with a χ^2 function:

$$\chi^2 = \sum_{\text{arm}=1}^{2} \sum_{\text{bin}} \frac{\left(D_{\text{arm}}^{\text{bin}} - S_{\text{arm}}^{\text{bin}}(\boldsymbol{\beta})\right)^2}{\sigma_{D_{\text{arm}}^{\text{bin}}}^2 + \sigma_{S_{\text{arm}}^{\text{bin}}}^2} + \sum_{l=1}^{N} \beta_l^2 \ , \tag{11.2}$$

where D, S is the bin content in the observed spectrum in the data and simulation, respectively, $\boldsymbol{\beta}$ is the list of nuisance parameters with zero as the nominal value, and N is the total number of nuisance parameters. In the formula, it has been used that the event yields in the data bins are large enough to assume Gaussian uncertainties. The uncertainties for the nuisance parameters are normalized to 1 and the probability distributions are assumed Gaussian. Only the physics parameters in the theoretical prediction and the nuisance parameters in the simulation are varied to minimize the χ^2; the observed t-spectrum in the data remains the same throughout the minimization procedure. A new simulation is made for each new set of physics and nuisance parameters, hence no assumptions on the effects of the parameters are needed. Instead, the true effects are used in each step of the minimization.

The details of the simulation, the actual procedure to find the minimum of the χ^2, and the way to extract the uncertainties on the physics parameters are given below.

11.2.1 Simulation details

The elastic events are generated from a theoretical probability distribution of $\mathrm{d}\sigma_{\mathrm{el}}/\mathrm{d}t$ with a given set of physics parameters. The collision point is taken from a 2D Gaussian distribution with the widths calculated from the vertical and horizontal emittances of the two beams, Equation (10.9). The t-value and azimuth angle, ϕ, of an event are translated to the horizontal and vertical scattering angles using

$$\theta_x^* = \cos\phi \cdot \sqrt{-t}/E_{\mathrm{beam}} \ , \tag{11.3}$$

$$\theta_y^* = \sin\phi \cdot \sqrt{-t}/E_{\mathrm{beam}} \ , \tag{11.4}$$

with $\theta_A^* = -\theta_C^*$. Contributions from the beam divergence are added to the scattering angles[1]. The beam divergence is calculated from the emittance using Equation (4.10) and is different for the two beams and for the vertical and horizontal directions.

The scattering angles of the two protons are now translated to the transverse positions at the ALFA detectors using the transport matrix elements. A total of four magnet currents for each beam are used to calculate the corrections of the transport matrix elements from the design values as described in Section 10.2.

A set of horizontal offsets, rotations, and vertical alignment parameters are used to perform a reversed alignment where the proton coordinates in the beam coordinate system is converted to the individual coordinate systems of the detectors. A Principal Component Analysis is performed on the eight correlated vertical alignment parameters in order to obtain eight uncorrelated nuisance parameters. The resolutions of the detectors are simulated by Gaussian smearings of the coordinates. The widths of the Gaussian distributions are calculated from the slopes and intercepts describing the y-dependent convoluted resolution of the four inner-outer detector pairs and the ratios between the inner and outer detectors.

[1]To be exact, the beam divergence should have been added to the protons *before* the scattering process. Fortunately, the angles are so small that the effect is negligible and this more simple way is sufficient.

The last part of the simulation is the overall normalization. The events are weighted with the luminosity to translate the cross section into an event rate, and also the trigger and tracking efficiencies for the two elastic arms are applied.

All the inputs to the simulation are treated as nuisance parameters with a penalty term in the χ^2 except for the physics parameters in the theoretical model which are free. The values of the nuisance parameters and their uncertainties were estimated in Chapter 10. In total, the fit includes 49 nuisance parameters.

The t-distribution for the simulated events are now reconstructed like the data with the exact same settings for the edge and beam screen cuts, the alignment constants, the correlation cuts, the transport matrix elements, and the beam energy. No floating parameters are used in this step. The background t-spectra for the two arms estimated in Chapter 9 are added to the simulation with a nuisance parameter for the normalization, and the similarity between the simulated t-spectrum and the observed t-spectrum is quantified with the χ^2 function (11.2).

11.2.2 Minimization procedure

The χ^2 in Equation (11.2) is a function of the physics parameters of a given theoretical model and all the 49 nuisance parameters. The minimization is performed with the MINUIT Migrad algorithm [46], which uses numerically calculated first derivatives of the χ^2 to predict the minimum. In principle, MINUIT can handle an arbitrary number of parameters, "*however the technological limitations of* MINUIT *can be seen around a maximum of 15 free parameters at a time*" [46]. Therefore, a stepwise controlled descent towards the minimum is used, where the minimization is performed in iterations fitting only a subset of parameters at a time.

Some nuisance parameters need careful treatment, since they cause bin-to-bin migration of events in the t-spectrum. This migration was already discussed above for the unfolding procedure. One example is the horizontal alignment of the detectors which shift the reconstructed horizontal scattering angle. The migration from one bin to another is discontinuous as a function of the alignment parameter. At a certain value, an event will change bin, hence with a finite number of simulated events it gives statistical fluctuations in the χ^2 function. Figure 11.3 shows the χ^2 value as a function of one of the alignment parameters for two different MC sample sizes. The fluctuations clearly decrease with increasing statistics as expected, since the relative change in bin contents of the simulation caused by a sudden migration of an event from one bin to another is not as large. Such fluctuations will confuse any minimization algorithm which uses first derivatives and must be avoided. One solution is to increase the MC statistics, but the fluctuations are present even with a 100 times more statistics than in the data. The size of the fluctuations roughly follows a $\sqrt{N}$ law, whereas the CPU time scales with N. Therefore, another procedure is chosen where a second order polynomial is fitted to the points, and the minimum determines the best value of the nuisance parameter used in the next steps of the minimization. This gives control over the statistical fluctuations in each minimization step. The fluctuations are of course also present in the previous fit procedure using unfolding, but they will never be directly observed since only three

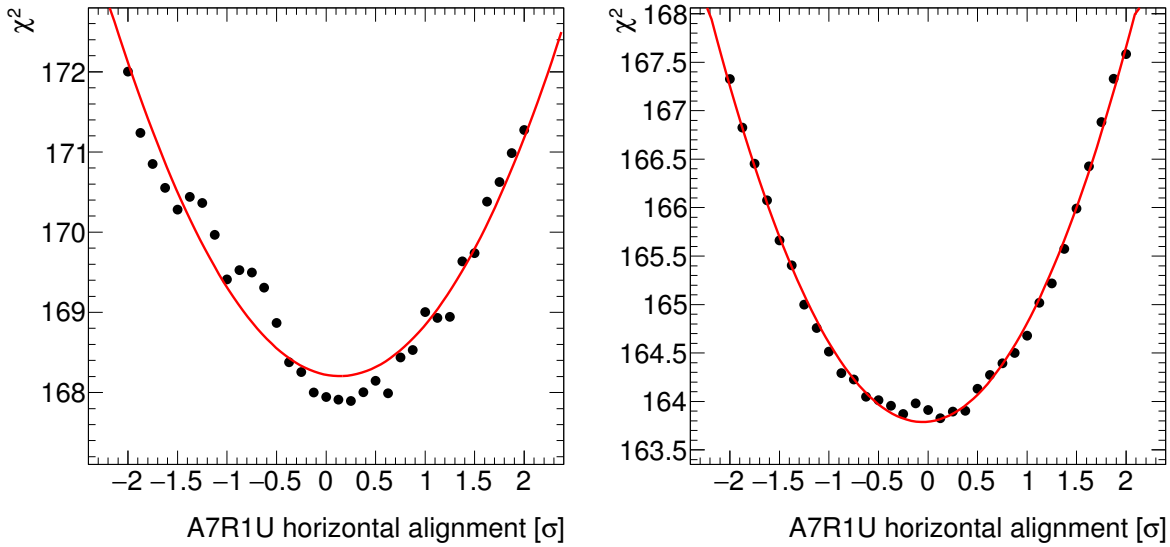

Figure 11.3: The χ^2 quantifying the similarity between the data and simulation as a function of the horizontal alignment in detector A7R1U measured in standard deviations from the nominal value. The MC sample size in the left (right) figure is 10 (100) times larger than in the data. A second order polynomial fit is also shown.

points are used to determine $\delta_k(i)$. The size of the effect is therefore unknown but must be larger due to the use of only three points. The MC statistics has been chosen to be about 30 times larger than in the data. This gives a reasonable compromise between the fluctuations caused by bin-to-bin migration and CPU time.

The detailed minimization procedure is as follows:

1 Make a simultaneous fit of all the physics parameters and the nuisance parameters without bin-to-bin migration effects. All other nuisance parameters are fixed. Fix the free parameters to the values of the fit result.

2 One at a time, make a scan of the nuisance parameters with bin-to-bin migration effects, fit a second order polynomial, and fix the nuisance parameter value to the minimum of the polynomial.

3 Repeat step 1 and step 2 with the updated parameter values until none of the nuisance parameters have changed by more than 10 % from the previous iteration, i.e. until the uncertainty on the uncertainty is less than 10 %.

The convergence criterion of a change less than 10 % in the nuisance parameters ensures that the fit converges in the order of hours. The minimization is performed several times with different initial values of the nuisance parameters. The results are nearly indistinguishable which proves that the convergence criterion has only a negligible effect on the estimation of the physics parameters.

The bin sizes of the t-spectra in the data and simulation are chosen in the same way as in the previous analyses. About 50 % of the events in each bin do not migrate to other

bins, which reduces the fluctuations in the χ^2. Furthermore, it gives the opportunity to unfold the t-spectrum in order to obtain the differential elastic cross section once the values of the physics and nuisance parameters have been determined.

The lower limit on the fit range is chosen to be $3 \cdot 10^{-4}$ GeV^2 since the acceptance in the first bin in Figure 11.1 is essentially zero. The upper limit is set to 0.2 GeV^2. This gives an acceptance above 20 % and is also consistent with the upper limit in the TOTEM analysis [2].

11.2.3 Uncertainty estimation

The fix-release procedure of the parameters in the fit means that the parameter uncertainties returned by MINUIT are not correct. The true uncertainty for a given parameter must be found with all other parameters floating. The procedure is as follows: Take 10 values of the given parameter in a guesstimated 2σ range around the global minimum. For each value, find the minimum by fitting all the other parameters and fill the χ^2 value in a histogram. Fit the histogram with a second order polynomial where all bins have a weight of 1. The values where the polynomial has increased by 1 gives the uncertainty band. Since this is a rather lengthy procedure, it will only be performed for the parameters of interest.

12 | Results

This chapter presents the results of fits to the observed t-spectrum. The first section is devoted to the investigation of different phenomenological models. The uncertainties on σ_{tot} and ρ are thoroughly investigated in the second section, followed by a discussion of the nuisance parameters. Two tests are made at the end of the chapter to find the stability of the fit results.

12.1 Model investigation

As described in Part I, perturbative QCD can not be used to describe forward elastic scattering and there exist several different phenomenological models aiming to describe the data. To gain further knowledge about the true nature of elastic scattering, the free parameters of the models must be fitted to the data, and a model can potentially be excluded if it cannot describe the data.

Only different parametrizations of the nuclear modulus will be investigated in the following. The sensitivity to the proton form factor is very small and does not allow a test of the different parametrizations, hence the standard dipole approximation will be used. The sensitivity to the interference phase is also small. For simplicity reasons, the West-Yennie formula is used, though it is formally inconsistent with a non-exponential parametrization of the nuclear modulus. The argument of the nuclear amplitude is chosen to be constant. It has been shown [2] that this functional form gives fit results indistinguishable to several other models.

Four different parametrizations for the nuclear modulus will be investigated. One option is to use a polynomial in the exponent:

$$F_N(t) \propto e^{-0.5\sum_{i=1}^{n} B_i |t|^i} , \tag{12.1}$$

which is very generic. A first order polynomial will be tried since this is the traditional approach, Section 3.2.2. However, a first order polynomial is only expected to be a good approximation at small t, hence the fit has been performed in the nominal t-range of $3 \cdot 10^{-4}$ GeV$^2 \leq -t \leq 0.2$ GeV^2 but also in a smaller t-range with an upper limit of $-t = 0.1$ GeV^2 in accordance with Ref. [11]. Second and third degree polynomials will also be investigated. They were considered in Ref. [7] and [2] and gave reasonable descriptions of the data. The last parametrization investigated here is the model from Ref. [47] where hadron spin non-flip amplitudes are considered and the exponent is written as:

$$F_N(t) \propto e^{-B_1|t|/2 + B_2/2(\sqrt{4\mu^2+|t|}-2\mu)} , \quad \mu = 135 \text{ MeV} . \tag{12.2}$$

	pol1 ($-t \leq 0.1$ GeV^2)	pol1	pol2	pol3	Spin-flip
χ^2/ndf	32.8/41	47.5/53	40.1/52	39.6/51	40.8/52
Probability (%)	81.6	68.8	88.6	87.7	87.0
σ_{tot} (mb)	99.1 ±1.5	99.2 ±1.5	99.1 ±1.5	99.1 ±1.5	99.2 ±1.5
ρ	0.155 ±0.021	0.142 ±0.020	0.166 ±0.022	0.160 ±0.024	0.172 ±0.023
B_1 (GeV)$^{-2}$	21.08 ±0.12	21.05 ±0.08	21.59 ±0.24	21.33 ±0.54	17.35 ±0.93
B_2 (GeV)$^{-4}$	—	—	-6.1 ±1.6	-1.8 ±8.0	—
B_2 (GeV)$^{-1}$	—	—	—	—	-2.5 ±0.7
B_3 (GeV)$^{-6}$	—	—	—	-17.6 ±33.1	—

Table 12.1: Fit results for different parametrizations of the nuclear modulus. The uncertainties only include statistics and the systematics from background, efficiencies and luminosity.

This model was also investigated in the previous elastic ALFA analyses [32, 11].

The fits are performed with only a subset of the nuisance parameters. The horizontal offsets and rotations of the detectors are fixed to their nominal values as well as the nuisance parameters describing the detector resolution and the six smallest principal components of the vertical alignment. It will be shown below that these parameters have a negligible influence on the fit. The other nuisance parameters are floating but for simplicity the uncertainties on the parameters of interest include only the contributions from background, efficiencies and luminosity and are hence underestimated.

The results are shown in Table 12.1. The χ^2/ndf is smaller than one for all the five cases, even for the first order polynomial in the full fit range up to $|t| < 0.2$ GeV^2. Therefore, it is impossible to exclude any of the models based on this data set. The inconsistent choice of the West-Yennie formula used with the non-exponential slopes does not change this conclusion. The fitted magnet currents and beam energy deviate more from their nominal values for the first order polynomial than for the other parametrizations, but none of the values are more than 1.1 standard deviations from the nominal. Even when only the background and efficiency nuisance parameters are included, and the precision of the efficiency is reduced to the precision obtained in Ref. [11], the fit for the first order polynomial in the full range returns χ^2/ndf = 68.8/53 giving a probability above 7 %. It can therefore be concluded that the inability to exclude some of the models primarily comes from the lack of statistics and not too large systematic uncertainties.

The second order polynomial will be used as the default parametrization in the following. Though the first order polynomial can not be excluded with this data set, it has previously been excluded by the TOTEM collaboration [7]. Furthermore, the greater values of some of the nuisance parameters give a weak sign of tension in the fit since the

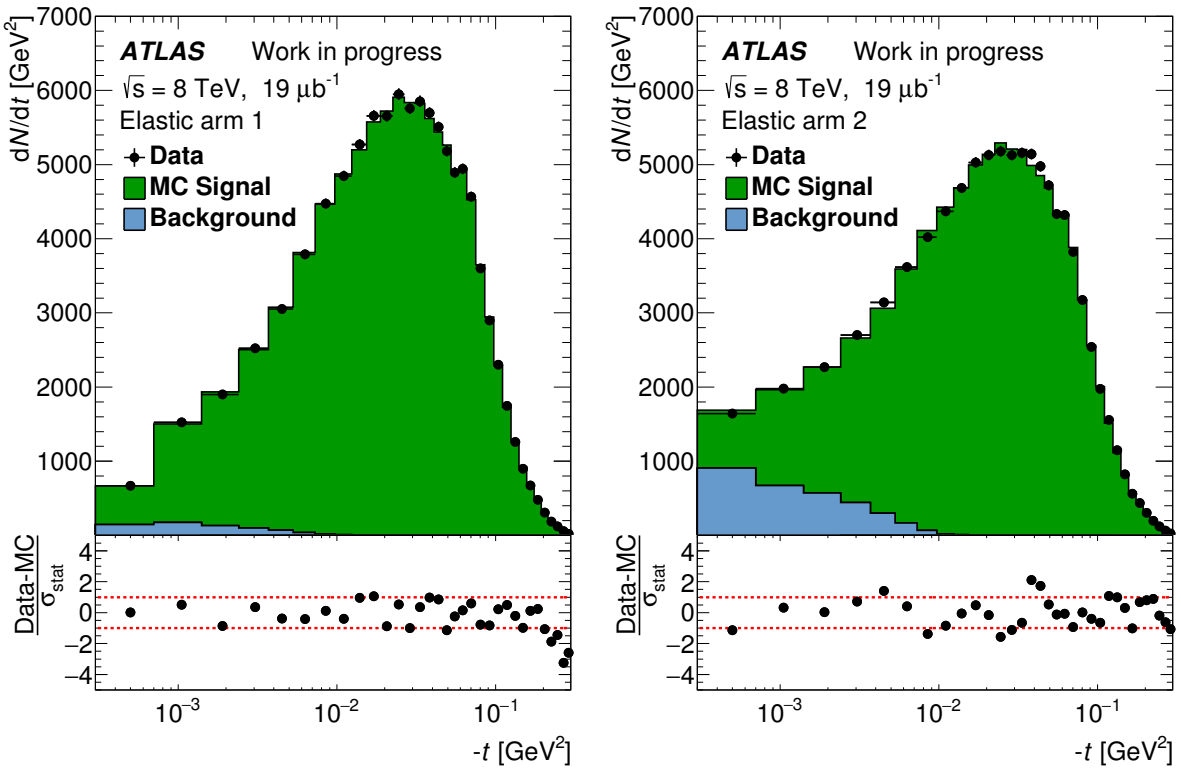

Figure 12.1: Comparison of the t-spectra in the data and simulation. A second order polynomial is used for the nuclear modulus.

physics parameters are not sufficient to describe the data. The third degree polynomial gives negligible differences to the second order polynomial concerning both the quality of the fit and the values of σ_{tot} and ρ. Furthermore, the value of the B_3 parameter is consistent with zero within the uncertainty. The spin-flip model will be used to address the systematic uncertainty on the σ_{tot} and ρ parameters due to the choice of theoretical model.

The comparison between the observed and simulated t-spectrum is shown in Figure 12.1 and similar figures for the other models can be found in Appendix C. Outside the fit range, the residuals for elastic arm 1 become negative which could be an indication that the second order polynomial is not appropriate at such high t-values.

12.2 Uncertainties on σ_{tot} and ρ

The procedure to find the uncertainties on the physics parameters was outlined in Section 11.2.3 and is a lengthy procedure. Therefore, only the full uncertainties on σ_{tot} and ρ will be carried out. The total cross section is used as an input parameter for simulations of other pp processes, and ρ has predictive power for σ_{tot} at higher energies through dispersion relations. These two parameters are therefore important outside the scope of elastic scattering. In contrast, the functional form of the nuclear modulus is unknown,

and different parametrizations are able to describe the data, hence those parameters are not of immediate relevance.

The full uncertainties on σ_{tot} and ρ using the second order polynomial parametrization are shown in Table 12.2. The table also includes the uncertainty contributions from individual nuisance parameters. They are calculated from the full uncertainty and the uncertainty obtained when the given nuisance parameter is fixed:

$$\sigma_{\text{parameter}} \equiv \sqrt{\sigma^2_{\text{full}} - \sigma^2_{\text{fixed parameter}}} \,. \tag{12.3}$$

This definition of individual uncertainty contributions does not take correlations into account, hence the full uncertainty is not the squared sum of all the contributions. However, it allows an overview of the most dominating parameters. The difference wrt. the spin-flip model in Table 12.1 should be added in quadrature as a systematic uncertainty due to the choice of parametrization.

The statistical uncertainty for σ_{tot} is small, whereas for ρ it has a dominating contribution. The sensitivity to ρ is restricted to the CNI region at $-t \lesssim 10^{-3}$ GeV^2 and hence only maximum three bins contribute to the fit of ρ. Furthermore, ρ depends on the relative difference between the bins, whereas σ_{tot} mostly depends on the overall normalization.

The uncertainties on the luminosity measurement and the efficiencies give the largest contribution to the total uncertainty for σ_{tot}. The contribution from Coulomb scattering is not large enough to restrict the normalization, hence the normalization of the t-spectrum is almost strictly proportional to σ^2_{tot}, see Equation (3.18). Therefore, a miscalibration in the luminosity and/or efficiencies can be directly compensated by a change of σ_{tot}.

The uncertainty on the background level has a great effect on the precision of ρ which is exactly as expected since the background peaks in the CNI region. It is questionable

	Uncertainty	
	σ_{tot}	ρ
Full	1.6	0.024
Statistical	0.3	0.017
Luminosity	0.9	0.004
Background	0.1	0.013
Efficiencies	1.2	0.008
Beam energy	0.7	0.007
Emittance	0.4	0.009
Optics	0.5	0.004
1. vertical component	0.0	0.006
2. vertical component	0.3	0.003
Detector resolution, horizontal offset, rotation, vertical components 3-8	0.1	0.003

Table 12.2: Uncertainty estimates for σ_{tot} and ρ when a second order polynomial is used for the modulus of the nuclear amplitude. In addition, some of the individual uncertainty contributions are shown. Model dependent uncertainties are not included.

whether the precision of the background estimate can be further improved in the future. Therefore, the focus should be to reduce the background level in the data taking such that the uncertainty on the background determination will have a smaller effect.

12.3 Nuisance parameter fit results

The fit results of the nuisance parameters are shown in Table 12.3. The nominal value is zero, and the parameters are normalized to one standard deviation. The uncertainties for the parameters are also shown, however these are obtained when all the other nuisance and physics parameters are fixed and are therefore not the global uncertainties.

Out of all the nuisance parameters, only the first principal component of the vertical alignment is off by more than one nominal standard deviation, i.e. the parameter uncertainty provided as input to the fit. This first component is closely related to the vertical offsets of the detectors, and the deviation from the nominal value is understood as a consequence of the efficiency dependence on the vertical offset as explained in Section 10.6.3: The alignment has been performed with preliminary results for the elastic track reconstruction efficiency, and the rather large value of the vertical offset indicates that the efficiency input to the alignment is slightly off. The uncertainty for the first vertical component is well below one, which means that the fit to the t-spectrum is able to constrain this parameter further.

The horizontal offsets and rotations of the outer detectors are essentially zero and the uncertainty is one, meaning that the sensitivity from the t-spectrum to these parameters is completely negligible. This is as expected since the horizontal coordinates in the outer detectors are not used for the t-reconstruction due to the optics. The horizontal offsets and rotations in the inner stations are only slightly changed, which means that the precision of the alignment procedure is sufficient. The six smallest principal components of the vertical alignment can also be ignored. The reason is the very strong vertical correlations between the stations originating from the small emittance in this data set. This means that basically one vertical offset parameter and one distance parameter combining all four detector stations are sufficient for the fit to the t-spectrum.

Though the dominant uncertainty contribution to the reconstructed t-value comes from the detector resolution (Section 10.10.3), the nuisance parameters for the resolution are very close to zero and the uncertainties are basically one. The influence of the uncertainty on t is reduced by the choice of bin sizes in the t-spectrum, hence it is expected that a smaller bin size would result in a greater sensitivity to the detector resolution.

The luminosity and the efficiencies have moved only slightly as expected from the discussion of Table 12.2 since it can be largely compensated by a change in σ_{tot}. The uncertainties returned by the fit are small, however they increase to almost 1 when the physics parameters are released. Therefore, a greater amount of events in the Coulomb region is needed if the t-spectrum should be used to determine the normalization and thereby the luminosity.

The values for the magnet currents are all below 0.5 which means that either the design optics is close to the true optics or that a deviation in the optics can be absorbed

	Value	Uncertainty
Luminosity	0.11	0.15
Arm 1 efficiency	0.12	0.09
Arm 2 efficiency	0.14	0.08
Arm 1 background	-0.02	0.92
Arm 2 background	-0.43	0.44
Beam energy	-0.50	0.25
Horizontal emittance beam 1	-0.10	0.73
Horizontal emittance beam 2	-0.16	0.92
Vertical emittance beam 1	0.18	0.79
Vertical emittance beam 2	0.29	0.67
kQ1Q3 beam 1	-0.24	0.40
kQ1Q3 beam 2	-0.28	0.42
kQ2 beam 1	0.15	0.60
kQ2 beam 2	0.20	0.64
kQ5 beam 1	-0.24	0.24
kQ5 beam 2	-0.49	0.24
kQ6 beam 1	-0.04	0.99
kQ6 beam 2	0.04	0.99
Vertical alignment - 1. component	1.27	0.38
Vertical alignment - 2. component	-0.17	0.88
Vertical alignment - 3. component	0.00	1.00
Vertical alignment - 4. component	0.01	1.00
Vertical alignment - 5. component	-0.01	1.00
Vertical alignment - 6. component	0.01	1.01
Vertical alignment - 7. component	0.02	1.00
Vertical alignment - 8. component	0.00	1.00
Horizontal offset - B7L1U	0.00	1.00
Horizontal offset - B7L1L	0.01	1.00
Horizontal offset - A7L1U	-0.13	0.84
Horizontal offset - A7L1L	-0.04	0.97
Horizontal offset - A7R1U	0.13	0.84
Horizontal offset - A7R1L	0.07	1.00
Horizontal offset - B7R1U	-0.01	1.00
Horizontal offset - B7R1L	0.00	1.00
Rotation - B7L1U	0.00	1.00
Rotation - B7L1L	0.00	1.00
Rotation - A7L1U	-0.16	0.82
Rotation - A7L1L	0.03	1.05
Rotation - A7R1U	0.03	1.04
Rotation - A7R1L	-0.16	0.81
Rotation - B7R1U	-0.01	1.00
Rotation - B7R1L	0.00	1.00
Resolution slope B7L1U-A7L1U	0.00	1.00

	Value	Uncertainty
Resolution slope B7L1L-A7L1L	-0.02	1.00
Resolution slope B7R1U-A7R1U	0.01	1.01
Resolution slope B7R1L-A7R1L	0.00	1.01
Resolution intercept B7L1U-A7L1U	0.02	1.02
Resolution intercept B7L1L-A7L1L	0.03	1.01
Resolution intercept B7R1U-A7R1U	0.03	1.04
Resolution intercept B7R1L-A7R1L	0.03	1.00
Resolution ratio B7L1U-A7L1U	0.00	0.97
Resolution ratio B7L1L-A7L1L	-0.15	0.97
Resolution ratio B7R1U-A7R1U	-0.08	0.94
Resolution ratio B7R1L-A7R1L	0.11	0.81

Table 12.3: Fit results for the nuisance parameters and the approximate uncertainties. The input values are zero with uncertainties of one.

by other parameters. This will become clear when the effective optics determination is made. The values are greatest and the uncertainties smallest for the Q5 magnets, hence these are likely to be the best candidates to be adjusted in the optics determination. It is important to note that the true optics determination is better suited to restrict the magnet currents since it uses the correlations between the measured coordinates and not just the t-value.

None of the nuisance parameters have values further than 1.1 standard deviation from the nominal input value. Therefore, it can be concluded that the physics parameters to a large extend provide enough flexibility in the fit to describe the data. It also justifies the simplified approach used in Section 12.1 where many nuisance parameters where fixed at their nominal value.

12.4 Stability tests

In the standard procedure, the two elastic arms are fitted simultaneously and hence share the same values of the physics and nuisance parameters. In order to perform a stability test of the fit, the two elastic arms are fitted individually. Any differences between the fit results in the two arms indicate that some of the experimental effects are not properly understood.

The results for the physics parameters and the quality of the fits are shown in Table 12.4 along with the results for the full fit procedure and an additional stability test discussed below. The quality of the fits are for both arms very good. The physics parameters are in good agreement within the (underestimated) uncertainties, hence the stability of the fit results across the two elastic arms are good. In particular, it is interesting to see that the two arms yield essentially the same behavior of the nuclear modulus. The uncertainty on ρ is greater in elastic arm 2 because of the higher background level. Figure 12.2 shows the comparison between the observed t-spectrum and simulation for both fits. There is essentially no improvement in the residuals compared to the simultaneous

	Full fit	Elastic arm 1	Elastic arm 2	Unfolding
χ^2/ndf	40.1/52	14.2/24	26.5/24	19.1/24
Probability (%)	88.6	94.2	32.8	74.9
σ_{tot} (mb)	99.1	98.4	99.4	99.1
	±1.5	±1.9	±2.1	±0.3
ρ	0.166	0.172	0.142	0.161
	±0.022	±0.026	±0.045	±0.019
B_1 $(\text{GeV})^{-2}$	21.6	21.7	21.3	21.5
	±0.2	±0.3	±0.4	±0.3
B_2 $(\text{GeV})^{-4}$	-6.1	-6.1	-6.2	-5.9
	±1.6	±2.2	±2.3	±1.8

Table 12.4: Fit results for different stability tests. The parameter uncertainties only include statistics and the systematics from background, efficiencies and luminosity.

fit of the two arms in Figure 12.1. It can be concluded that this stability test show no significant tension between the two elastic arms.

Another stability test is a fit to the unfolded spectrum. It was argued in Section 11.1.1 that the unfolding procedure has some limitations when it is used to perform the actual fit and determination of physics and nuisance parameters. However, when the parameters have been determined using the procedure outlined in Section 11.2, an unfolding can be performed with the given set of fitted parameters, and the theoretical function can be fitted to the unfolded distribution. If the description of the data in the simulation is correct, the fit results should be consistent with the original fit.

The results for the parameters are shown in Table 12.4 and the fit is shown in Figure 12.3. The best fit values from Table 12.3 are used to perform the unfolding, background subtraction, acceptance correction, and the scaling from luminosity and efficiency. The RooUnfoldBayes algorithm [48] has been used for the unfolding with the default regularization parameter of 4. No other unfolding algorithms are tried since this is only a stability test. For simplicity, the statistical correlations between the bins have not been included in the fit. The fit results including the two parameters for the nuclear modulus are in good agreement with the results from the full fledged fit.

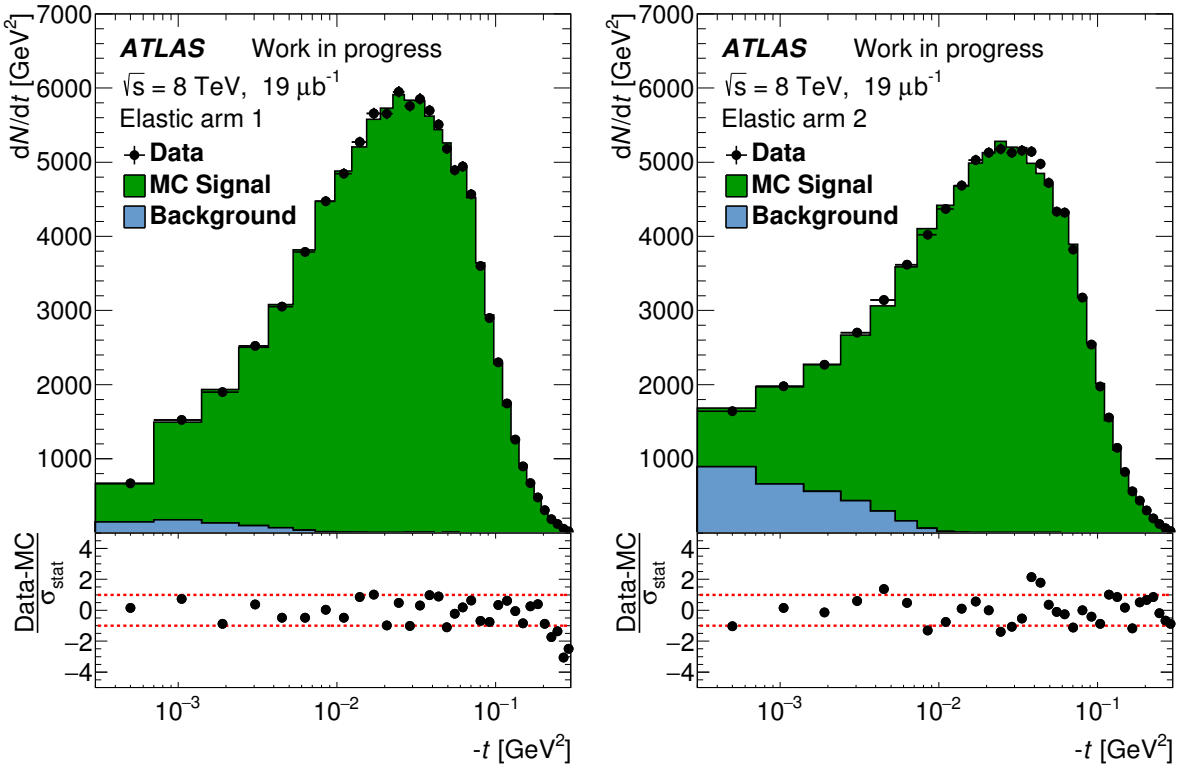

Figure 12.2: Comparison between the data and simulation for separate fits to the two elastic arms.

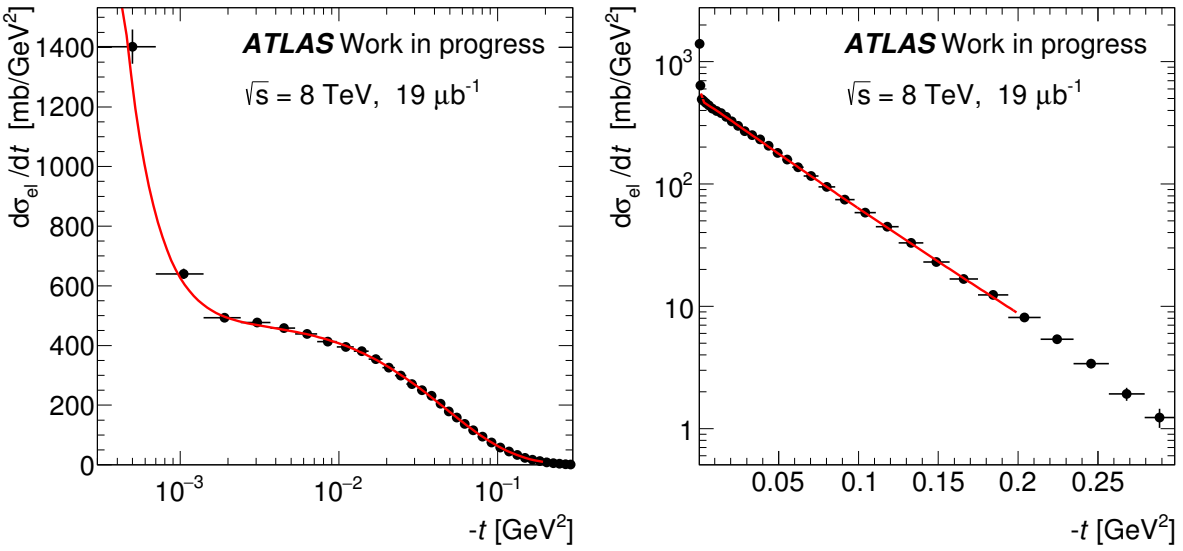

Figure 12.3: Fit to the differential elastic cross section. The values from Table 12.3 are used to unfold the observed t-spectrum. Only statistical uncertainties are included. The two plots are identical but with different scales on the axis.

13 | Discussion

The results for the total cross section and the ρ parameter from the previous chapter are:

$$\sigma_{\text{tot}} = 99.1 \pm 0.3 \text{ (stat.)} \pm 1.6 \text{ (syst.) mb} ,$$
$$\rho = 0.166 \pm 0.017 \text{ (stat.)} \pm 0.019 \text{ (syst.)} .$$

The results are preliminary since the final numbers for the elastic track reconstruction efficiency and the effective optics are not yet available.

This chapter presents a comparison with previous measurements. It will also be discussed what can be improved to obtain a better precision in the future. The chapter ends with an outlook at the $\beta^* = 2.5$ km run in September 2016, where the experience from the data analysis in this thesis was used to obtain the best possible running conditions to fulfill the ultimate goal of ALFA.

13.1 Comparison with other measurements

Results for the total cross section and the ρ parameter at $\sqrt{s} = 8$ TeV have previously been published by the TOTEM Collaboration, where the same LHC setup was used as in this analysis. The results from TOTEM are [2]:

$$\sigma_{\text{tot}}^{\text{TOTEM}} = 102.9 \pm 2.3 \text{ mb} ,$$
$$\rho^{\text{TOTEM}} = 0.12 \pm 0.03 .$$

In addition, the total cross section was measured by the ATLAS Collaboration at $\sqrt{s} = 8$ TeV using a $\beta^* = 90$ m optics [11]:

$$\sigma_{\text{tot}}^{\text{ATLAS}} = 96.07 \pm 0.92 \text{ mb} .$$

The data set was not sensitive to CNI, but the CNI contribution was included in the fit with a fixed $\rho = 0.1362$. The result for σ_{tot} can therefore be compared with the $\beta^* = 1$ km results.

The σ_{tot} found in this analysis agrees with both the TOTEM measurement and the $\beta^* = 90$ m ATLAS measurement. The differences correspond to 1.4 and 1.6 standard deviations, respectively. Moreover, the σ_{tot} in this analysis is close to the average of the two previous measurements. The uncertainty of 1.6 mb is higher than in the previous ATLAS result mainly due to the poor precision of the elastic track reconstruction efficiency. TOTEM uses a luminosity independent procedure where instead the inelastic

rate is measured. This gives a larger uncertainty on the normalization and therefore on σ_{tot}.

The measurement of ρ is in agreement with the TOTEM measurement within 1.2 standard deviations. The value of $\rho = 0.1362 \pm 0.0034$ used in the previous ATLAS measurement is taken from a global fit to data from lower energies [18] and agrees well with both the TOTEM result and the result in this analysis.

One important caveat is the result for the B-slope using a first order polynomial parametrization for the nuclear modulus. The $\beta^* = 90$ m ATLAS result is

$$B^{\text{ATLAS}} = 19.74 \pm 0.24 \text{ GeV}^{-2} . \tag{13.1}$$

The result for this $\beta^* = 1$ km data set was shown in Table 12.1 but with a different fit range. With the fit range from the $\beta^* = 90$ m ATLAS result, ρ fixed to 0.1362 and all magnet currents fixed in the fit, the B-slope is

$$B = 20.92 \pm 0.30 \text{ GeV}^{-2} . \tag{13.2}$$

This is more than three standard deviations above the ATLAS $\beta^* = 90$ m result. The correlation between the ρ-parameter and the B-slope is larger than 50 %, hence a too high B-slope also results in a too high ρ-parameter.

One possible explanation for the high B-slope is the optics. Including the Q5 magnet currents in the fit yields:

$$B = 20.78 \pm 0.42 \text{ GeV}^{-2} . \tag{13.3}$$

Not only has the value slightly decreased, but the uncertainty has significantly increased and the deviation from the ATLAS result is now only 2.2 standard deviations. This indicates that the optics has an effect on the B-slope, hence it is important to determine the effective optics for this data set in order to perform a reliable measurement.

13.2 Possible improvements

In order to improve the precision on the measurements of σ_{tot} and ρ, a number of things can be done.

For the measurement of ρ, the most important uncertainty contribution comes from the limited statistics. More statistics can easily be obtained with more LHC beam time, however this has to be balanced with other physics interests. The luminosity is low in the elastic setup, and these LHC settings are therefore not usable for the measurements of rare processes. Another possibility is to take data at even lower t-values such that the event yield in the CNI region is enhanced. Going to lower t-values requires a higher β^* and/or a smaller beam.

A smaller beam would give less background in the ALFA detectors. Background is the dominant systematic uncertainty for ρ, hence a lower background level is important for a precise measurement. A smaller emittance reduces the beam size, but also an optimization of the settings for the collimator scraping can reduce the repopulation of the beam halo and thereby the background.

The elastic track reconstruction efficiency would also benefit from a lower background level. Not only would the efficiency be higher since less background events coincide with an elastic event and thereby destroy the track reconstruction. The efficiency would most likely also be determined with a higher precision. The higher efficiency enhances the statistics and thereby the precision on ρ, whereas the better efficiency precision is very important for the uncertainty on σ_{tot}.

A possible improvement for the fit to the observed t-spectrum would be to decompose t into horizontal and vertical components and fit the two dimensional distribution instead. The resolution for the vertical component is about a factor of 10 better than the horizontal, and information is therefore lost when they are combined. The fit would probably also be more sensitive to the alignment parameters, the optics, and the emittance. The primary reason why this is not done in the current analysis is that it would require a determination of the track reconstruction efficiency in this two-dimensional t-space, and the efficiency determination is already limited in statistics.

The ultimate fit procedure would be to simulate the 8-dimensional space of the four sets of (x, y) coordinates in the four detectors. Such a fit could simultaneously handle both the alignment, the effective optics fit, and the determination of physics parameters in a way where no information is lost.

13.3 Outlook - the $\beta^* = 2.5$ km run

From the 19$^{\text{th}}$ to 23$^{\text{rd}}$ September 2016, about 300 μb^{-1} of pp collision data was collected at a center-of-mass energy of 13 TeV and $\beta^* = 2.5$ km. The purpose was to reach the Coulomb dominated region in the differential elastic cross section whereby the absolute luminosity for ATLAS can be determined as discussed in Section 3.3. The very high β^* is required because the beam energy has increased, see Equation (4.15). Based on the online and offline analysis of the $\beta^* = 1$ km data, a number of improvements have been made.

First of all, the collimator settings were fine-tuned. A number of test runs with different settings were tried, and the author took part in the online and fast offline analysis to determine the best configuration. The largest effect was observed when one of the horizontal collimators was retracted further from the beam after the scraping which allowed for a longer time period before the repopulated beam halo would hit the collimator and produce shower events. Furthermore, the time between the scraping periods used for the data taking was optimized. Every scraping takes some time where no elastic data can be recorded, and it also reduces the beam intensity. Scraping should therefore not be done too often nor too rarely, in order to ensure good data quality in terms of efficiency and background. The author invented an online plot for the approximate track reconstruction efficiency which - together with hitmaps and trigger rates - was used to decide when to scrape.

Second, the proton bunches were scraped down to a record low emittance in the SPS before injection into the LHC. This low emittance reduced the size of the beam halo which minimized the background level and the intensity loss during scraping. Furthermore, it improves the t-resolution.

The last point mentioned here is that the optics was optimized to yield larger M_{12}^x's than in the $\beta^* = 1$ km optics where the outer detectors were essentially useless for the reconstruction of the horizontal scattering angle. The t-resolution is therefore expected to be better in the $\beta^* = 2.5$ km data. This was only possible because new LHC power cables for the magnets were installed which allow more freedom in the optics.

Figure 13.1 shows the online hitmaps for events with an elastic trigger. The time period is right before scraping which has the highest background level. The background events are visible very close to the detector edge but the level is observed to be lower than in the $\beta^* = 1$ km data by comparing detector A7L1U with Figure 9.2b. Offline selection criteria will further reduce the background. The difference in horizontal width of the elastic pattern between the inner and outer stations are due to the optics, where the outer stations are more sensitive to the scattering angle.

The offline analysis of the $\beta^* = 2.5$ km data has not yet started. However, due to these improvements a much better precision on ρ is expected than for the $\beta^* = 1$ km data. In addition, a simulation by a collaborator shows that a statistical uncertainty of 2 % on the luminosity can be expected, hence the ultimate goal for ALFA can be obtained with this data set: Determine the Absolute Luminosity for ATLAS!

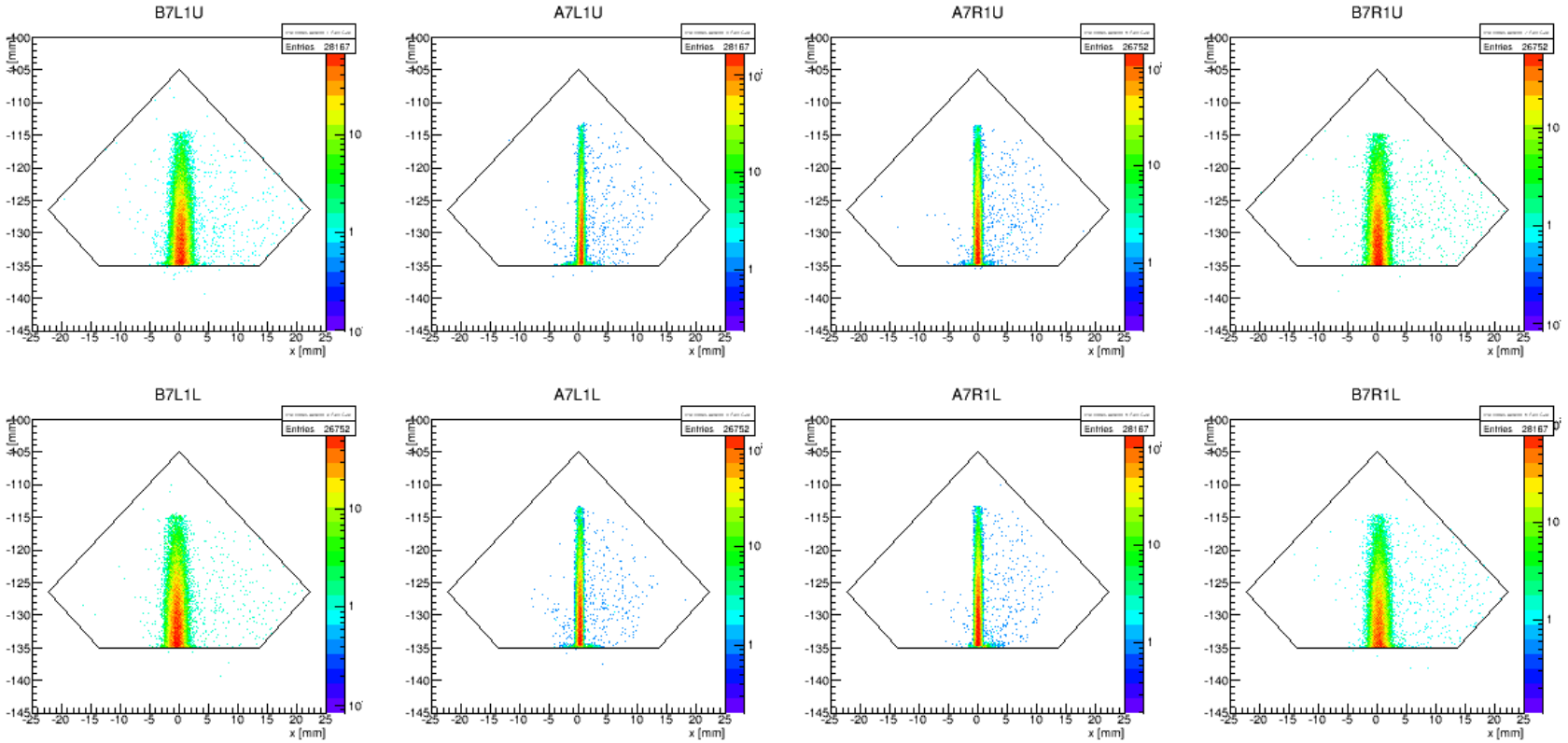

Figure 13.1: Hitmaps for events with an elastic trigger signal accumulated for 20 luminosity blocks just before scraping in one of the $\beta^* = 2.5$ km, $\sqrt{s} = 13$ TeV runs.

14 | Conclusion

The LHC at CERN has opened the possibility to test the Standard Model of particle physics in a new high energy regime. The ALFA detector is built to measure forward elastic proton-proton scattering and thereby probe the non-perturbative phase-space of Quantum Chromodynamics where only phenomenological models are available. Furthermore, the optical theorem relates forward elastic scattering to the total proton-proton cross section, σ_{tot}, which is an important quantity for simulations of high energy processes.

The data analyzed in this thesis was taken at $\sqrt{s} = 8$ TeV with a $\beta^* = 1$ km collision optics and with the detectors positioned only about 1 mm from the beam center. This gave an acceptance above 20 % at a four-momentum transfer down to $3 \cdot 10^{-4}$ GeV^2. This enters the Coulomb-Nuclear-Interference region and therefore allows a determination of the ρ parameter which is the ratio of the real to imaginary forward elastic scattering amplitude.

Unfortunately, the special LHC settings used for this data taking resulted in a high and time-dependent background from the beam halo. Therefore, a new data driven background estimation procedure was developed which takes the time dependence into account. Furthermore, it does not rely on assumptions about symmetric background conditions in the detectors. This background procedure was also implemented in the elastic track reconstruction efficiency determination along with other new developments.

The determination of the detector distance to the beam is crucial for the reconstruction of the four-momentum transfer. An improved distance measurement using the ALFA Overlap Detectors was developed and also used in a recent publication with another data set. Furthermore, online monitoring distance plots were developed for future data taking, and the high voltage for the Overlap Detectors was optimized.

The previous procedure to fit the differential elastic cross section can be biased due to the model dependence in an unfolding procedure and the complex interplay of different experimental effects. Therefore, a new fit procedure was developed where elastic events are generated from a theoretical distribution, all the experimental effects are applied, and the simulation is compared to the observed data distribution. This allows a simultaneous fit of the parameters of interest in the theoretical model and the nuisance parameters for the experimental effects without underlying assumptions about the effects.

Different parametrizations for the modulus in the nuclear scattering amplitude was compared to the data, but there was insufficient statistical power to exclude any of the

investigated models. With a second order polynomial, the preliminary results are:

$$\sigma_{\text{tot}} = 99.1 \pm 0.3 \text{ (stat.)} \pm 1.6 \text{ (syst.) mb} ,$$
$$\rho = 0.166 \pm 0.017 \text{ (stat.)} \pm 0.019 \text{ (syst.)} ,$$

which are in agreement with previous measurements. The final effective optics and elastic track reconstruction efficiency from collaborators are pending. The dominant systematic uncertainties for σ_{tot} are the luminosity and elastic track reconstruction efficiency, whereas the background dominates for the ρ measurement.

The experience from this data analysis and new online monitoring plots were used to optimize the experimental settings for a data taking in September 2016 with $\sqrt{s} = 13$ TeV and $\beta^* = 2.5$ km. Here, the aim is to fulfill the ultimate goal of ALFA: Determine the Absolute Luminosity For ATLAS.

Appendices

A | List of abbreviations

ALFA	Absolute Luminosity For ATLAS
ATLAS	A Toroidal LHC ApparatuS
BBA	Beam Based Alignment
BCM	Beam Condition Monitor
CNI	Coulomb-Nuclear-Interference
CTP	Central Trigger Processor
DPE	Double Pomeron Exchange
EOF	Elastic Overestimation Factor
QCD	Quantum Chromodynamics
QED	Quantum Electrodynamics
QFT	Quantum Field Theory
HLT	High Level Trigger
HV	High Voltage
ID	Inner Detector
IP	Interaction Point
L1	Level 1
L2	Level 2
LHC	Large Hadron Collider
LUCID	Luminosity measurements Using Cherenkov Integrating Detector
MAPMT	MultiAnode PhotoMultiplier Tube
MBTS	Minimum Bias Trigger Scintillator
MC	Monte Carlo
MD	Main Detector
OD	Overlap Detector
PMT	PhotoMultiplier Tube
pp	proton-proton
RUC	Random Uncorrelated Coincidence
SD	Single Diffraction
SM	Standard Model

B | Derivation of the lattice method

The following derivations show that the lattice method is mathematically identical to the local subtraction method.

The transport equation reads:

$$\begin{pmatrix} u \\ \theta_u \end{pmatrix} = \begin{pmatrix} M_{11} & M_{12} \\ M_{21} & M_{22} \end{pmatrix} \begin{pmatrix} u^* \\ \theta_u^* \end{pmatrix} \ , \quad u = (x, y) \ . \tag{B.1}$$

which gives six equations:

$$u^A_{241} = M^A_{11,241} u^{A*} + M^A_{12,241} \theta^{A*}_u \tag{B.2}$$
$$u^A_{237} = M^A_{11,237} u^{A*} + M^A_{12,237} \theta^{A*}_u \tag{B.3}$$
$$u^C_{237} = M^C_{11,237} u^{C*} + M^C_{12,237} \theta^{C*}_u \tag{B.4}$$
$$u^A_{241} = M^C_{11,241} u^{C*} + M^C_{12,241} \theta^{C*}_u \tag{B.5}$$
$$u^A_{241} - u^A_{237} = d_A M^A_{21} u^{A*} + d_A M^A_{22} \theta^{A*}_u \tag{B.6}$$
$$u^C_{241} - u^C_{237} = d_C M^C_{21} u^{C*} + d_C M^C_{22} \theta^{C*}_u \tag{B.7}$$

where d_A, d_C are the distances between the inner and outer stations and where it has been used that

$$\theta_u = \frac{u_{241} - u_{237}}{d} \ . \tag{B.8}$$

The M^A_{21}, M^A_{22}, M^C_{21}, and M^C_{22} are the same at 237 m and 241 m since there are no magnets between the inner and outer ALFA stations that can change the proton angle. Now, the difference between the RHS in Equation (B.3) and (B.2) must equal the RHS in Equation (B.6) which gives:

$$d_A M^A_{22} = M^A_{12,241} - M^A_{12,237} \quad (\text{setting } u^{A*} = 0) \tag{B.9}$$
$$d_A M^A_{21} = M^A_{11,241} - M^A_{11,237} \quad (\text{setting } \theta^{A*}_u = 0) \tag{B.10}$$

and likewise for the C-side.

The lattice method uses the inverse of the transport matrix to find the scattering angle:

$$\begin{pmatrix} u^* \\ \theta_u^* \end{pmatrix} = \begin{pmatrix} M_{11} & M_{12} \\ M_{21} & M_{22} \end{pmatrix}^{-1} \begin{pmatrix} u \\ \theta_u \end{pmatrix} \tag{B.11}$$
$$= \frac{1}{M_{11}M_{22} - M_{12}M_{21}} \begin{pmatrix} M_{22} & -M_{12} \\ -M_{21} & M_{11} \end{pmatrix} \begin{pmatrix} u \\ \theta_u \end{pmatrix} \tag{B.12}$$

which gives

$$\theta^* = \frac{-M_{21,241}u_{241} + M_{11,241}\theta_u}{M_{11,241}M_{22,241} - M_{12,241}M_{21,241}} \tag{B.13}$$

$$= \frac{-M_{21,241}u_{241} + M_{11,241}(u_{241} - u_{237})/d}{M_{11,241}M_{22,241} - M_{12,241}M_{21,241}} \tag{B.14}$$

Substituting for M_{21} and M_{22} using Equations (B.9) and (B.10) gives:

$$\theta^* = \frac{-dM_{21,241}u_{241} + M_{11,241}u_{241} - M_{11,241}u_{237}}{M_{11,241}dM_{22,241} - M_{12,241}dM_{21,241}} \tag{B.15}$$

$$= \frac{-dM_{21,241}u_{241} + M_{11,241}u_{241} - M_{11,241}u_{237}}{M_{11,241}(M_{12,241} - M_{12,237}) - M_{12,241}(M_{11,241} - M_{11,237})} \tag{B.16}$$

$$= \frac{M_{11,241}u_{237} + (dM_{21,241} - M_{11,241})u_{241}}{M_{11,241}M_{12,237} - M_{12,241}M_{11,237}} \tag{B.17}$$

$$= \frac{M_{11,241}u_{237} - M_{11,237}u_{241}}{M_{11,241}M_{12,237} - M_{12,241}M_{11,237}} \tag{B.18}$$

which is the same as the local subtraction method.

C | Additional plots for model investigation

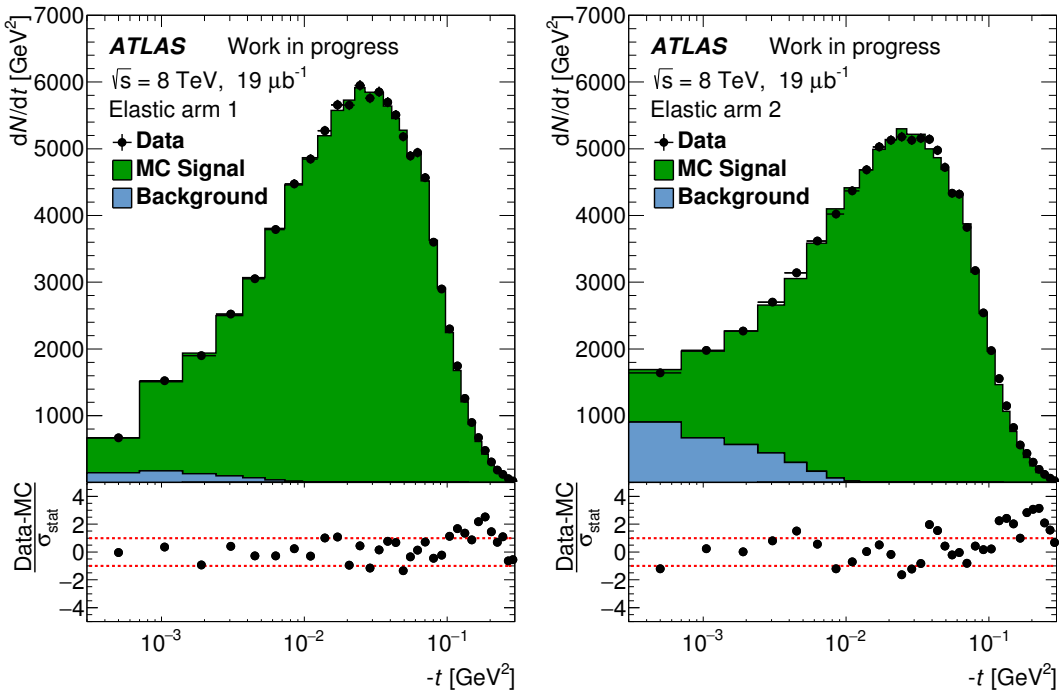

Figure C.1: Comparison of the t-spectra in the data and simulation. A first order polynomial is used for the nuclear modulus.

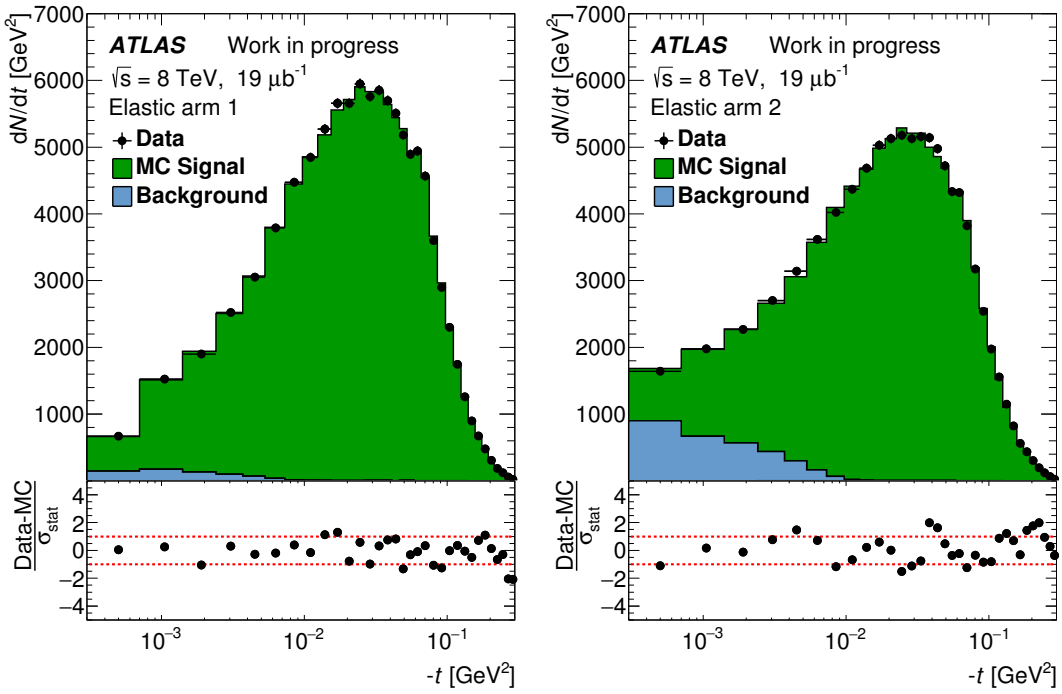

Figure C.2: Comparison of the t-spectra in the data and simulation. A first order polynomial is used for the nuclear modulus.

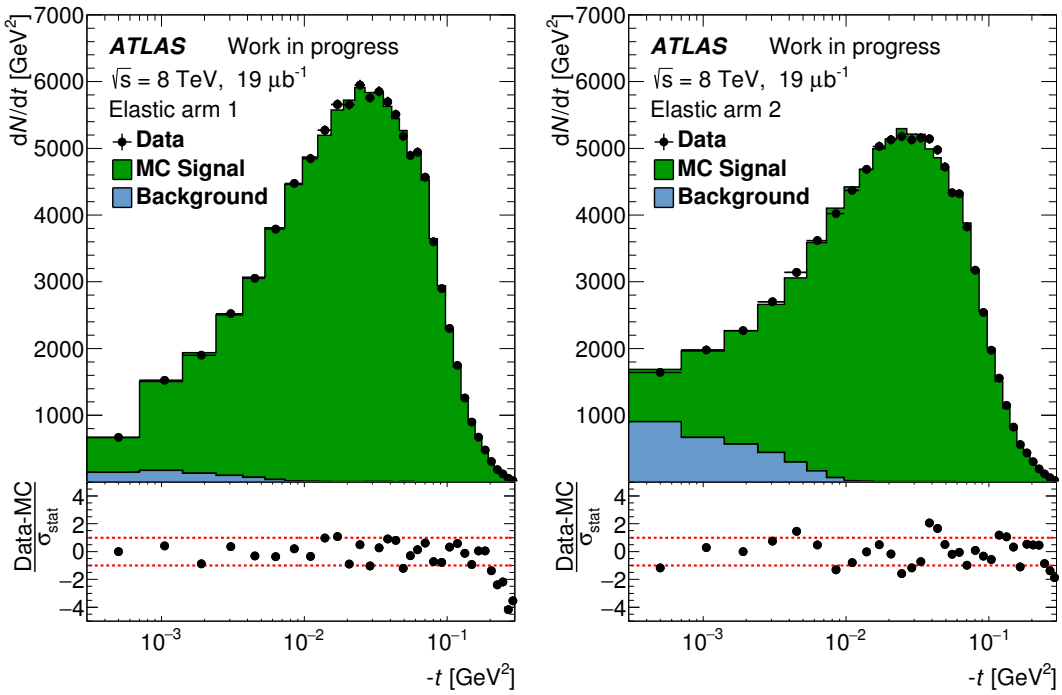

Figure C.3: Comparison of the t-spectra in the data and simulation. A third order polynomial is used for the nuclear modulus.

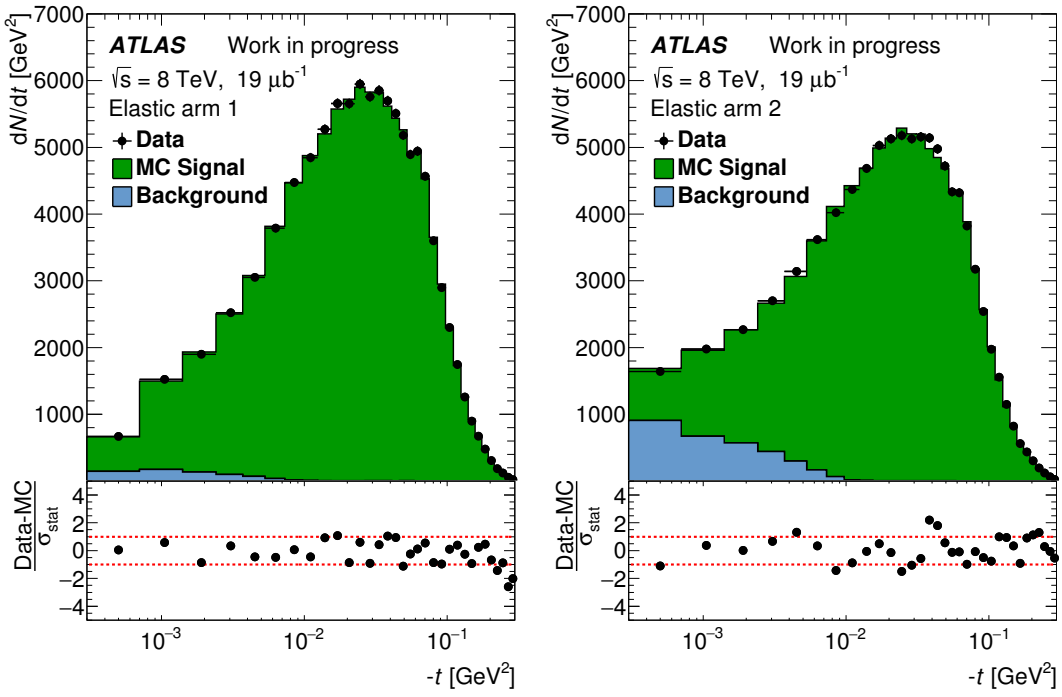

Figure C.4: Comparison of the t-spectra in the data and simulation. The parametrization in Ref. [47] is used for the nuclear modulus.

Bibliography

[1] The Bible, Genesis Chapter 1 Verse 1, 27, and 28. English Standard Version.

[2] The TOTEM Collaboration. Measurement of Elastic pp Scattering at $\sqrt{s} = 8$ TeV in the Coulomb-Nuclear Interference Region - Determination of the ρ Parameter and the Total Cross-Section. Technical Report arXiv:1610.00603. CERN-PH-EP-2015-325. TOTEM-2015-002, CERN, Geneva, Dec 2015.

[3] S. Bethke. Experimental Tests of Asymptotic Freedom, Jun 2006.

[4] `https://en.wikipedia.org/wiki/Standard_Model#/media/File:Standard_Model_of_Elementary_Particles.svg`.

[5] The A1 Collaboration. Electric and magnetic form factors of the proton. *Phys. Rev. C*, 90:015206, Jul 2014.

[6] The TOTEM Collaboration. Proton-proton elastic scattering at the LHC energy of $\sqrt{s} = 7$ TeV. *Europhysics Letters*, 95(4):41001, 2011.

[7] The TOTEM Collaboration. Evidence for non-exponential elastic proton-proton differential cross-section at low $|t|$ and $\sqrt{s} = 8$ TeV by TOTEM. *Nuclear Physics B*, 899:527 – 546, 2015.

[8] G. B. West and D. R. Yennie. Coulomb interference in high-energy scattering. *Phys. Rev.*, 172:1413–1422, Aug 1968.

[9] R. Cahn. Coulombic-hadronic interference in an eikonal model. *Zeitschrift für Physik C Particles and Fields*, 15(3):253–260, 1982.

[10] V. Barone and E. Predazzi. *High-Energy Particle Diffraction*. Springer, Heidelberg, 2002.

[11] The ATLAS Collaboration. Measurement of the total cross section from elastic scattering in pp collisions at $\sqrt{s} = 8$ TeV with the ATLAS detector. *Physics Letters B*, 761:158 – 178, Jul 2016.

[12] M. Froissart. Asymptotic Behavior and Subtractions in the Mandelstam Representation. *Phys. Rev.*, 123:1053–1057, Aug 1961.

[13] A. Martin. Unitarity and High-Energy Behavior of Scattering Amplitudes. *Phys. Rev.*, 129:1432–1436, Feb 1963.

[14] N. N. Khuri and T. Kinoshita. Real Part of the Scattering Amplitude and the Behavior of the Total Cross Section at High Energies. *Phys. Rev.*, 137:B720–B729, Feb 1965.

[15] O. S. Brüning, P. Collier, P. Lebrun, S. Myers, R. Ostojic, J. Poole, and P. Proudlock. *LHC Design Report*. CERN, Geneva, 2004.

[16] `http://te-epc-lpc.web.cern.ch/te-epc-lpc/machines/pagesources/Cern-Accelerator-Complex.jpg`.

[17] T. S. Pettersson and P. Lefèvre. The Large Hadron Collider: conceptual design. Technical Report CERN-AC-95-05-LHC, Oct 1995.

[18] K.A. Olive and Particle Data Group. Review of Particle Physics. *Chinese Physics C*, 38(9):090001, 2014.

[19] The ATLAS Collaboration. Improved luminosity determination in pp collisions at $\sqrt{s} = 7$ TeV using the ATLAS detector at the LHC. *Eur. Phys. J.*, C73(8):2518, 2013.

[20] S. van der Meer. Calibration of the Effective Beam Height in the ISR. 1968.

[21] G. Baud, B. Dehning, J. Emery, J. J. Gras, A. Guerrero, and E. Piselli. Performance Assessment of Wire-Scanners at CERN. (CERN-ACC-2013-0308):4 p, Sep 2013.

[22] The ATLAS Collaboration. The ATLAS Experiment at the CERN Large Hadron Collider. *J. Instrum.*, 3:S08003. 437 p, 2008. Also published by CERN Geneva in 2010.

[23] D. Berge, M. Bona, R. Camacho, R. Kwee, J. Lundberg, and A. Messina. Luminosity Measurement using the ATLAS Minimum Bias Trigger Scintillator System. Technical Report ATL-LUM-INT-2010-004, CERN, Geneva, Mar 2010.

[24] The ATLAS Collaboration. Luminosity determination in pp collisions at $\sqrt{s} = 8$ TeV using the ATLAS detector at the LHC. *The European Physical Journal C*, 76(12):653, 2016.

[25] `https://inspirehep.net/record/878496/files/figures_AtlasDetectorLabelled.png`.

[26] S. Jakobsen, P. Fassnacht, P. Hansen, and J. B. Hansen. *Commissioning of the Absolute Luminosity For ATLAS detector at the LHC*. PhD thesis, Bohr Inst., Dec 2013. Presented 31 Jan 2014.

[27] K. Janas. Analysis of the Track Reconstruction Algorithm in the ALFA detector of the ATLAS experiment. Technical report, 2014.

[28] S. A. Khalek and P. Puzo. *Measurement of the total proton-proton cross section with ATLAS at LHC*. PhD thesis, Orsay, 2013. presented 28 Nov 2013.

[29] P. Jenni, M. Nordberg, M. Nessi, and K. Jon-And. *ATLAS Forward Detectors for Measurement of Elastic Scattering and Luminosity*. Technical Design Report ATLAS. CERN, Geneva, 2008.

[30] C. Joram, H. Stenzel, and A. Braem. Basic Considerations on the Overlap Detectors of the ATLAS ALFA system. Technical Report ATL-LUM-PUB-2007-002. ATL-COM-LUM-2006-009. CERN-ATL-LUM-PUB-2007-002, CERN, Geneva, Jun 2006.

[31] S. S. Mortensen. Kinematic reconstruction of diffractive processes with tagged protons in the ALFA detector at TeV. Master's thesis, University of Copenhagen, Copenhagen, Denmark, 2013.

[32] The ATLAS Collaboration. Measurement of the total cross section from elastic scattering in pp collisions at $\sqrt{s} = 7$ TeV with the ATLAS detector. *Nuclear Physics B*, 889:486 – 548, 2014.

[33] S. S. Mortensen, S. Jakobsen, and A. Guerrero Llorente. Trigger efficiency for the ALFA detector at $\sqrt{s} = 8$ TeV, $\beta^* = 90$ m. Technical Report ATL-COM-FWD-2015-018, CERN, Geneva, Nov 2015.

[34] M. A. Medici. Diffraction with ALFA and ATLAS at $\sqrt{s} = 8$ TeV. Master's thesis, University of Copenhagen, Copenhagen, Denmark, 2013.

[35] B. Giacobbe et al. Measurement of the total cross section from elastic scattering in pp collisions at $\sqrt{s} = 8$ TeV with the ATLAS detector. Technical Report ATL-COM-PHYS-2015-1371, CERN, Geneva, Nov 2015.

[36] B. Allongue et al. Test Beam 2008: First Measurements with an ALFA Roman Pot Prototype. Technical Report ATL-LUM-INT-2010-001, CERN, Geneva, Jan 2010.

[37] P. W. Rasmussen. Elastic pp scattering in ALFA. Bachelor thesis at University of Copenhagen, 2016. Available upon request.

[38] R. Ciesielski, K. Goulianos. MBR Monte Carlo Simulation in PYTHIA8. (arXiv:1205.1446).

[39] J. Wenninger. Energy Calibration of the LHC Beams at 4 TeV. Technical Report CERN-ATS-2013-040, CERN, Geneva, May 2013.

[40] CERN Accelerator Beam Physics Group. Mad - methodical accelerator design. `http://mad.web.cern.ch/mad/`.

[41] LHC eLogBook. `https://op-webtools.web.cern.ch/elogbook/?lgbk%5B%5D=60`.

[42] ATLAS beam spot page. `https://atlas-beamspot.cern.ch/jobfiles/data12_8TeV.00213268.express_express/DB_BEAMSPOT.x232_c802/data12_8TeV.00213268.express_express-DB_BEAMSPOT.x232_c802.PlotBeamSpot.pdf`.

[43] B. Allongue et al. Results from the ALFA test beam campaign in 2009. Technical Report ATL-COM-LUM-2010-031, CERN, Geneva, Oct 2010.

[44] K. Kreutzfeldt, M. Düren, and H. Stenzel. *Measurement of elastic proton-proton scattering at* $\sqrt{s} = 7$ *TeV with the ALFA sub-detector of ATLAS at the LHC*. PhD thesis, Giessen U., Dec 2014. Presented 27 Feb 2015.

[45] V. Blobel. Some Comments on χ^2 Minimization Applications. 2003.

[46] MINUIT user's guide. `http://seal.web.cern.ch/seal/documents/minuit/mnusersguide.pdf`.

[47] O. Selyugin. Problems of determination of σ_{tot} at the LHC. (arXiv:1310.0928).

[48] T. Adye. Unfolding algorithms and tests using RooUnfold. (arXiv:1105.1160):6 p, May 2011. Comments: 6 pages, 5 figures, presented at PHYSTAT 2011, CERN, Geneva, Switzerland, January 2011, to be published in a CERN Yellow Report.